

Copyright

by

Indre Altman

2020

The Thesis committee for Indre Altman

Certifies that this is the approved version of the following thesis:

**Submarine Channel Curvature and Migration Distance: A Study of Joshua Channel with
Implications for Sinuous Submarine Channel Geomorphology and Deepwater Reservoir
Prospectivity**

SUPERVISING COMMITTEE:

Zoltan Sylvester, Co-Supervisor

David Mohrig, Co-Supervisor

Richard Chuchla

**Submarine Channel Curvature and Migration Distance: A Study of Joshua Channel with
Implications for Sinuous Submarine Channel Geomorphology and Deepwater Reservoir
Connectivity**

by

Indre Altman

Thesis

Presented to the Faculty of the Graduate School
of the University of Texas at Austin

in Partial Fulfillment

of the Requirements

for the Degree(s) of

Master of Science in Energy and Earth Resources

The University of Texas at Austin

August 2020

Dedication

This thesis is dedicated to people who encourage resilience. Dr. Sylvester, thank you for teaching me that nearly any problem--technical or otherwise--may be solved with enough patience and searching. Mr. Chuchla, thank you for helping me always focus on growth no matter temporary hurdles that come in the way. To my family in Houston and especially to Adam, thank you for your upbeat encouragement.

Acknowledgments

The pursuit of this degree would not be possible without CLEAResult and their fellowship dedicated to the memory of their founder Glenn Garland. The remarkable life that Glenn Garland led is inspiring in every sense of the word, and he will be remembered as a visionary. Thank you to the staff of CLEAResult as well, who kindly welcomed me into their community on several occasions with insightful conferences and a warm office shadowing. The good-natured people in the Austin office and their meaningful, challenging, and interdisciplinary work showcase the values underpinning the EER graduate program.

My thesis committee members have been extraordinarily helpful. Thank you for all meeting with me--even over Zoom--to ensure that the paper was on track. Dr. Sylvester, I will always appreciate the many hours that you put in helping me adjust to QGIS and Python, and your faith in me. Dr. Mohrig, your enthusiasm for graduate student research is unparalleled. Mr. Chuchla, I came away from every discussion learning something valuable and new.

Thank you to the members of the Quantitative Clastics Laboratory for encouraging endless curiosity. In particular, thank you to Jake Covault for offering to meet with me many months ago and investing in our learning with a remarkable trip to San Diego.

Lastly, thank you to the EER community, especially Jessica, who ensures that every student thrives the most that they can.

Submarine Channel Curvature and Migration Distance: A Study of Joshua Channel with Implications for Sinuous Submarine Channel Geomorphology and Deepwater Reservoir Prospectivity

by

Indre Altman, M.S.E.E.R.

The University of Texas at Austin, 2020

SUPERVISORS: Zoltan Sylvester and David Mohrig

The nature of plan-view migration in submarine channels is a subject of debate among researchers, and of significance to oil and gas investment in deepwater prospects. Early work has suggested that common features in fluvial channels such as downstream migration are rare or absent in deepwater reservoirs, and that relationships between geometric attributes of submarine channels do not compare to those in fluvial channels. This study explores whether curvature and migration in sinuous submarine channels are correlated, in a similar manner to rivers in the Amazon, where a recent study has found that variance in curvature explains 57% of variance in migration rate. Using bathymetric and seismic data from the Joshua Channel in the Eastern Gulf of Mexico, this study find that variance in curvature explains approximately 52% of variance in migration distance. In addition, the lag between curvature and migration is similar to that found in rivers when scaled to thalweg width. Lastly, a qualitative financial discussion of reservoir connectivity highlights the importance of understanding submarine channel kinematics.

Table of Contents

Chapter One: Introduction.....	1
Chapter Two: Geological Context.....	7
Chapter Three: Methodology.....	16
Chapter Four: Results.....	24
Analysis of Seismic Data.....	24
Analysis of Bathymetric Data.....	33
Chapter Five: Discussion.....	40
Curvature and Migration.....	40
Curvature and Half-width.....	44
Chapter Six: Qualitative Analysis of Financial Implications.....	50
Chapter Seven: Conclusion.....	70
Appendix.....	72
Bibliography.....	85

Chapter One: Introduction

Hydrocarbon reservoirs of deepwater depositional systems have become an increasing focus of investment since the 1990s (Pettingill and Weimer, 2002). Because ancient submarine channels are often prolific reservoirs (e.g., Beydoun et al., 2002; Abreu et al., 2003) and submarine channels serve as sediment transport conduits for laterally more extensive lobes, understanding the stratigraphic architecture and the distribution of heterogeneities in channelized deepwater systems is of great interest in the energy industry.

Understanding the evolution and the resulting architecture of deepwater channels is as fascinating to geomorphologists as it is vital to determining the profitability of deepwater projects. The history of channel migration and the resulting depositional architecture are among the main factors controlling the extent and connectivity of channelized reservoirs. Although typical submarine channel reservoirs tend to be well connected in three dimensions, high-sinuosity systems have highly complex geometries and a wide range of variation in porosity and permeability. Heterogeneities such as mud drapes, debris flow deposits, and mudclast conglomerates can act as flow barriers or buffers, and high-permeability streaks along channel axes often result in early water breakthrough at producing wells. Reservoir connectivity and the nature of fluid flow in the reservoir ultimately will impact hydrocarbon recovery, development plans, and the economic feasibility of a project.

In sedimentary geology and geomorphology, there is an ongoing debate about how the complex geometries of submarine channels are generated. One of the key questions is whether the kinematics of submarine channels are similar to migration patterns described from rivers. The fact that submarine channels are difficult to observe in real time (Talling et al., 2015) exacerbates these debates, for the physics of channelized turbidity currents differ in several respects from the physics of open-channel flow. Early observations suggested that features common in fluvial channels, such as downstream migration, point bars, and cutoff meanders, are rare or absent in deepwater channels. New seafloor- and seismic data increasingly challenges this view, suggesting that highly sinuous submarine channels for which the large-scale plan-view migration patterns are qualitatively similar to those of meandering rivers. This study aims to compare the relationship between channel curvature and bank migration in a submarine channel in the Eastern Gulf Of Mexico (Joshua Channel) to the same relationship described from fluvial channels (in

this case, rivers in the Amazon Basin), in order to investigate whether the simple plan-view kinematics of submarine channels is similar to fluvial channel migration.

This project first seeks to test whether, as recently described from fluvial channels (Sylvester et al., 2019), curvature explains a significant fraction of the migration rates in sinuous submarine channels. Relying on a simple kinematic model that has explained an average 57% of variance in the migration of several Amazon Basin rivers (Sylvester et al., 2019), this project will test the relationship between curvature and bank migration in sinuous submarine channels and explore how submarine channels compare to their fluvial counterparts.

The model used by Sylvester et al. (2019) for the Amazon Basin relies on two key assumptions that probably apply to submarine channels as well: 1) that the location of maximum migration lies downstream of the point of maximum curvature (Seminara, 2006), and that 2) defining bank erosion as a function of local and upstream curvatures may allow for the derivation of an expected migration rate (Howard and Knutson, 1984). These assumptions relate to the concept of “nominal migration rate”, which describes migration rate as the rate that would be expected if bank erosion depended only on local curvature (Fig. 1; Howard and Knutson, 1984).

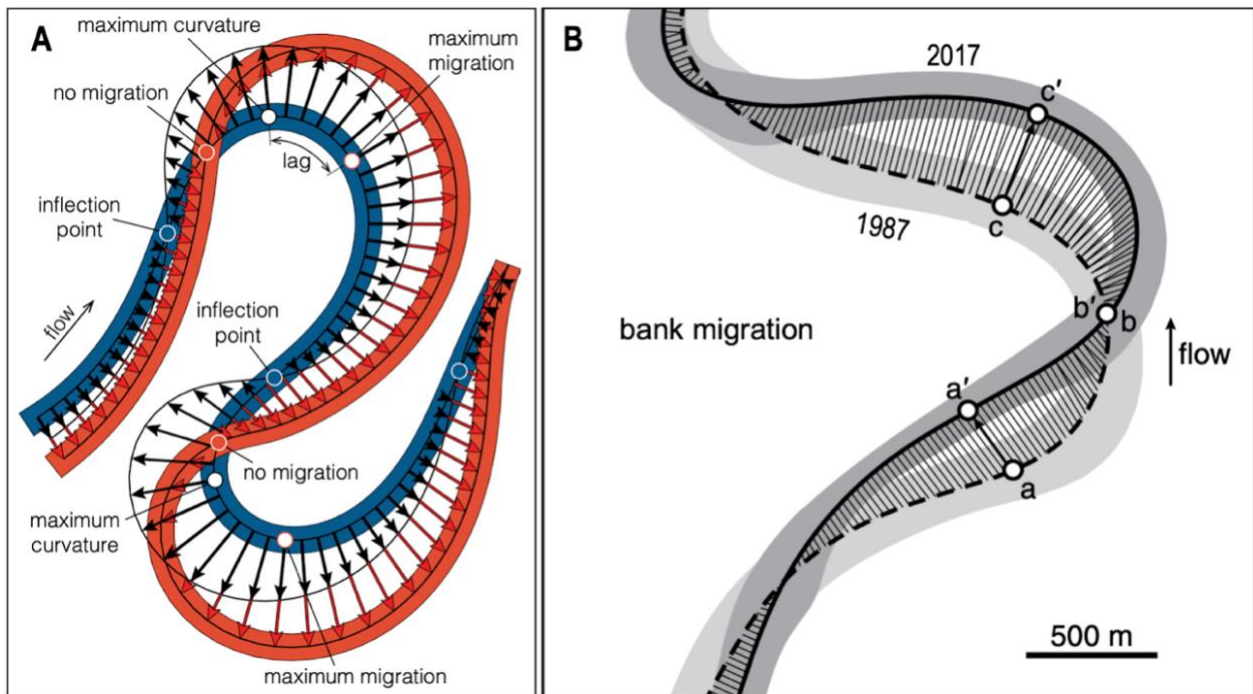


Figure 1. A: Downstream delay of predicted migration rate relative to bend curvature in a simple model of meandering (Sylvester et al., 2019). Nominal (black arrows) and predicted (red arrows) migration rates are plotted along two meander bends, with a phase lag corresponding to the along-channel distance

between locations of maximum curvature and maximum migration. B: Example of estimated bank migration vectors displayed between two centerlines (Sylvester et al., 2019). Every point on the centerline of the old channel (dashed line) is correlated to a point on the centerline from the new channel (solid line), minimizing distance between points with a dynamic time warping algorithm. This approach can be used between every centerline pair in a dataset of channel centerlines.

While Howard and Knutson (1984) use an empirical relationship between local curvature and nominal migration rate, Sylvester et al. simplify their approach by defining the nominal migration rate (R_0) as the product of the dimensionless curvature (W/R) and the migration rate constant k :

$$R_0 = k_l W/R. \quad (1)$$

Migration rates are predicted as the weighted sum of upstream curvatures, where Ω and Γ are weighting parameters with values of -1 and 2.5 , s is the current location along the centerline, ξ is the along-channel distance upstream from that location, and $G(\xi)$ is an exponential weighting function:

$$R_1(s) = \Omega R_0(s) + \left[\Gamma \int_0^\infty R_o(s - \xi) G(\xi) d(\xi) \right] \left[\int_0^\infty G(\xi) d(\xi) \right]^{-1}, \quad (2)$$

and

$$G(\xi) = e^{-\alpha\xi}, \quad (3)$$

where α is a function of the friction factor (C_f), water depth (D), and a constant (k) that equals 1: $\alpha = 2kC_f/D$. (4)

Sylvester et al. (2019) assume a constant value for D for each river segment, and optimize the value of the friction factor C_f to minimize the phase shift between the actual and predicted migration curves. The migration rate constant k is estimated by minimizing the difference between the absolute values of the actual and predicted migration rates.

This model can be used to predict bank migration, defined as the rate of bank erosion and accretion measured along a direction perpendicular to the banks or the centerline (Figure 1b). Even though submarine channels aggrade more than fluvial channels (Peakall et al., 2000; Jobe et al., 2016), this two-dimensional model may still apply to submarine channels given that many exhibit plan-view migration patterns qualitatively similar to those of rivers (e.g., Sylvester et al., 2011; Kolla et al., 2012).

Second, this project seeks to explore whether this model may also apply to the relationship between curvature and a potentially useful parameter: the half-width. Banks migrate through erosion of their cutbanks and deposition on their inner banks. As a result, channel cross

sections are asymmetric where significant migration occurs because cutbanks have steeper gradients than inner banks. Because these profiles change according to migration activity, the variable distance between the channel thalweg and the highest point of the inner bank might be a proxy for bank migration. This distance is called the channel half-width. If proved an appropriate proxy, this approach would allow geomorphologists to determine the positions of maximum migration along channels lacking time series data.

To capture the half-width parameter, boundaries of channel banks were drawn reflecting interpreted bankfull flow on Joshua Channel (Fig. 2). The distance between this boundary and the centerline likely displays higher variability than that of the total width because it captures the details of the thalweg location in relation to the banks. The half-width estimates inner bank accretion, with half-width peaks corresponding with point bars and half-width troughs corresponding to cutbanks. If one considers the half-width to vary with bank migration, then variations in half-width may likewise follow curvature. The location of maximum half-width should, in theory, coincide with the location of maximum migration.

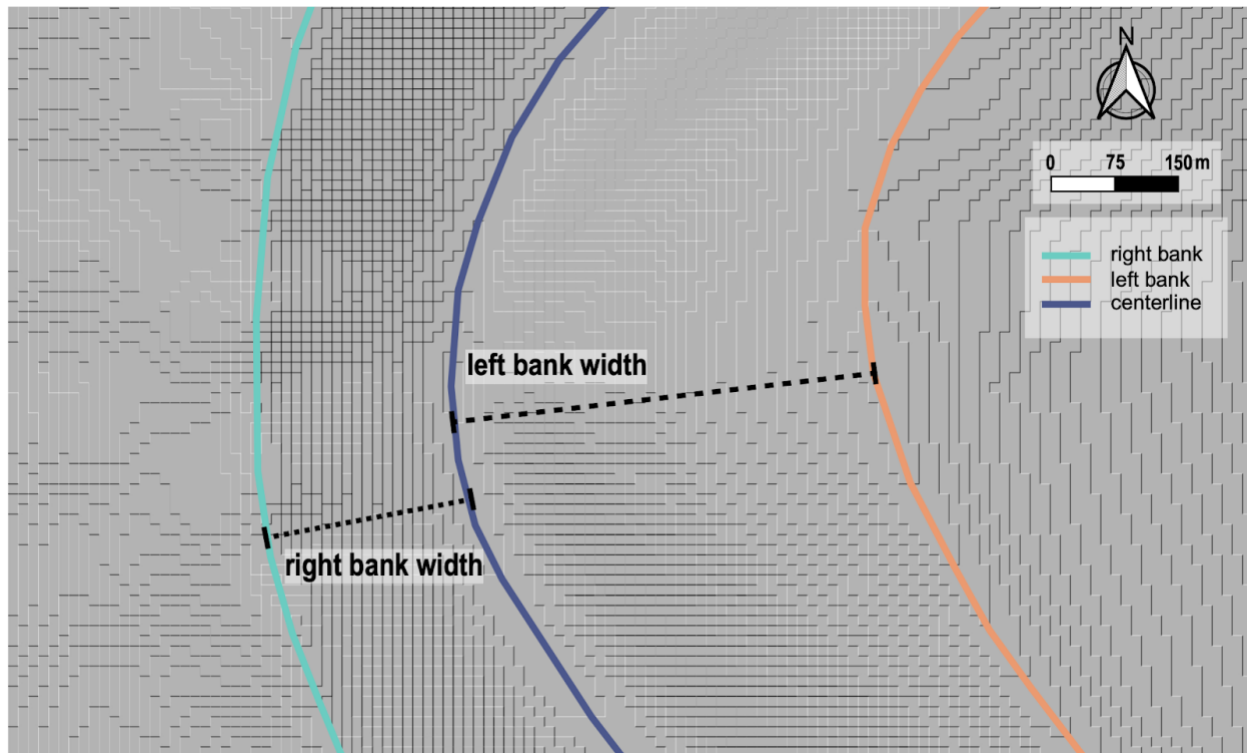


Figure 2. The channel half-width is the distance between the channel centerline (interpreted thalweg) and the two banks: either the right bank width or left bank width may be used as a “half width” parameter. In this example, the left bank width reaches a maximum just south of the apex of the channel bend and then declines, and the right bank width appears to reach a minimum

where the left bank width is maximized. The half width should be selected so that it is in phase with curvature plots, which reflect positive or negative values depending on the bend.

This study focuses on the relationships between curvature, half-width, and bank migration for a sinuous deep-water channel, using bathymetric and 3D seismic data from the 'Joshua Channel' in the Eastern Gulf of Mexico. First this study investigates whether a quasi-linear relationship between curvature and bank migration exists in deep-water sinuous channels using 3D seismic data. Next the relationship between curvature and half-width is examined using bathymetric data from the same system. This analysis provides another way to think about the spatial expression of migration distance and curvature.

The question of whether migration relates to and lags behind curvature in deepwater channels is a critical one to ask in the context of deepwater exploration and appraisal. If the lag that Sylvester et al. (2019) find in fluvial channels is found for Joshua Channel, then this would suggest that downstream migration is a significant feature of sinuous deepwater channels. If the expression of downstream migration in submarine channels plays a meaningful role, then deepwater channel reservoir models may need to adjust assumptions about how channels stack laterally and vertically within reservoirs. Channel stacking patterns are a key component of reservoir architecture, which is a critical consideration not only during exploration but also during development, when wells are strategically placed to optimize flow through the reservoir.

This study will conclude with qualitatively analyzing the financial implications of channel architecture on hydrocarbon production. Geologic interpretations of reservoir connectivity affect prospect valuation, which utilizes volumetric estimates of reserves and reservoir connectivity for production profiles and cash flow estimates. However, financial analyses often make simplistic assumptions about volumetric estimates that fail to capture the full spread of development scenarios. This analysis will explore the extent to which depositional architecture may impact financial projections for a prospect. Improving financial analyses with technical insights is particularly important to investment in expensive deep-water development, for which confidence in expected production profiles is vital.

The outcomes of this study are important not only to sedimentology, but also to reducing early uncertainties in prospect analysis. Data acquisition, particularly of well and core data, is expensive because of the high cost of operating and drilling in deepwater. Many types of key data (e.g. grain size, porosity, permeability, presence and nature of mud drapes) are best accessed

through drilling data, which is obtained after acquiring and interpreting 3D seismic surveys. However, if geoscientists optimize the information they may glean from 3D seismic data, they may reduce uncertainty early on in exploration and provide better recommendations for optimum exploration and appraisal well placement. Channel curvature is one particularly useful parameter. It is simple to extract from 3D seismic surveys, and is recognized to strongly impact channel migration in fluvial systems (Howard and Knutson, 1984; Ikeda, 1981). Lateral migration determines channel placement, and therefore channel stacking patterns in aggradational deepwater systems. Channel stacking patterns determine vertical and horizontal permeability in channelized reservoirs, and thus exert a control on flow rates and initial production rates. If this study finds a relationship between curvature and migration in submarine channels, then curvature from 3D seismic surveys may be used to inform realistic modeling of channel stacking patterns and resulting reservoir connectivities.

Chapter Two: Geological Context

The Joshua Channel, a relatively undisturbed deepwater channel-levee system in the northeastern Gulf of Mexico, offers an opportunity to study the architecture and evolution of deepwater channels. Joshua Channel lies in water depths of over 2500 m (ultra-deepwater), and according to a new map published by the Bureau of Ocean and Energy Management in 2018, Joshua Channel is visible on the seafloor for 280 kilometers. Another 240 kilometers of the channel are buried but can be mapped in seismic data (Posamentier, 2003; Kramer et al., 2016). The high quality bathymetric and seismic data and well-preserved nature of long segments of the Joshua Channel length provide great potential for studying submarine channel migration. The regional and local geological history, depositional setting, and planform geometry of this channel provide important context for this case study.

The Joshua Channel is located in the northeastern Gulf of Mexico, which was formed through the crustal extension and seafloor spreading associated with the Mesozoic break-up of Pangea (Galloway, 2008). Following the formation of basement grabens and half grabens in the Late Triassic through Early Jurassic extension, the main phase of rifting occurred from the Late Jurassic to Early Cretaceous (Galloway, 2008). Normal continental crust rims the edges of the Gulf of Mexico. Transitional continental crust resulting from Middle to Late Jurassic rifting is thick in the northern portion of the basin and thin in the southern and western portions (Fig. 3). The central Gulf floor contains Late Jurassic oceanic crust (Fig. 3). During this Jurassic rifting, sea water entering the Gulf of Mexico deposited an extensive salt layer. The basin then evolved into a restricted basin in which source rock was deposited (Galloway, 2008). The Gulf of Mexico transitioned into an open basin during the Cretaceous, leading to additional deposition of organic matter and carbonate layers, and to additional subsidence from sediment loading (Galloway, 2008). In the Cenozoic, the basin received large amounts of clastics shed by North American highlands which were generated during the Sevier and Laramide orogenies (Galloway, 2008). This sequence of events generated thick clastic sedimentary layers and deformed the Callovian salt. Both factors created the conditions to produce significant hydrocarbon volumes sealed by shale and salt.

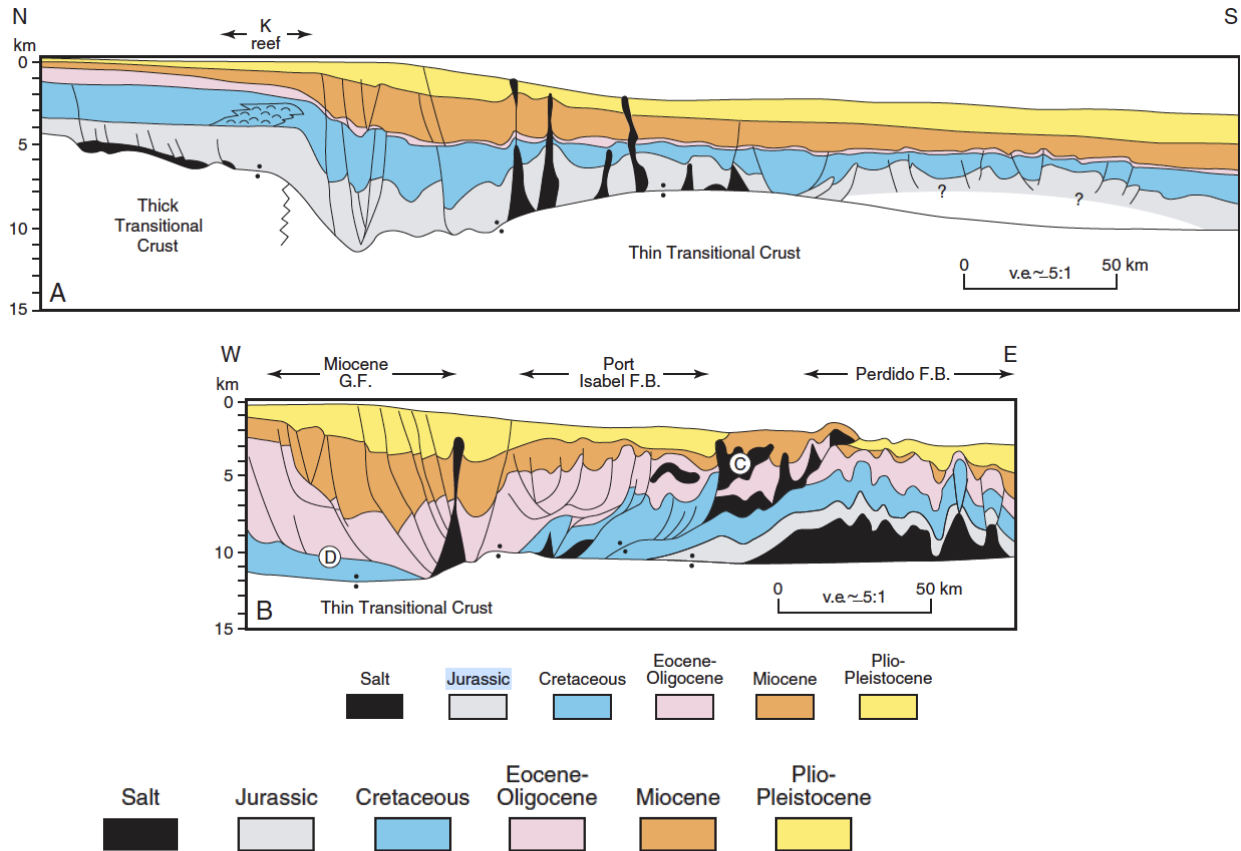


Figure 3. Dip cross-section of the northeastern (A) and northwestern (B) Gulf of Mexico continental margin, from Galloway (2008). For cross-section location see Figure 5 in Galloway (2008).

The establishment of Joshua Channel is associated with Pleistocene Gulf of Mexico depositional systems. By the late Pliocene, the North American ice sheet had developed and reshaped drainage systems flowing into the Gulf. This ice sheet diverted north-flowing streams to the south vis-a-vis damming, and coalesced the streams of the paleo-Mississippi basin. The Mississippi Valley was cut and back filled with glacial outwash. The single large Mississippi River observed today was established by the late Pleistocene (Galloway 2008). Frequent and dramatic sea-level changes that followed forced shorelines and sediment transport conduits to adjust. Transgressions propelled the shores landward to create large shelves (Galloway 2008). Subsequent regressions pulled the shores seaward, which generated deep valleys across the shelves (Galloway 2008). . These events occurred along with high sediment supply from protruding delta lobes, a series of enormous mass wasting events associated with glacial outwash, and submarine canyon erosion (Galloway 2008). Canyon excavation was most

prominent along the eastern edge of the delta system (Galloway 2008). Along the northeastern end of the continental margin, the Plio-Pleistocene fill is relatively thin (Fig. 3).

The Joshua Channel is situated on a basin plain southeast of the Mississippi Canyon and west of the Florida escarpment (Fig. 4), in the DeSoto Canyon area of the northeastern Gulf of Mexico (Posamentier 2003). In 1968, R.N. Harbison described DeSoto canyon as “a curious S-shaped submarine canyon” with a gentle gradient and a closed bathymetric low in its southeastern portion (Harbison 1968). The canyon basin reaches 17 kilometers from north to south with a gradient of 0.15 degrees, and 13 kilometers towards the southwest with approximately 8-degree slopes to the east and west (Harbison 1968). The canyon itself is 0.5-1 km wide and 10-20 m deep (Clark and Pickering 1996). The deposits of the Joshua Channel system within this basin were the results of sediment transport through the Mississippi River and canyon system around the mid to late Pleistocene, with updip linkage to the Pearl River in Louisiana (Kramer et al., 2016). While the canyon was thought to be a recent topographic feature related to the convergence of the Florida Escarpment and the Mississippi Fan, Denne et al. (2013) speculate that the canyon is the remnant of an older, larger, erosional canyon whose incision coincided with (and was potentially induced by) the seismicity of the Chicxulub impact. While the western side of the DeSoto basin experienced some strike-slip deformation (associated with differential subsidence and basinward sliding over salt layers), the eastern DeSoto Basin has no strike-slip features present and relatively small amounts of salt (Bouroullec et al., 2017).

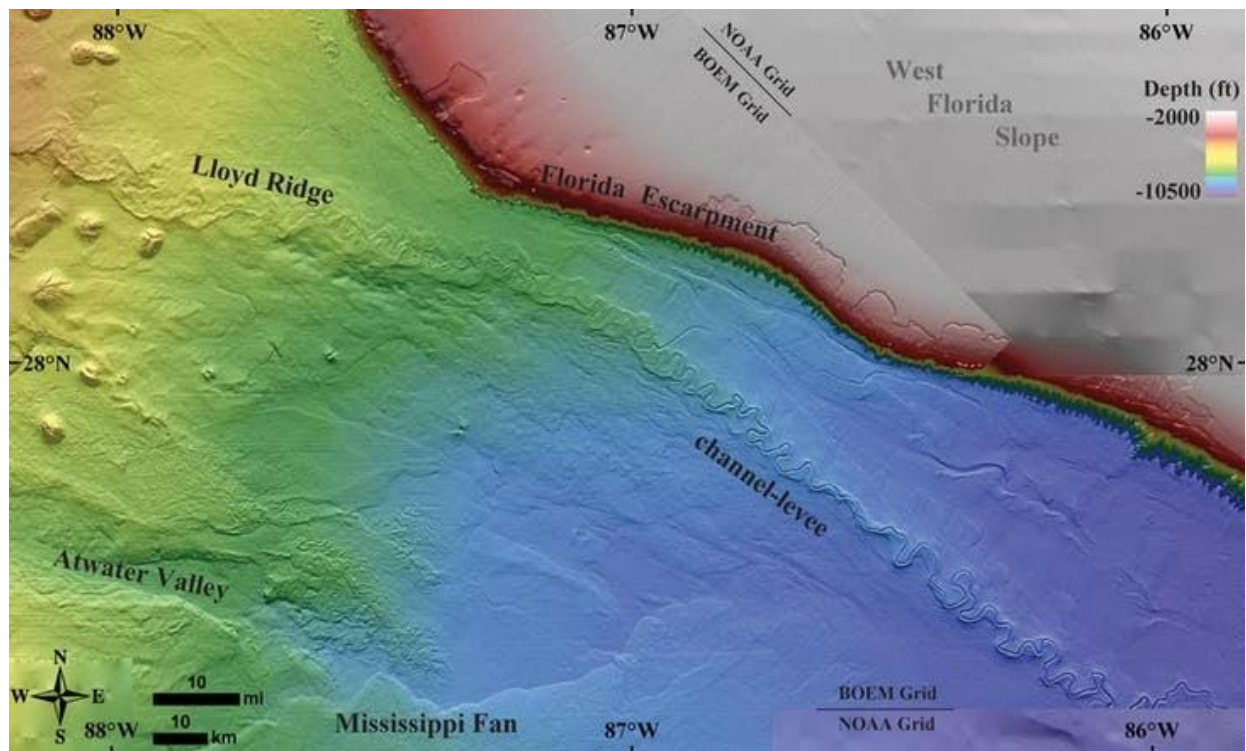


Figure 4. Bathymetric map of the Eastern Gulf of Mexico available from the Bureau of Ocean Energy Management showing the Joshua Channel (labeled “Lloyd Ridge” and “channel-levee”) and surrounding areas (Kramer and Shedd, 2017).

Originating from the ancient Pearl River canyon, Joshua Channel is a 400+ mile abandoned channel-levee system lying about two miles below sea level (Kramer et al., 2016). It is bound between salt domes to the north, the Mississippi Fan to the southwest, and the Florida Escarpment to the east. This regional confinement led to a largely linear geometry along the basin floor (Kramer et al., 2016). The channel complex was likely initiated with canyon incision and downdip deposition during the Wisconsin glacial 74 kya (Martinson et al., 1987). The principal depositional elements of the system are shown in Figure 5. In this time period the Louisiana outer-continental shelf edge collapsed, causing the 500-mile-long mass transport deposit that would provide the foundation for the following coarse bedload braided channels making up the early Joshua Channel (Kramer et al., 2016). The channel then transitioned to an avulsing single channel-levee as sediment supply declined, with its levee cut-banks periodically failing and leaving overbank splays (Kramer et al., 2016). The channel also gradually became more sinuous as it evolved, as evident in seismic data. It is likely that the Joshua Channel was pushed towards the Florida Escarpment by the growth of the Mississippi Fan (Bouma 2000). Pleistocene and Holocene sediments subsequently buried the system, and it was abandoned 29 kya (Kramer et al., 2016). The channel

system temporarily acted as a barrier to the Mississippi Fan during an unknown period, and when it failed young sediments spilled out over the system onto the eastern levee of the channel, as well as into an adjacent basin towards the Florida Escarpment (Kramer et al., 2016). Now in ultra-deepwater, the system remains well-preserved underneath a hemipelagic drape (Posamentier, 2003; Kramer et al., 2016).

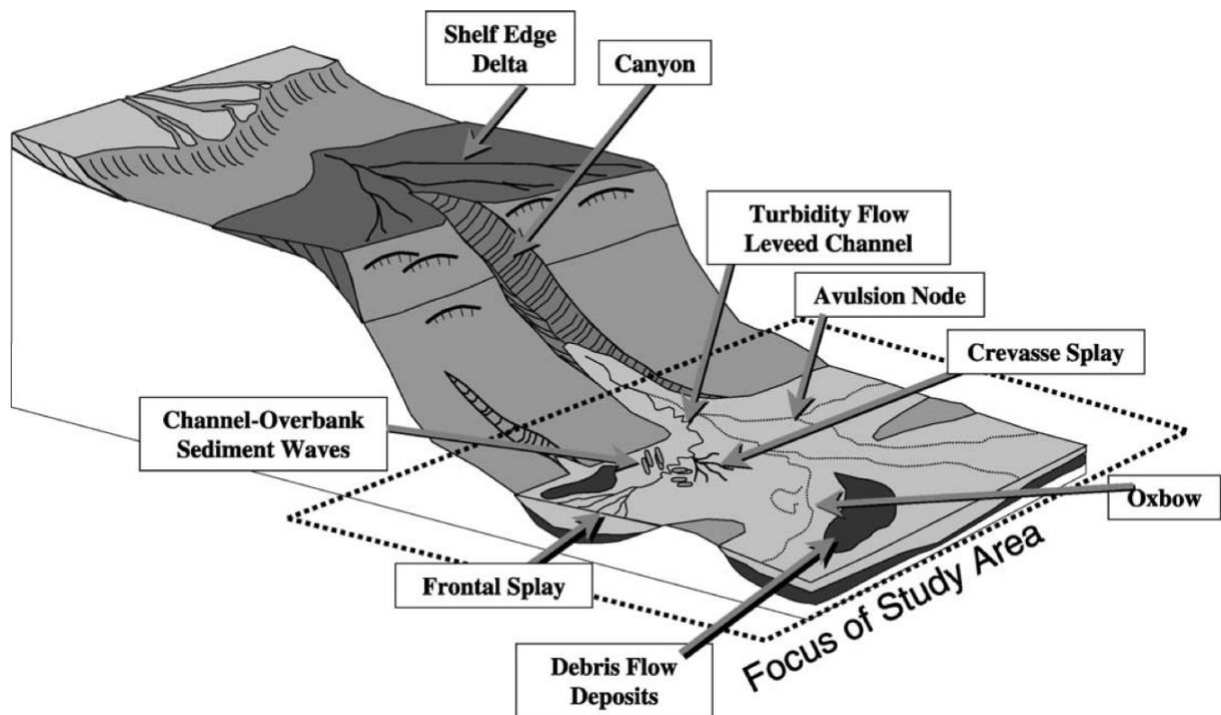


Figure 5. Schematic illustration of principal depositional elements from shelf edge to basin plain. Posamentier et al., 2003).

The planform geometry of Joshua Channel is characterized by moderately to highly sinuous bends flanked by levees. Sediment waves decorate the levees, likely the result of flow stripping and overspill, and some slump scars are visible (Fig. 8a; Posamentier, 2003). The bankfull channel width has been identified as 787 m (P50), as measured between levee crests, excluding channel axes. The channel depth is about 22 m (Shumaker et al., 2018). The ratio of channel width to depth (the aspect ratio) is approximately 36 (Fig. 6a; Shumaker et al., 2018). The ratio between the along-channel distance and straight-line distance between the first and last measured points (the average whole-channel sinuosity) is approximately 2.1 to 2.21 (Fig. 6b, Shumaker et al., 2018). When inspecting bathymetric data provided by the Bureau of Ocean Energy Management, the channel fill lies about 50 m above the basin floor, with differential

compaction likely accounting for the limited expression of levees relative to the channel relief. The channel height appears to be emphasized by differential compaction, as muddy levees will have compacted more than sandy channel deposits (Fig. 7).

In seismic data, continuous to discontinuous high seismic amplitudes suggest a sandy channel fill, and patterns of dynamic channel behavior such as swing and sweep are noticeable (Fig. 7; Fig. 9; Posamentier, 2003). Evidence of downstream migration is discernible from U-shaped channel stacks seen in seismic cross sections, which also indicate a transition from dominant lateral migration to dominant aggradation throughout the evolution of the channel (Fig. 9). Posamentier (2003) observes downstream meander loop migration in 16 out of 22 crossings, as well as four cutoffs and seven avulsions. The avulsion events occurred in the late stages of the channel evolution. These events are associated with levee crevasses and avulsion channels feeding frontal splays (Posamentier 2003). While cutoffs and avulsions are observed by Posamentier (2003; Fig. 8b) and Shumaker et al. (2018) along upstream and downstream portions of the channel, these events are not observed in the channel segments investigated here. The observed swing and sweep behaviors, as well as the presence of cutoffs, suggest that the dynamic plan view kinematics of Joshua Channel are similar to those of rivers.

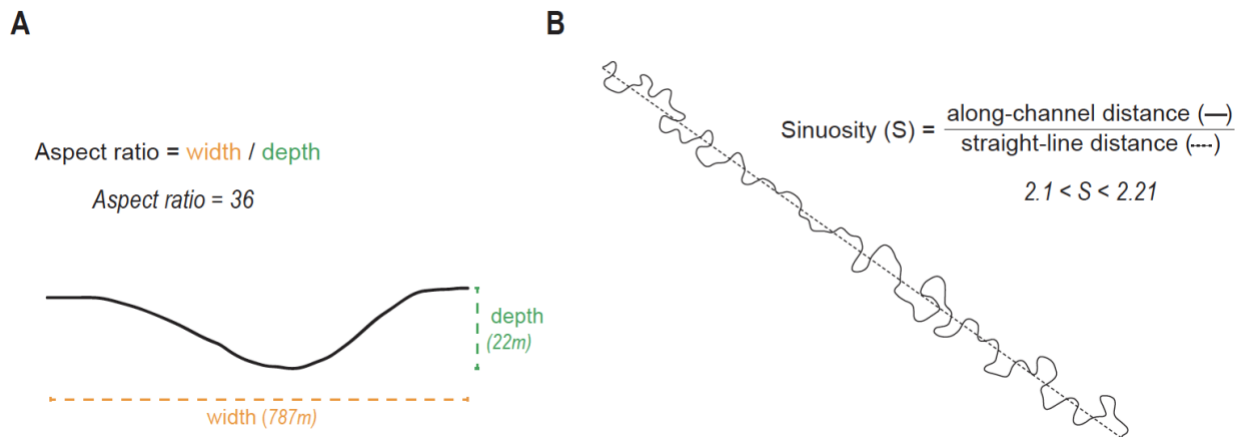


Figure 6. A: Illustration of aspect ratio in Joshua Channel, with channel width (width) and depth (green), and aspect ratio measurements calculated by Shumaker et al. (2018). Channel profile is vertically exaggerated. B: Joshua Channel in plan view with sinuosity annotated as the ratio of the length of the solid black segment to the length of the dashed segment, and a range of sinuosity values calculated by Shumaker et al. (2018) for Joshua Channel.

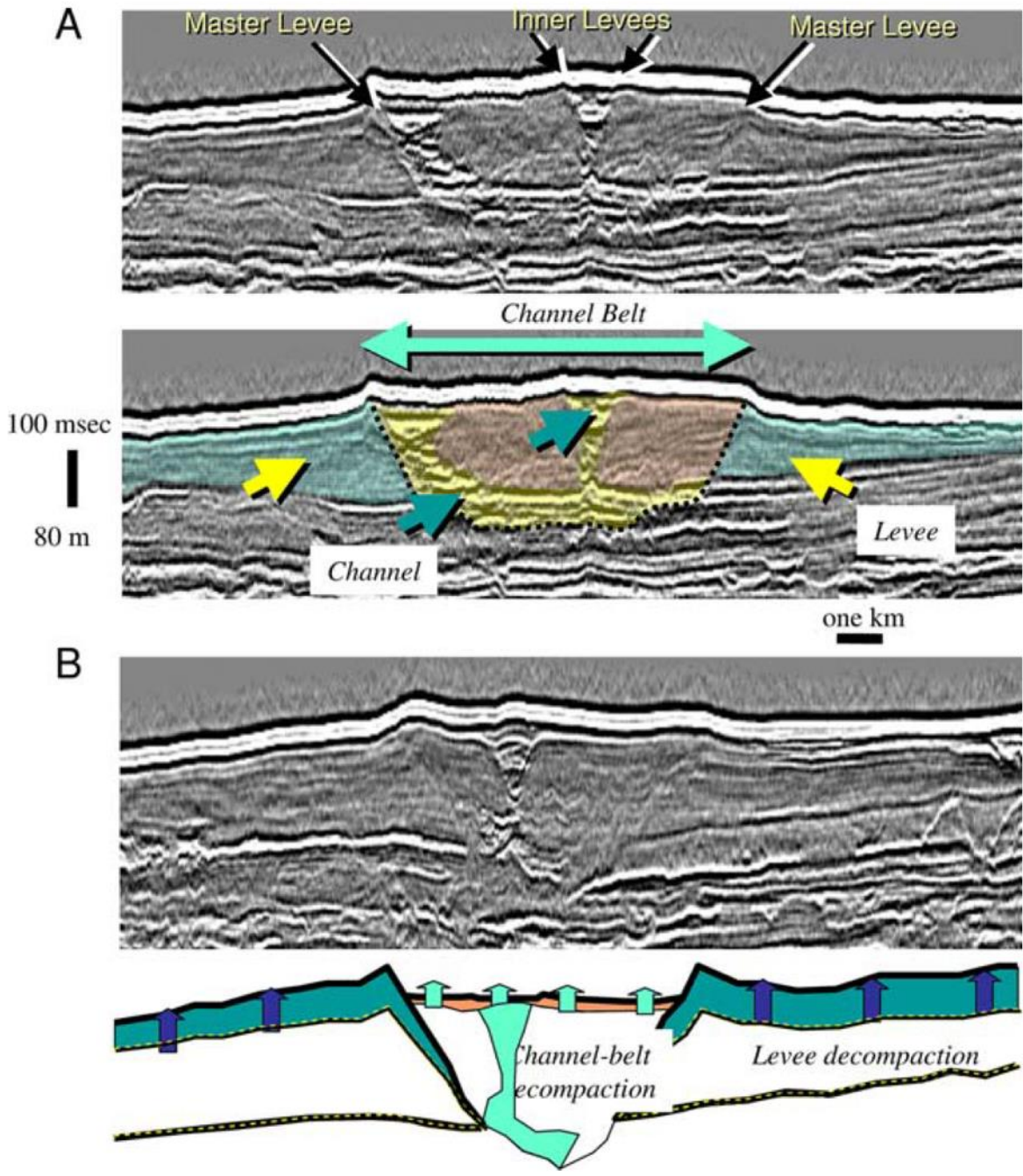


Figure 7. A: Transverse seismic reflection profile across the Joshua channel belt and levee system, marked with master bounding levees as well as the levees bounding the channel (Posamentier, 2003). The channel is probably the most sand prone; the channel belt, less so; the overbank, least sand prone (Posamentier, 2003). B: Interpreted decompacted configuration of the leveed channel system (Posamentier, 2003).

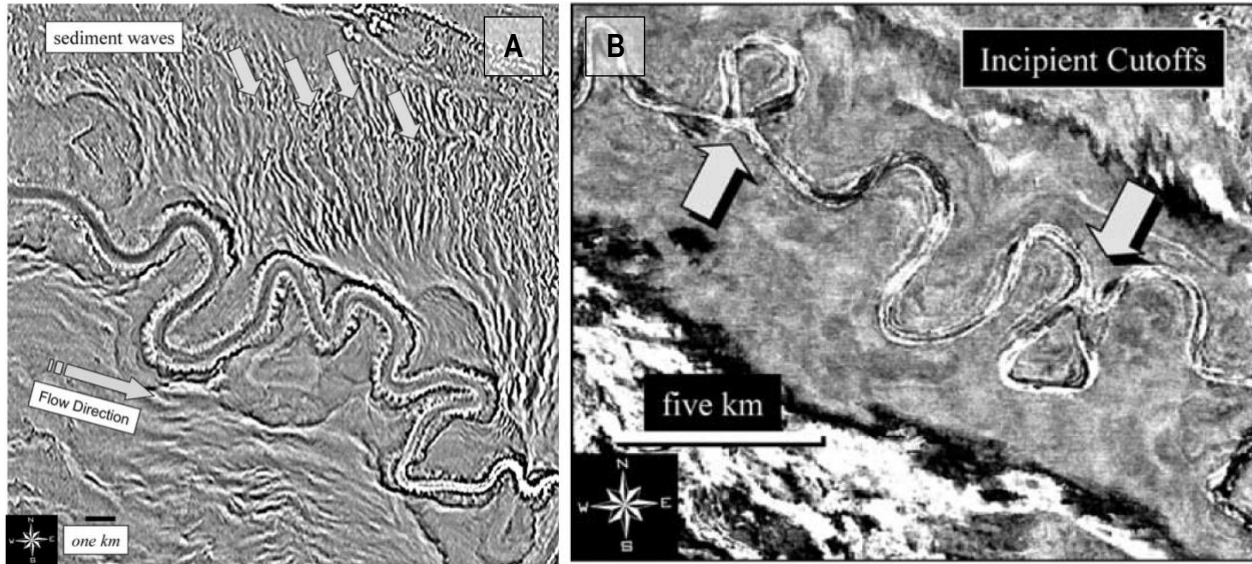


Figure 8. A: Curvature map of upper bounding surface of Joshua channel-levee system, showing overbank sediment waves (white arrows), flow direction (dashed arrow), and slump scars on the inner flank of the levee (Posamentier, 2003). B: Cutoffs observed in Joshua Channel (Posamentier, 2003).

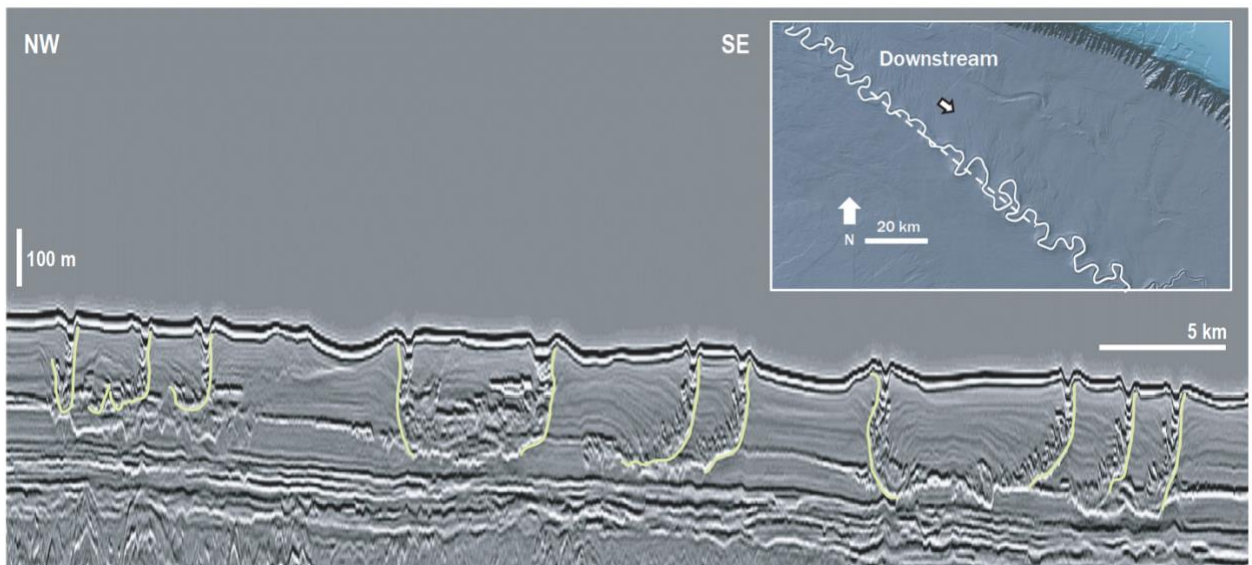


Figure 9. Seismic dip cross section from Kramer et al. (2016), with location (dashed line) on a bathymetric map from Kramer and Shedd (2017). The outlines of “J” shaped channel stacking patterns associated with downstream migration are annotated in yellow.

A highly sinuous, undisturbed channel with a classic channel-levee geometry, the Joshua Channel is an excellent example of a channel-levee system. The features of the channel have been described at length by Posamentier (2003) and its geometric attributes, by Shumaker et al. (2018). Shumaker et al. (2018) compare the geometric attributes of an array of 36 modern channels in high-resolution bathymetry. The results suggest that the geometric characteristics of

Joshua Channel are representative of many sinuous submarine channels. The sinuosity of Joshua Channel (2.1) was in the top 14% of the 36 channels studied by Shumaker et al. (2018). Shumaker et al. note that Joshua Channel maintains a remarkably steady width for its entire mapped length, deviating by only 15% to 25% from its median width. The aspect ratio decreases from approximately 1:100 upstream to approximately 25:1 downstream. The trend of aspect ratio decreasing downstream is commonly observed in other channels, and attributed to an inverse relationship between flow discharge and channel distance compared to fluvial channels (Shumaker et al., 2018). The depth of Joshua Channel was also low compared to the other studied channels, although this may relate more to late stage channel-filling debris flows and partial burial upstream than to the primary mechanics of the channel. Compared to channels in the western Gulf of Mexico, which traverse highly variable slope gradients resulting from salt tectonics, Joshua Channel crosses a relatively stable slope gradient with little influence from salt tectonics (Fig. 4). The relatively high sinuosity and well-defined meander bends of Joshua Channel make it an ideal candidate for the study of the planform kinematics of submarine channels. While Joshua Channel may not be representative of channels traversing highly variable topographies, understanding the geometry of a channel with relatively few disturbances may help the interpretation and modeling of increasingly complex channel systems.

Chapter Three: Methodology

This study uses the curvature-migration model of Howard and Knutson (1984), as implemented by Sylvester et al. (2019), to analyze submarine channel geometry derived from both seismic and bathymetry data. The data and code used by Sylvester et al. (2019) are available at <https://github.com/zsylvester/curvatureepy>. The adaptations of this code for the Joshua Channel are available at: <https://github.com/indrealman/Thesis>. The second part of this study is based on the qualitative analysis of reservoir connectivity in a seismic cross section of Joshua Channel and its potential effect on the viability of analogous deepwater reservoirs.

In this study, the approach of Sylvester et al. (2019) that looked at the relationship between migration rate and curvature of fluvial channels was adopted and applied to 3D seismic data and bathymetric data from the Joshua Channel. Sylvester et al. (2019) apply their simple kinematic model to 30 years of time lapse satellite imagery of quickly migrating rivers in the Amazon Basin. They calculate migration rates using a dynamic time warping algorithm (e.g., Lisiecki and Lisiecki, 2002) that correlates each point along the first channel centerline to the closest point on the second centerline. Interpreting geometries in 3D seismic data as proxies for time lapse data, in this study I also calculate migration rates with a dynamic time warping algorithm, correlating each point along the first channel centerline to the closest point on the second centerline.

Contour maps were generated in the GIS application QGIS from four key horizons extracted from the 3D seismic data set. QGIS is a free software program for geography professionals that provides similar functions as ArcGIS. The horizons represent interpretations of channel base surfaces, and they were interpreted using a dataset provided by Spectrum Geo (now TGS) by Jacob Covault (Fig. 10). The horizons were labeled in the following order: Horizon 1 (youngest), Horizon 2 (second youngest), Horizon 3 (second oldest), and Horizon 4 (oldest). As no absolute age data are available for these horizons, migration distance rather than migration rate is tracked. The horizons were uploaded into QGIS 3.4 as x, y, z coordinates in UTM zone 15N. The x, y, z points were then color coded by depth with a custom color gradient that highlighted local topographic lows rather than the overall channel slope, and then an image (raster) of the shading was extracted for legibility. More significantly, contour data on QGIS was created from the points. The contours were generated in 2, 3, and 4 meter increments for each seismic horizon. The 2-meter contour interval was largely used for horizons 1 and 2, but as data

becomes noisier at depth, the 4 meter spaced contours were more often employed. In order to prevent bias in interpretation, the first few versions of centerlines were interpreted individually at each depth, only displaying one centerline at a time. In QGIS, shapefiles for interpreting the thalweg (or centerline) were generated using contour data. Where contour data was incomplete (as in horizons 3 and 4), the centerlines were interpreted conservatively, following the simplest paths between the centerlines informed by the contour plots. The bends with incomplete contour information for Horizon 3 are bends 14, 15, 17, 29, and 46. Bends with no contour information for Horizon 3 (but nevertheless interpreted from seismic data) are bends 47-56. For Horizon 4, contour data was incomplete for bends 48, 50, and 52-4, and unavailable for bends 55 and 56.

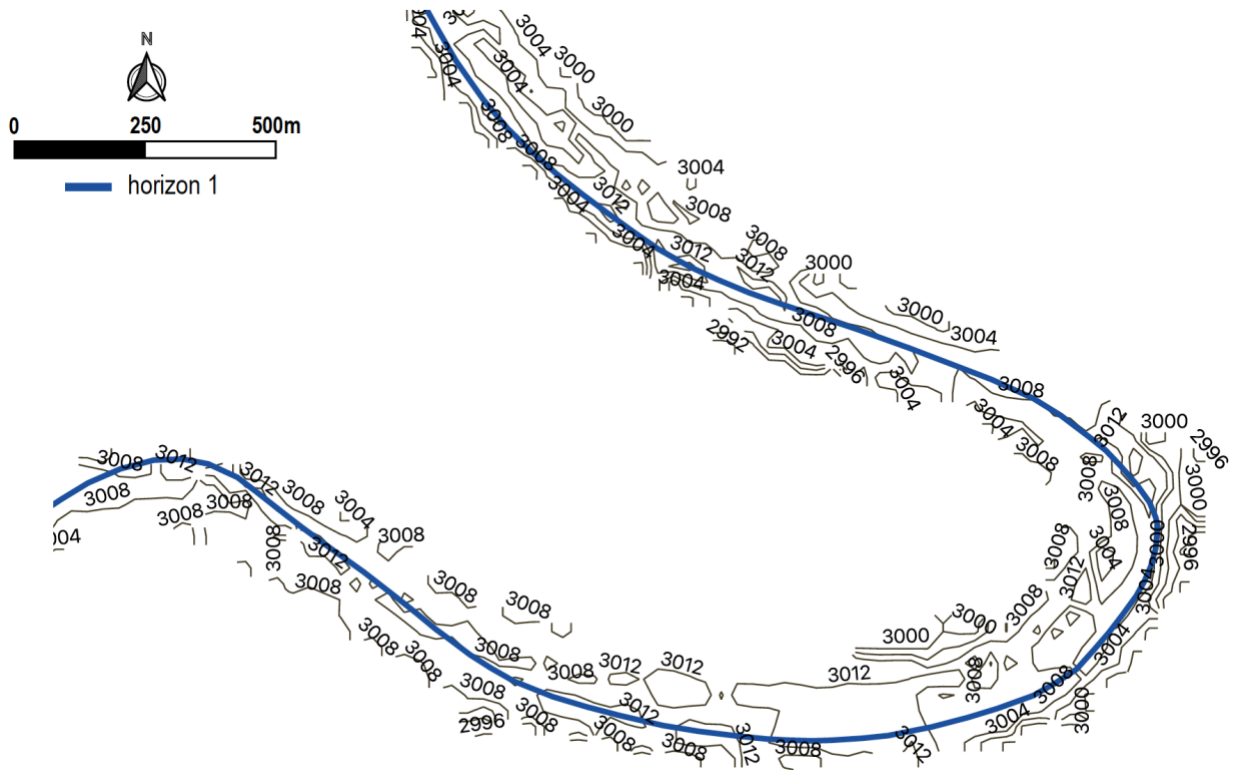


Figure 10. Example of a contour map with 4 meter spacing for horizon 1 on a bend of Joshua Channel. Three different contour maps were used for horizon 1, describing topography in 2, 3, and 4 m increments respectively.

For a map view of the data set, seismic horizon slices at four different depths were also visualized in QGIS. The high-resolution horizon slices were provided by Jacob Covault, and correspond roughly to the horizon contour data. “PSlice0_004” was taken at the shallowest depth and roughly corresponds with Horizon 1, and “PSlice0_006”. roughly corresponds with Horizon 2. “PSlice0_010” was taken at maximum depth, and roughly corresponds to Horizon 3 and

Horizon 4. For example, “PSlice0_010” resembles the 3D seismic map in Kramer et al. (2016), although the map by Kramer et al. depicts the channel at greater depth, with horizon 4 roughly corresponding with the youngest channel on the map (Fig. 11). The overall movement of channel bends are visible in the manner in the horizon slices used. For example, in Figure 11 the channel positions prior to horizon 4 are noticeable.

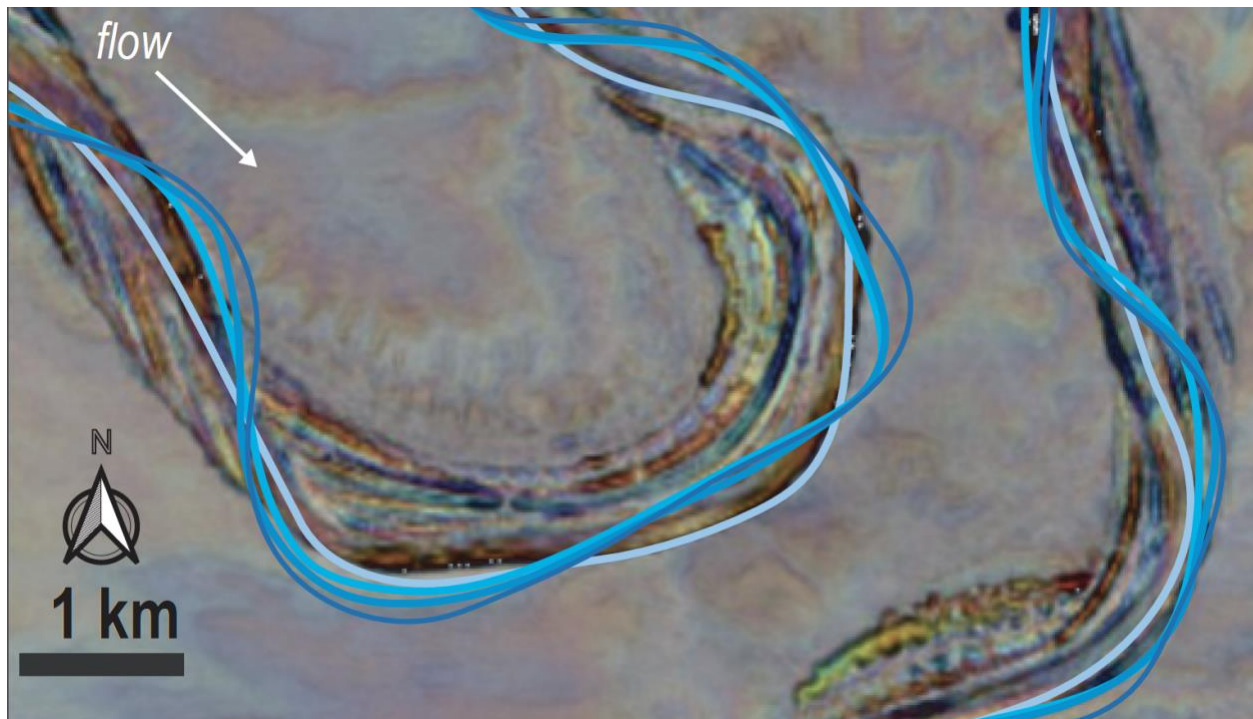


Figure 11. A section of a 3D seismic map roughly resembling horizon slice “PSlice0_010”, although reflecting channel positions at even great depths (Kramer et al., 2016). Interpreted centerlines are depicted, with youngest centerlines in dark blue and the oldest in light blue, and flow direction is noted in white. The centerline of horizon 4 roughly corresponds with the youngest channel presented here. The geometry in visible in seismic horizon slices aided the interpretation of channel centerlines.

In order to ensure accurate and precise correspondence with the centerline interpretations, the horizon slices were georeferenced with 14 points spread evenly across the map (the mean error for the georeferencing was 6.013×10^{-10} m). The horizon slices provided context for centerline interpretations. After the contours were interpreted and final centerlines were color coded and displayed together, the trends in channel movement and geometry in the horizon slices were compared to those suggested by the centerlines. Centerlines that were not in agreement with the trends suggested by map view were adjusted accordingly. On QGIS only the centerline and contours of one horizon would be visible at a time while centerlines were interpreted, and the most dominant and continuous topographic lows were followed. 3D seismic images were

placed in the background during the final editing round in order to add context for interpretation. Centerlines for horizons 3 and 4 (representing the oldest channel histories) do not cover the full portion of the channel, only covering areas where thalwegs could be interpreted with a moderate degree of confidence.

To gather an impression of the amount of aggradation taking place between horizons, rough estimates of “aggradation height” were derived by calculating the difference between channel depths of two examined horizons. The channel depths were calculated by averaging the depths of the first and last bends of each particular time step. Historical aggradation amounts (particularly in muddy units and at great depths) were likely significantly higher, as this measurement does not account for compaction. “M/A” summarizes the relationship between migration and aggradation in a dimensionless ratio of migration distance to aggradation height. Although a rough estimate, this metric provides a general idea of the distance in depth between seismic horizons.

After the centerlines were interpreted, their UTM coordinates were exported into a computational notebook environment called Jupyter Notebook (Kluyver et al., 2016). From there, the code from Sylvester et al. (2019) was adapted to compute the migration distance instead of migration rate. This analysis was conducted for the three consecutive time steps, as well as for three additional time steps. The consecutive time steps are named: time step 1 (from Horizon 4 to Horizon 3), time step 2 (from Horizon 3 to Horizon 2), timestep 3 (Horizon 2 to Horizon 1), and time step 4 (Horizon 1 to the seafloor). Time step 4 is analyzed and discussed as part of the half-width analysis to corroborate results from the seismic analysis with those of the bathymetric analysis. Additional analysis was conducted to determine relationships between other combinations of the seismic horizons, in case any particular horizons act as outliers that skew the analysis. These time steps are named time step A (from Horizon 4 to Horizon 1), time step B (from Horizon 4 to Horizon 2), and time step C (from Horizon 3 to Horizon 1). The code for the analysis of the first time step is available in the Appendix.

To estimate the migration distance, two channel centerlines that consist of an unequal number of data points must be correlated. The dynamic time warping algorithm (DTW) implemented in the ‘dp_python’ package was used. The “optimized dynamic programming (dp)/dynamic time warping (dtw)” package (https://github.com/dpwe/dp_python) performs a best-path calculation using the dynamic programming method, in a way that is 500 to 1000 times

faster than the equivalent pure Python. Originally developed for speech recognition and now used in bioinformatics, DTW aligns two sequences that share inconsistent time bases. The DTW algorithm implements vectorization with nested loops, for which Python tends to be inefficient. The core algorithm is written in the C language. The algorithm evaluates the similarity between data as a local cost matrix, through which it finds the lowest cost path to produce an optimal alignment.

For the calculation of the dimensionless curvature (W/R , where W is channel width and R is radius of curvature, the thalweg width rather than “bankfull width” (to borrow fluvial terminology) or levee-crest width was used. The thalweg width was interpreted in high-resolution bathymetric data. Figure 12 depicts thalweg and levee crest width on one bend in the bathymetric dataset. The thalweg width was chosen to normalize curvature because this width is most comparable to the bankfull width of fluvial channels typically used in R/W . Pirmez and Imran (2003) notice that while ratios for $L:R$ (length to radius of curvature) and $L:A$ (length to area) are consistent between fluvial and submarine channels, a large discrepancy between the two channel types exists between their $R:W$ values when bankfull widths are considered (2003). Pirmez and Imran (2003) suggest measuring thalweg width in place of levee crest width wherever high-resolution bathymetry is available. Comparing submarine channel geometries to those of fluvial channels, Pirmez and Imran (2003) find that the measurement and interpretation of thalweg width as opposed to bankfull width leads to agreement between the geometric scaling of fluvial and submarine channels. Levee crest width, often described as the “bankfull” width of submarine channels, may become very wide due to the significant levee aggradation that is often present in submarine channels. Shumaker et al. (2018) note that while submarine channels adapt to discharge changes largely through vertical aggradation, in contrast, fluvial channels, accommodate these changes via widening. In contrast with a fluvial setting, where deposition on high-flow boundaries only occurs during high flow events, in the submarine setting, the dilute portions of gravity flows blanket the levee throughout much of the life of the flow, with relatively little vertical control on aggradation. Pirmez and Imran (2003) interpret the high-velocity core of the flow to account for the erosive potential of the flow and thus “it is the width of this portion of the flow that actively ‘carves’ the channel and shapes the meandering planform”. While thalweg width is generally more difficult to discern than levee crest width, this study benefits from the high-resolution bathymetry that allows a reasonable interpretation of

thalweg boundaries. The detailed process of obtaining an estimate of thalweg width for Joshua Channel is described below.

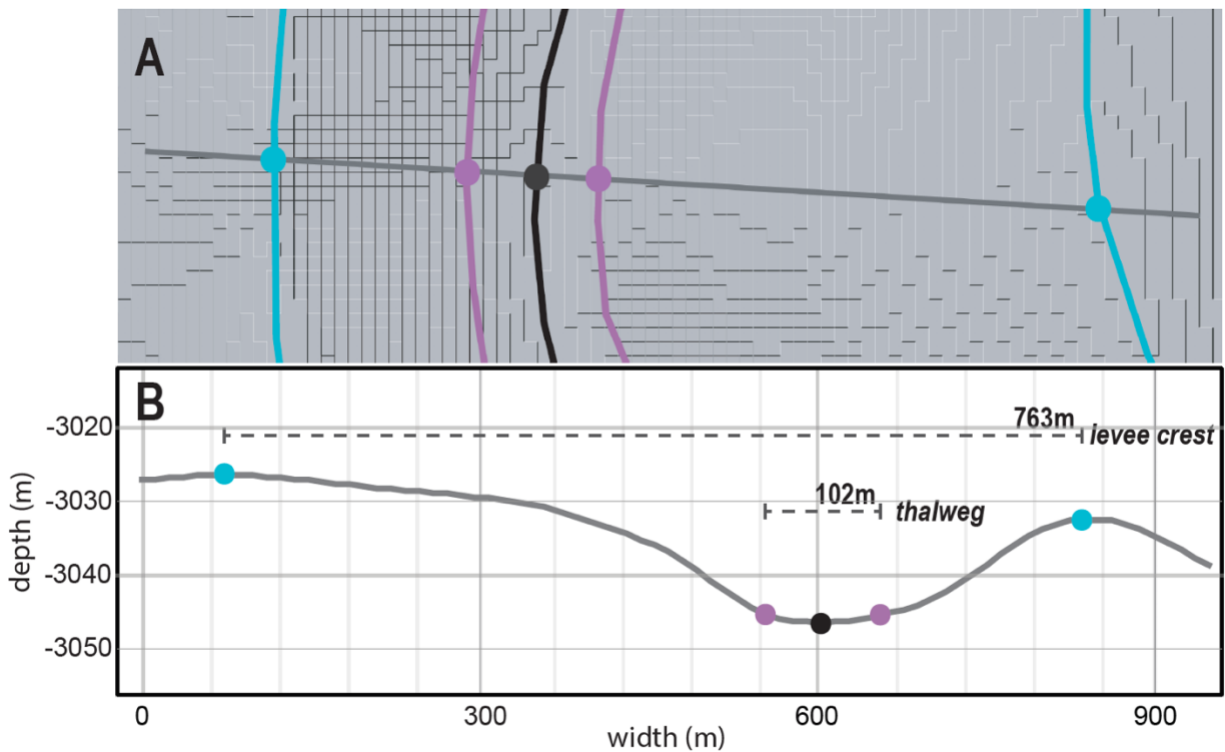


Figure 12. Two different interpreted channel widths: “levee crest” width (denoted by aqua boundaries) and “thalweg” width (by green boundaries). A: The widths in birds eye view on bend #29 with coordinates from the bathymetric map. B: The widths in a cross section of the bend with its corresponding terrain profile. The shorter, deeper thalweg width is thought to correspond with the highest energy portions of the flow. Levee crest width (763 m above) has been commonly used as a comparison to fluvial bankfull width, although Pirmez & Imraz (2003) assert that thalweg width (102 m above) here offers a more appropriate comparison. The light blue boundaries in A correspond with another measured width that is not used in this analysis.

To investigate the relationship between half-width and curvature, publicly available high-resolution bathymetric data of the Joshua Channel from the Bureau of Ocean Energy Management (Kramer and Shedd, 2017). Integrating over one hundred 3D seismic time-migrated surveys, the entire Gulf of Mexico dataset covers water depths of -40 to $-3,379$ m with an average error of 1.3 percent of water depth (Kramer and Shedd, 2017).

To process and analyze bathymetric data, QGIS and Jupyter notebooks are used.

The thalweg and banks were interpreted in a manner similar to the interpretation of seismic data. To determine the boundaries necessary to compute half-width, the highest topographic points that closely followed the curvature of the channel were selected. To map the

channel centerline the lowest topographic points were selected. The lines were visually smoothed by dragging points to eliminate noise from unwanted features (i.e., unexplained ‘potholes’ along the thalweg or likely erosional features in the banks).

Smoothing in QGIS was preferable to smoothing only in the code, because it made it possible to identify potential extraneous features affecting topography that were not related to curvature or true bank boundaries (i.e., ‘potholes’ that are likely to be noise or bank failures). This smoothing in QGIS would also prevent the curvature from flipping from positive to negative excessively (which may happen if a single point is out of place).

In Jupyter Notebook, the interpreted bank boundaries and centerlines were loaded as CSV files and geometric attributes of the channel were computed in Python. Correlations between left and right banks, half-width, and centerlines were computed using the code provided by Sylvester et al. (2019) for fluvial channels.

The first and second derivatives of the curve or centerline were computed using Cartesian coordinates and returned the cumulative distance along the curve or centerline. The curve was then resampled with a bicubic spline interpolation, and the dynamic time warping algorithm correlated the curves. To smooth the curvature data series, a Savitzky-Golay filter was used, with a smoothing factor of 51 (Fig. 13). To compute half-width values, the left and right bank widths were defined as the distances between the centerline and the left bank and right bank respectively. These series were also resampled and smoothed.

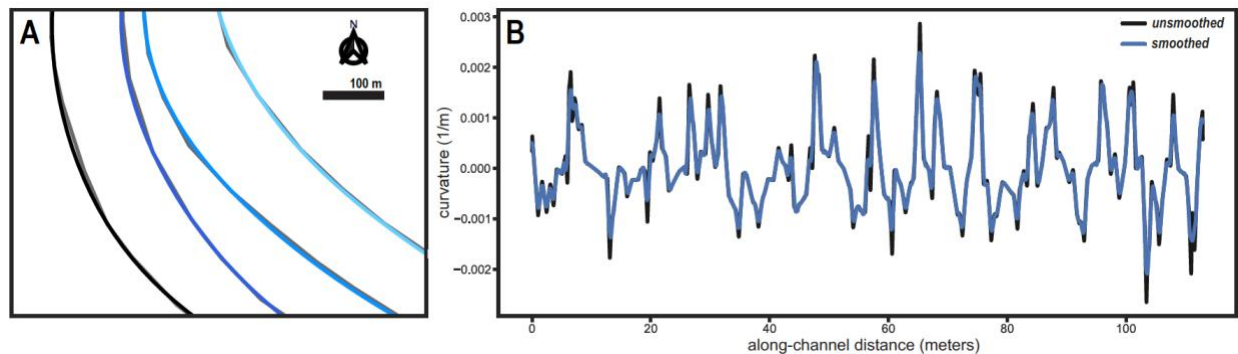


Figure 13. A: Smoothed centerlines in color over original centerlines in black. Each unsmoothed centerline is composed of x, y coordinates that require smoothing before curvatures are computed. Smoothed horizons are in black (Horizon 1), navy blue (Horizon 2), teal (Horizon 3), and aqua (Horizon 4). B: Resulting raw and smoothed curvature for Horizon 4. “Unsmoothed” curvature refers to the curvature that was measured from the vertices of the interpreted shapefiles. “Smoothed” curvature was generated using a Savitzky-Golay filter, with a smoothing factor of 51.

To compare half-width and curvature, the right bank width was selected to function as the half-width and the smoothed curvature series were used. After comparing curvature and half-width on a plot, the lag between the two was computed (a positive lag would suggest that curvature follows migration or half-width, while a negative lag would suggest that half-width or migration follows curvature). The lag is first computed as the median difference between points of zero curvature and zero migration, and this number is adjusted to maximize the Pearson correlation between curvature and migration. The points of zero curvature and zero migration are detected in Python, after which several are deleted so that only one inflection point for each variable exists per bend for each timestep.

The code used in the analysis of half-widths and the centerline of bathymetric data is highly similar to the code written for the analysis of seismic centerlines (Appendix). The main difference is that for the analysis of “half-widths”, the left and right bank boundaries were imported as shapefiles and that the right bank width was used in place of migration distance.

This paper also explores the economics of submarine channel reservoirs by qualitatively analyzing factors affecting the connectivity of deepwater reservoirs such as mud drapes, lateral migration, and stacking patterns. The discussion will not provide precise estimates for the economic value of “connected” versus “less connected” reservoirs. However, this will offer geologists and financial analysts alike an appreciation of the particular ways in which depositional architecture might impact financial outcomes.

Chapter Four: Results

Analysis of Seismic Data

As was expected based on planform patterns visible in 3D seismic maps, the behaviors of the interpreted centerlines are dynamic. (Fig. 14A). At first glance, patterns of swing and sweep are visible in several bends (Fig. 14B). Two cutoffs are also visible. Channel sinuosity appears to increase over time, with the youngest centerline noticeably more sinuous than older centerlines.

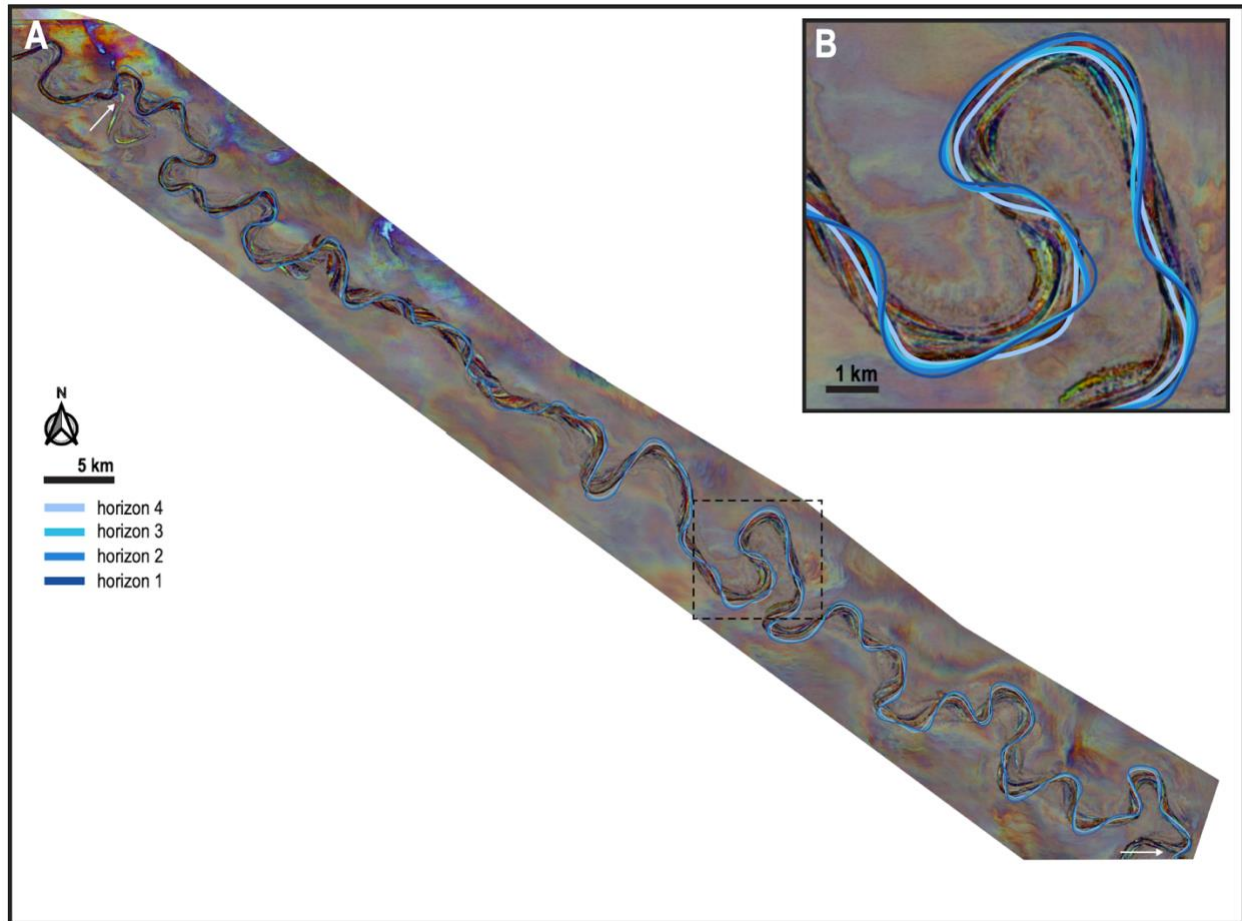


Figure 14. A: A map generated from 3D seismic data overlaid with the four centerlines that were interpreted in QGIS. Centerlines are color-coded by age, from light blue (oldest) to dark blue (youngest). Two cutoffs are observed (white arrows). Map provided by the BOEM (Kramer et al., 2016). B: A close up view of the bend outlined in dashed lines.

The annotated bends for each time step are displayed in Figures 15 and 16, following the approach outlined by Sylvester et al. (2019). Locations of zero curvature are plotted along older horizons. Curvature inflection points precede the corresponding zero migration points in all bends. Inflection points that do not exist across all horizons (which appear to result from the

formation or evolution of compound bends) are not plotted, in order for bend assignments to remain consistent across horizons.

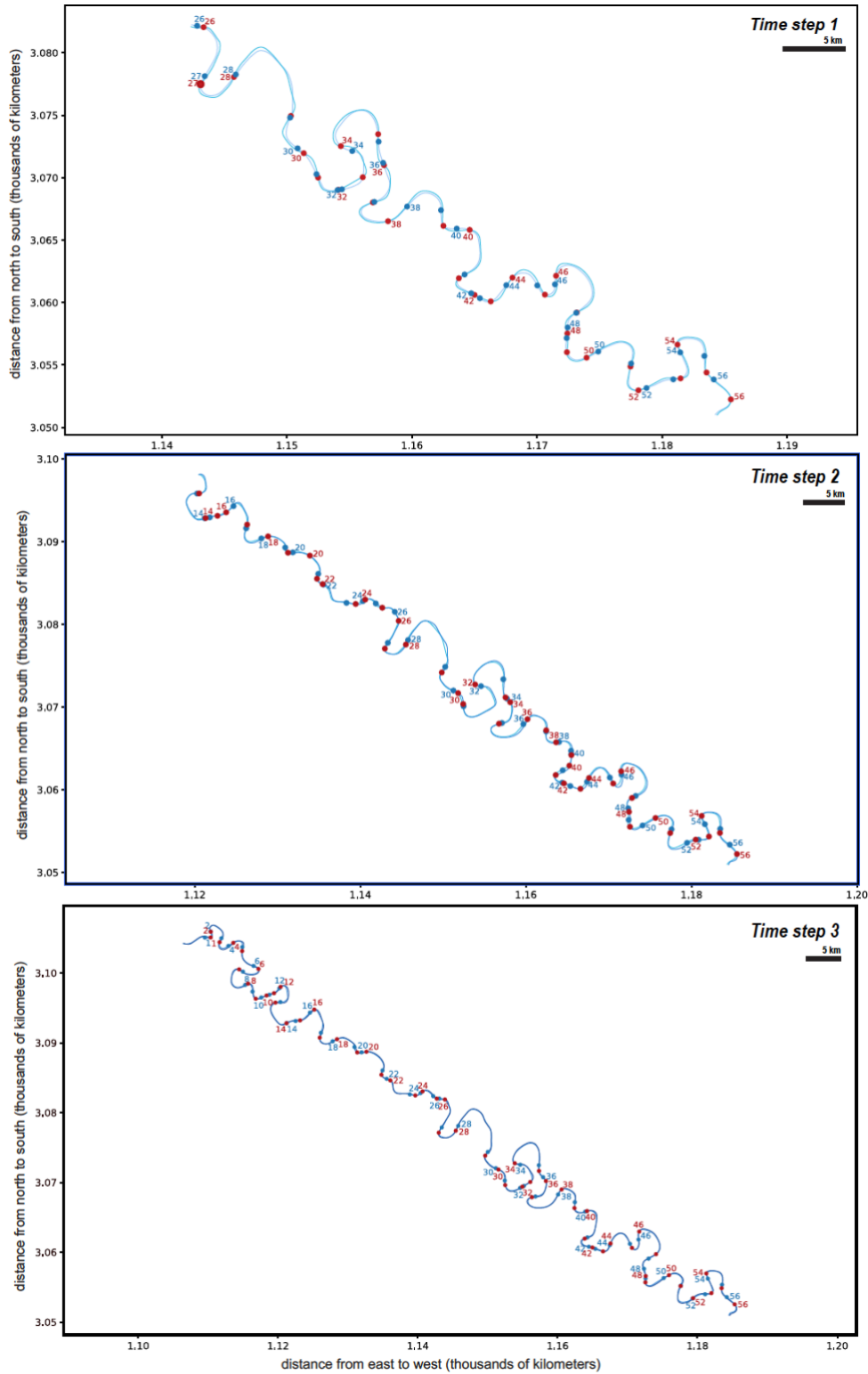


Figure 15. Maps of locations of zero migration (red) and of zero curvature (teal) across time steps 1, 2, and 3, with every other bend labeled. A (top): time step 1, from Horizon 4 (light blue)

to Horizon 3 (aqua). B (middle): time step 2, from Horizon 3 (aqua) to Horizon 2 (medium blue). C (bottom): time step 3, from Horizon 2 (medium blue) to Horizon 1 (indigo). Locations of zero curvature are plotted the older horizon, and indicate the upstream boundary of the bend that matches their annotations. Inflection points that are inconsistent across all horizons (which appear to result from the formation or evolution of compound bends) are not plotted.

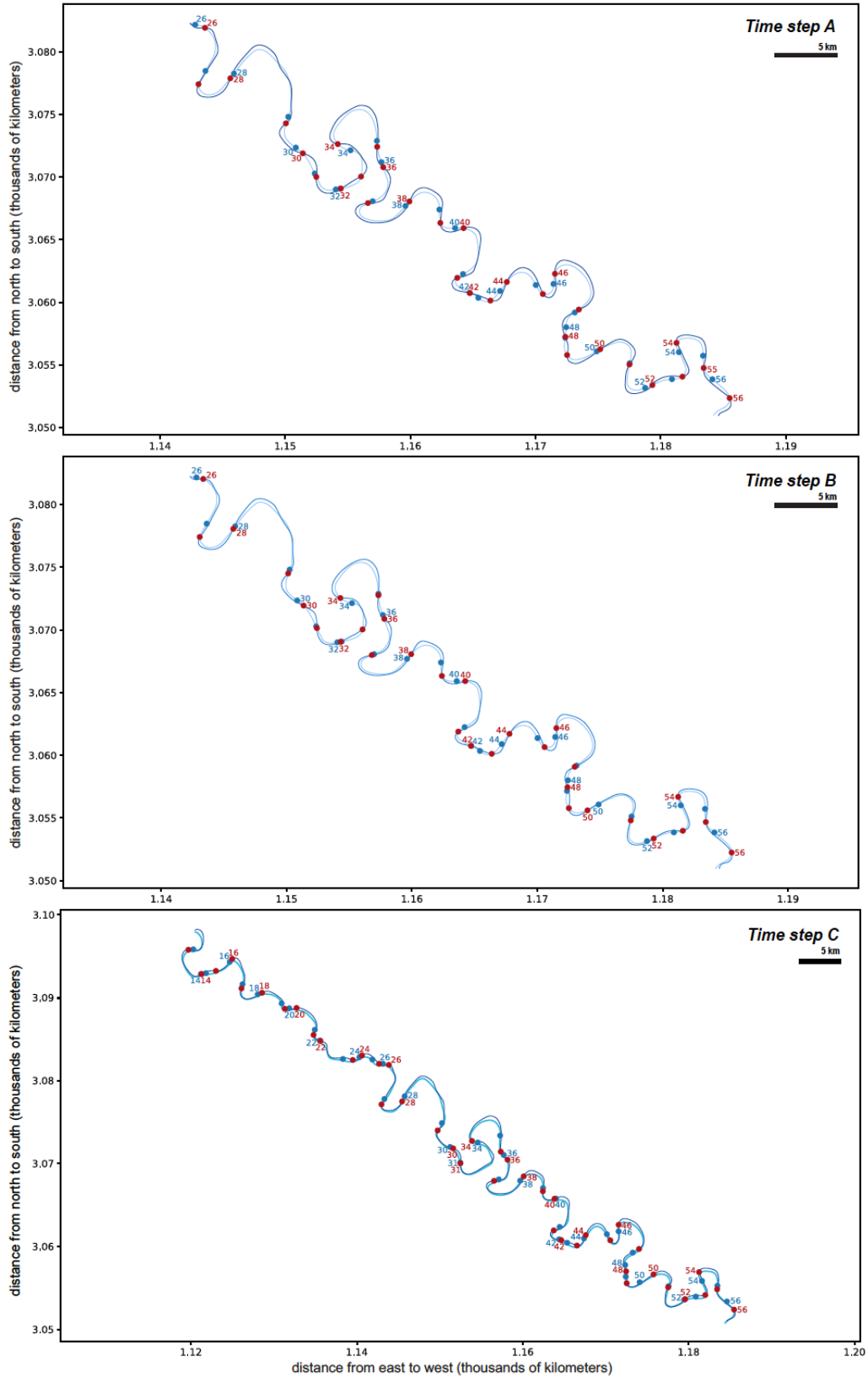


Figure 16. Maps of locations of zero migration (red) and of zero curvature (teal) for time steps A, B, and C, with every other bend labeled (except for in the case of bends 31 and 34 in Fig. 11c,

because bends 32 and 33 were not detected in time step C). A: time step A, from Horizon 4 (light blue) to Horizon 1 (indigo). B (middle): time step B, from Horizon 4 (light blue) to Horizon 2 (medium blue). C (bottom): time step C, from Horizon 3 (aqua) to Horizon 1 (indigo).

Figures 17 and 18 summarize the findings of this study. Denoting curvature and migration changes along the channel and shading them by bend, one may notice a small, consistent lag between curvature (teal) and migration (red) in the time series plots (Fig. 17; Fig. 18).

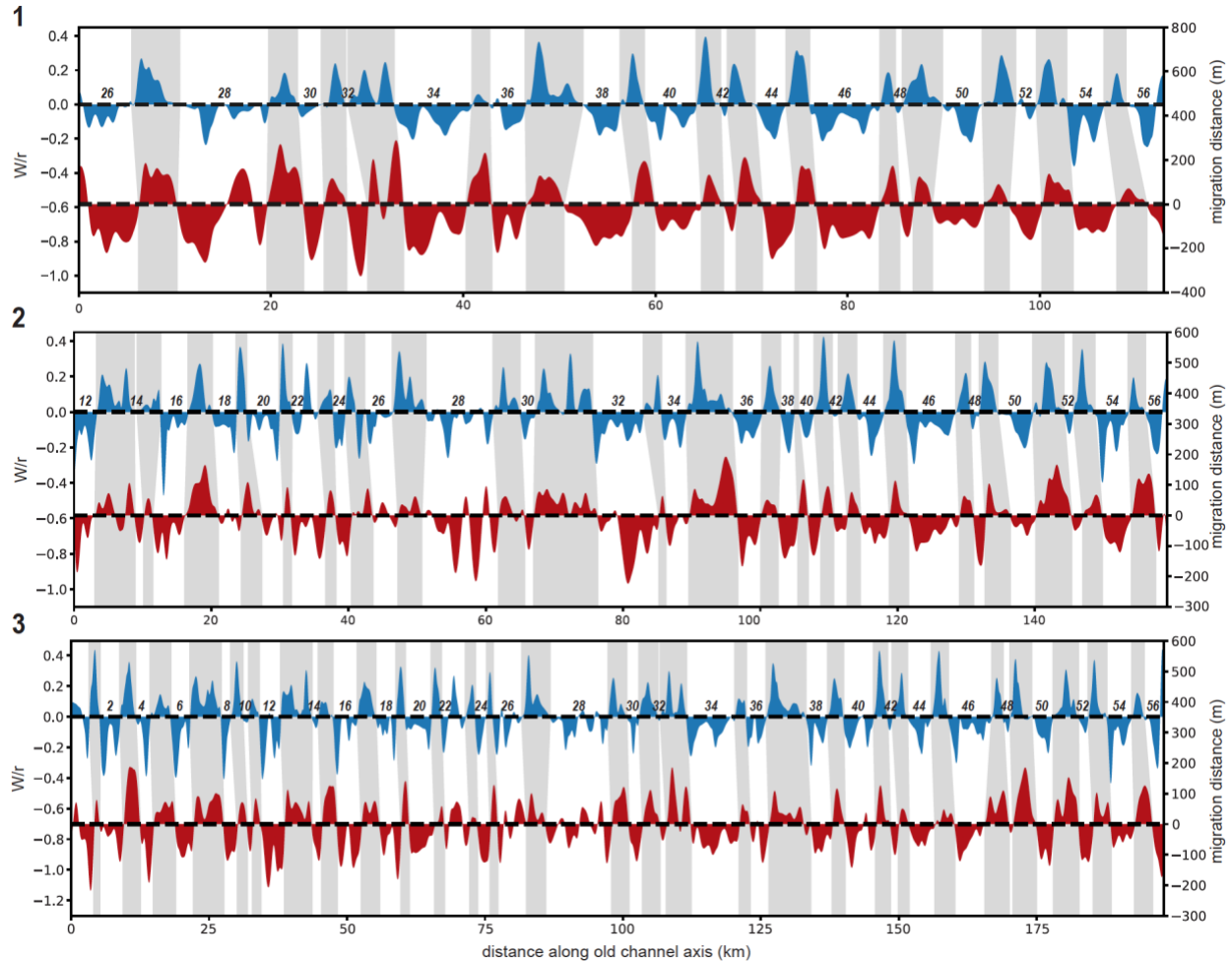


Figure 17. Curvature (expressed as width / radius of curvature) in teal and migration distance in red variations for each timestep. 1: Time step 1, from Horizon 4 to Horizon 3. 2: Time step 2, from Horizon 3 to Horizon 2. 3: Time step 3, from Horizon 2 to Horizon 1. “Bends” are numbered and shaded by curvature sign, with beige (-) and white (+). Bends were picked using an inflection point algorithm which tracked curvature inflection points. Some bends were combined with neighboring bends for this classification for ease of interpretation, so that new or disappearing bends would not leave the classification inconsistent across timesteps. The small but significant deflection in the shading that leans to the right illustrates the lag between curvature and migration distance.

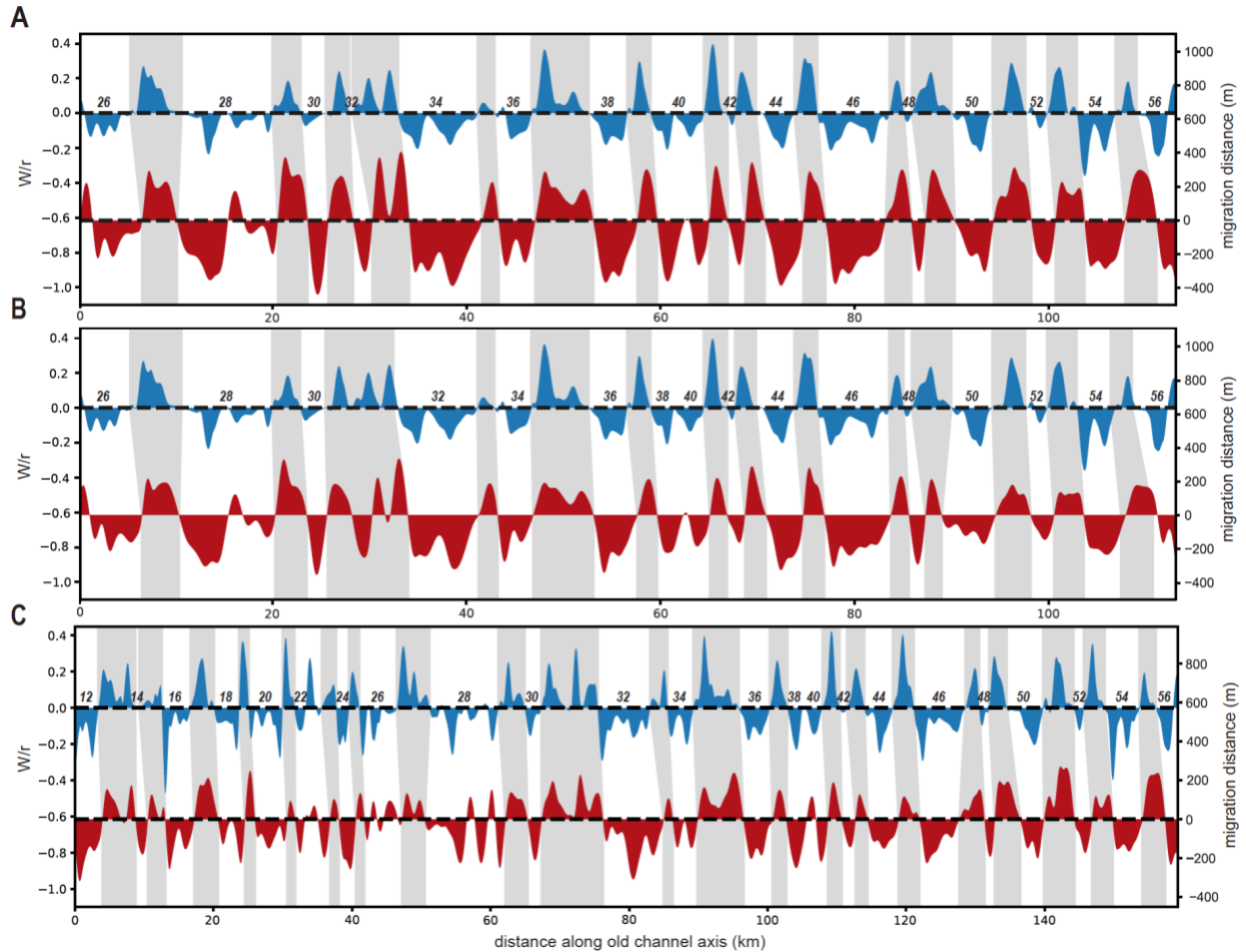


Figure 18. Curvature (expressed as channel width/radius of curvature) in teal and migration distance in red for each timestep. A: Time step A, from Horizon 4 to Horizon 1. B: Time step B, from Horizon 4 to Horizon 2. C: Time step C, from Horizon 3 to Horizon 1.

Migration appears to follow curvature by a small but consistent phase lag (Figs. 17 and 18). The trends in migration distance for each bend appear to mimic the trends in curvature. Bends are defined by inflection points that were identified automatically, but were adjusted to group new or disappearing bends together that would alter the total number of bends across timesteps. The analysis is not affected by the annotated assignments of bends. The bends are numbered and shaded only for the purpose of interpretation. Some bends visibly expand during time steps: bend 28 (a complex compound bend) expands in each time step (Fig. 17, Fig. 18, Fig. 19). Other bends, such as bends 37 and 49 (Fig. 13a), appear to tighten, with migration distance changing direction before the downstream boundary of the bend. While the lag appears throughout many of the bends shown in Fig. 18a-c, it is displayed most consistently in Fig. 18a,

which describes the cumulative time step between Horizon 4 (for which only the downstream portion is available) and Horizon 1.

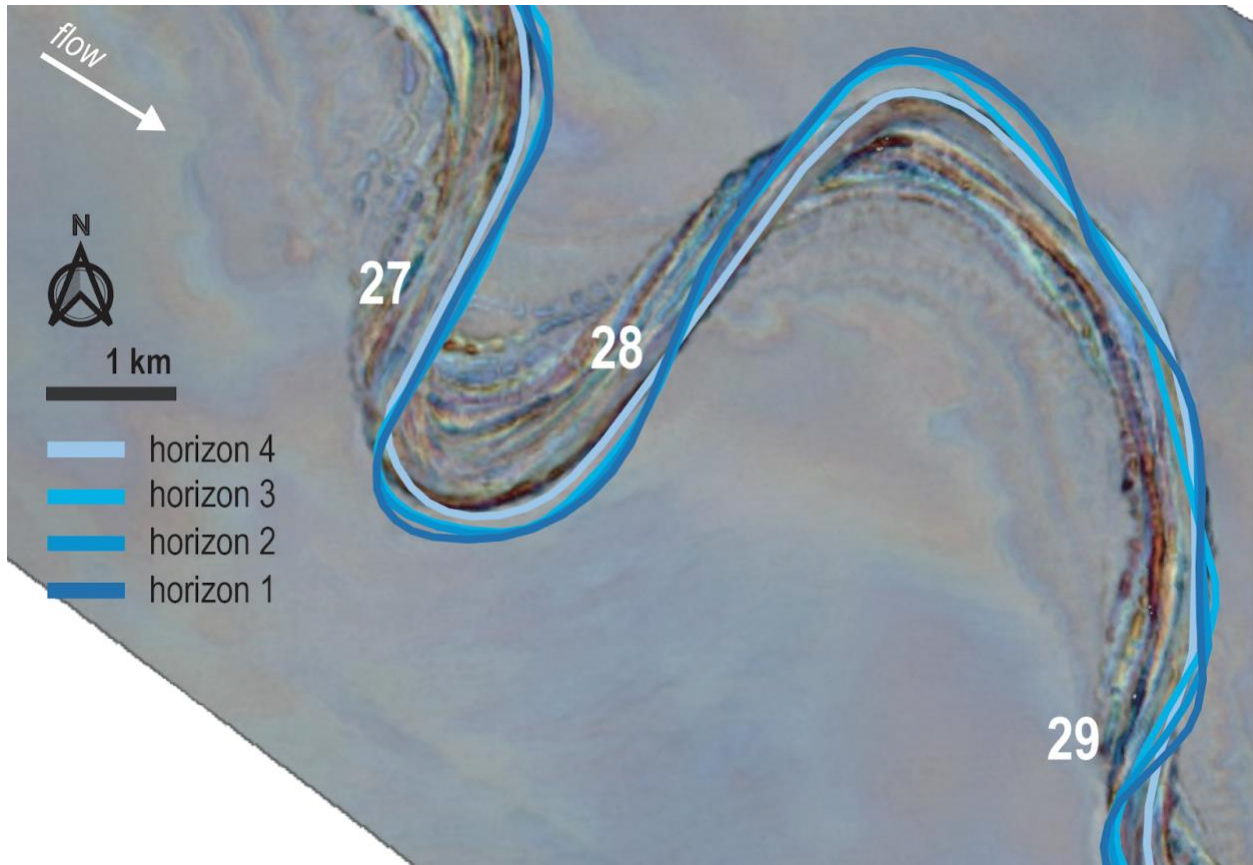


Figure 19. One segment of the channel (bends 28) overlaid with interpreted centerlines (unsmoothed) for seismic horizons 1-4 seen on a 3D seismic map. Flow direction (white arrow) and bends (white, by the upstream boundary of the bend) are marked. The lengthening of bend 28 (in both channel axis length and “point bar” width) appears to coincide with the amplification of curvature anomalies within the compound bend. Map displays a deeper portion of the channel than interpreted by the centerlines, and is available from the BOEM (Kramer et al., 2016).

The analysis suggests that curvature and lagged migration distance correlate relatively well (Fig. 20). The coefficients of determination (r^2) show that variation in curvature explains 40% of variation in migration distance in time step 1, 35% of variation in time step 2, and 57% of variation in time step 3. For the cumulative timesteps, variation in curvature explains 61% of variation in migration distance in time step A, 57% of variation in time step B, and 56% of variation in time step C. The phase lags for time steps 1, 2, and 3 are 675 m, 650 m, and 675 m respectively (Fig. 20). For the additional time steps A, B, and C, the phase lags were 750m, 675m, and 700 m respectively. The mean lag of six timesteps is 688m, with a range of 100m. Data based on incomplete contour data are plotted in orange, and makes up many of the outliers in Figure 21.

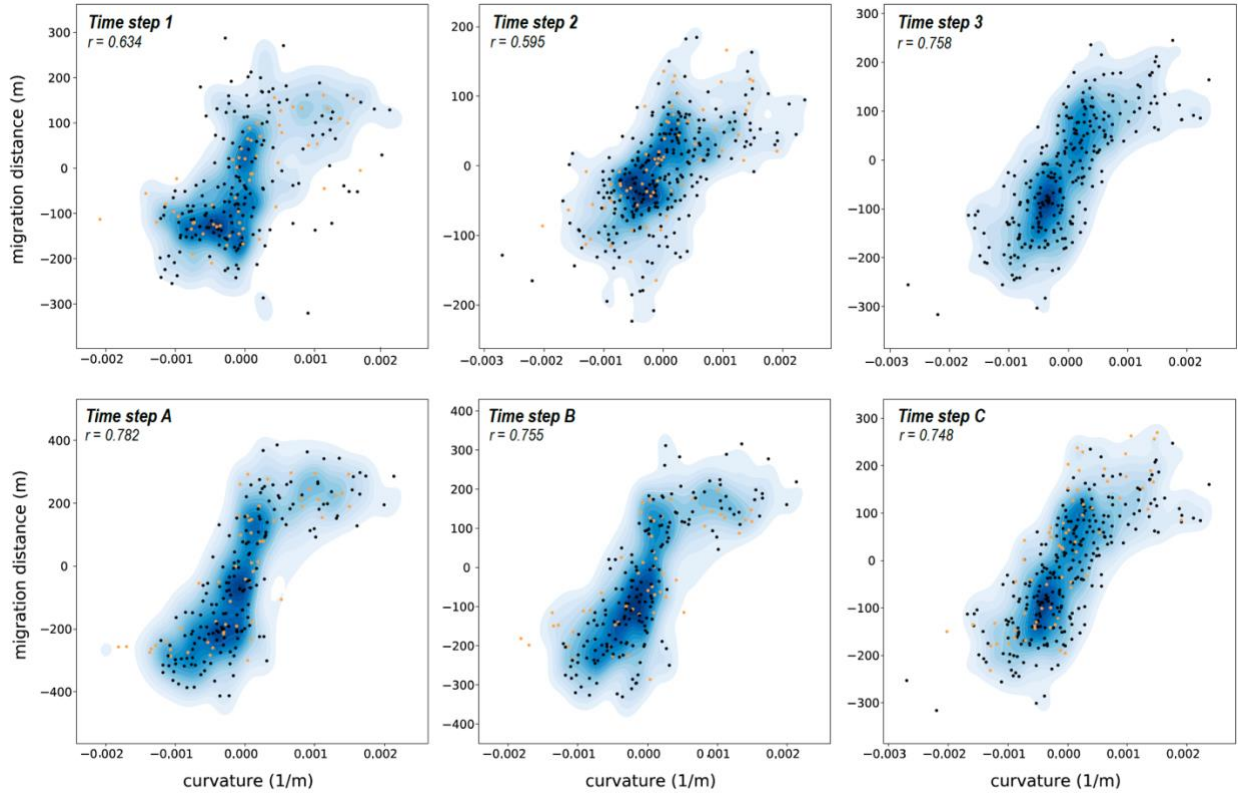


Figure 20. Correlations across seismic horizons between migration distance and curvature when the phase lag is taken into account. Only 5% of data are plotted as points, while areas shaded in blue are bivariate kernel density estimates of all data points. Channel segments with incomplete contour data in horizons 3 and 4 are plotted in orange. Orange data points represent areas where channel trajectories were interpreted based on only channel movements visible in 3D seismic maps rather than on both these and contour maps. A: Timestep 1 (from Horizon 4 to Horizon 3), the Pearson's correlation coefficient ('r') is 0.634 with the phase lag, and 0.460 when no lag is included. B: Timestep 2 (from Horizon 3 to Horizon 2), $r = 0.595$ with the phase lag and $r = 0.375$ without the phase lag. C: Timestep 3 (Horizon 2 to Horizon 1), $r = 0.758$ with the phase lag and $r = 0.406$ without the lag. D: Timestep A (between horizon 4 to Horizon 1), $r = 0.782$ with the phase lag and $r = 0.547$ with no phase lag. E: Timestep B (between Horizon 4 and Horizon 2), $r = 0.755$ with the phase lag and $r = 0.544$ without the phase lag. F: Timestep C (between Horizon 3 and Horizon 1), $r = 0.748$ with the phase lag and $r = 0.436$ without the phase lag.

Correlations were recomputed for timesteps 1 and 2 in order to exclude centerline segments that were interpreted with incomplete data (Fig. 20). For time step 1, the correlation increased from 0.634 to 0.655 and the estimated lag increased to 700m. For timestep 2, the correlation changed from 0.595 to 0.584 and the lag decreased to 625m. When eliminating poor contour data but considering the results of all time steps, $r = 0.720$ with a lag of 679 m, with a range of 100 m, and variance in curvature explains 52% of variance in migration. When eliminating channel segments without contour data and also excluding time step 2 (an anomalous

interval which had a correlation under 0.60), the mean correlation for the six time steps was $r = 0.747$, meaning that variance in curvature explained 57% of variance in migration, and the mean lag was 690m, with a range of 50m.

The inclusion of phase lag in the correlation analysis had a significant effect on the computed correlation between migration distance and curvature. Excluding the phase lag for timesteps 1, 2, and 3, $r = 0.454, 0.375,$ and 0.406 respectively. For the cumulative timesteps A, B, and C, $r = 0.547, 0.544,$ and 0.436 when no phase lag is included. The mean r for the correlations with no phase lag is $r = 0.460$ and the mean r squared is 0.211 (compared to 0.720 and 0.518 with the phase lag). This discrepancy in r values implies that the linear relationship between curvature and migration distance is almost twice as strong when a phase lag is considered. The r squared values indicate that curvature may explain only roughly 21% of variance in migration distance along equivalent channel axis positions, but may explain between 52% of in migration distance from 679 m downstream.

There is a positive, relatively strong linear relationship (with a mean r of 0.720) between curvature and migration distance in the seismic data for Joshua Channel when a lag of approximately 679 m is included and low-quality data are excluded, with curvature explaining roughly 52% of the variance in migration distance.

To compare the lag between deepwater curvature and migration variation to that of fluvial channels, a dimensionless ratio, lag / channel width (L/W), was calculated. Thalweg width and levee crest width were measured, as shown in Figure 12. Both widths have been used in studies of scaling in submarine channels (Pirmez and Imran 2003). The L/W ratio assumes that the distance between points of maximum curvature and maximum migration depends on channel width. For the fluvial study, Sylvester et al. (2019) note that migration is shifted downstream relative to bend curvature by a distance that is 2.1 to 4.7 times larger than the channel width. For Joshua Channel, the lag followed bend curvature by a distance that was 3.6 to 4.2 times larger than the median thalweg width and 0.8 to 1.0 times larger than the median levee crest width (when using the range of lags in Table 2). The lag/channel width ratio of Joshua Channel was remarkably close to, although a bit larger, than the mean of the ratios (3.4) for rivers of the Amazon Basin, when thalweg width was considered in place of levee crest width. When levee crest width was used in place of thalweg width, L/W decreased to 0.90 (which would suggest that the lag distance was lower in magnitude and arguably less significant).

Analysis of Bathymetric Data

Half-width and curvature are linearly correlated ($r = 0.772$) when a phase lag of 250 m is considered, as shown in the kernel density and scatter plot in Figure 21. Variation in half-width follows variation in curvature by a small lag. The lag is less than half that for migration and curvature. Migration distance varies inversely with curvature in time step 4 (between Horizon 1 and the seafloor), with $r = -0.479$ and a lag of 300 m. Migration distance weakly varies with the inverse of curvature, which it lags behind by a small amount (Fig. 22b).

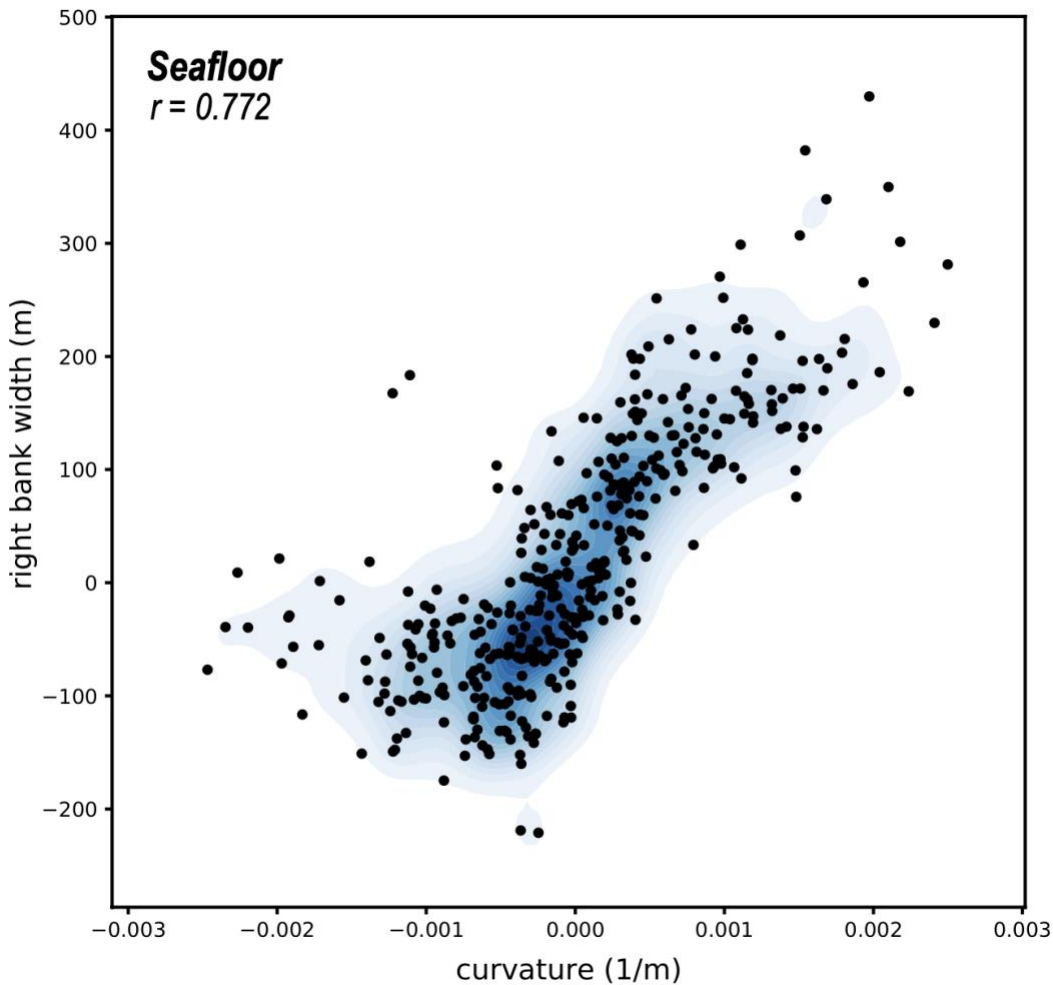


Figure 21. Correlation between half-width, a potential proxy for migration, and curvature. With a phase lag of 250 m between curvature and right bank width, $r = 0.772$; without a phase lag, $r = 0.733$. Only 5% of the data are plotted as points.

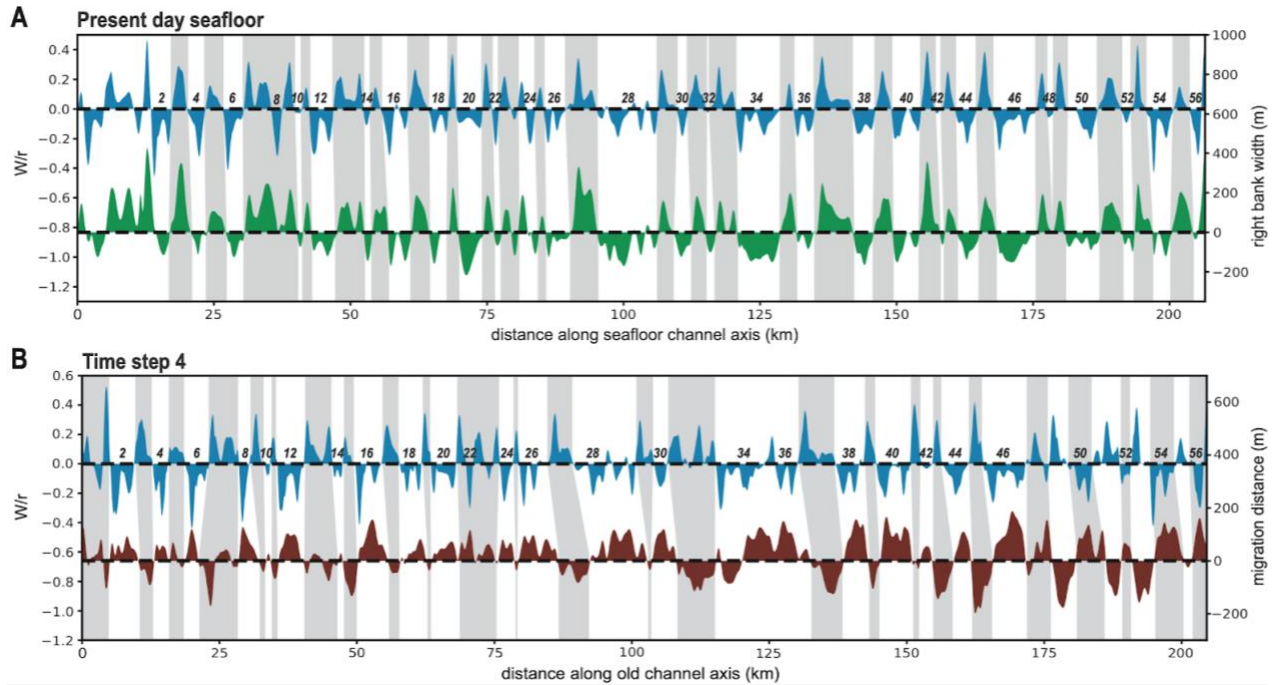


Figure 22. (A) Half-width (green) and curvature (teal) plotted along the axis of Joshua Channel, highlighting deviation from the median value of half-width and from the curvature of 0 (both in black dashed lines). Right bank width is the half-width used here. In some channel segments variation in half-width seems to precede variation in curvature, albeit with a smaller phase lag. (B) Migration distance (red) and curvature (teal) in time step 4 (from Horizon 1 to the seafloor). Migration seems to have the opposite sign compared to curvature, following the inverse trend of other time steps. In other words, the centerline straightens during this step.

The interpreted centerline and high flow bank boundaries of the Joshua Channel are displayed on seafloor bathymetry (Kramer and Shedd, 2017) (Fig. 23). The computed left and right bank widths along with the mean channel half-width are shown along various sections of the channel (Fig. 24). As one might expect when observing the geometry of the center of the channel and the banks, the left bank width and right bank width are inversely related. As with the curvature-migration distance series, a small lag exists between curvature and right bank width (Fig. 22).

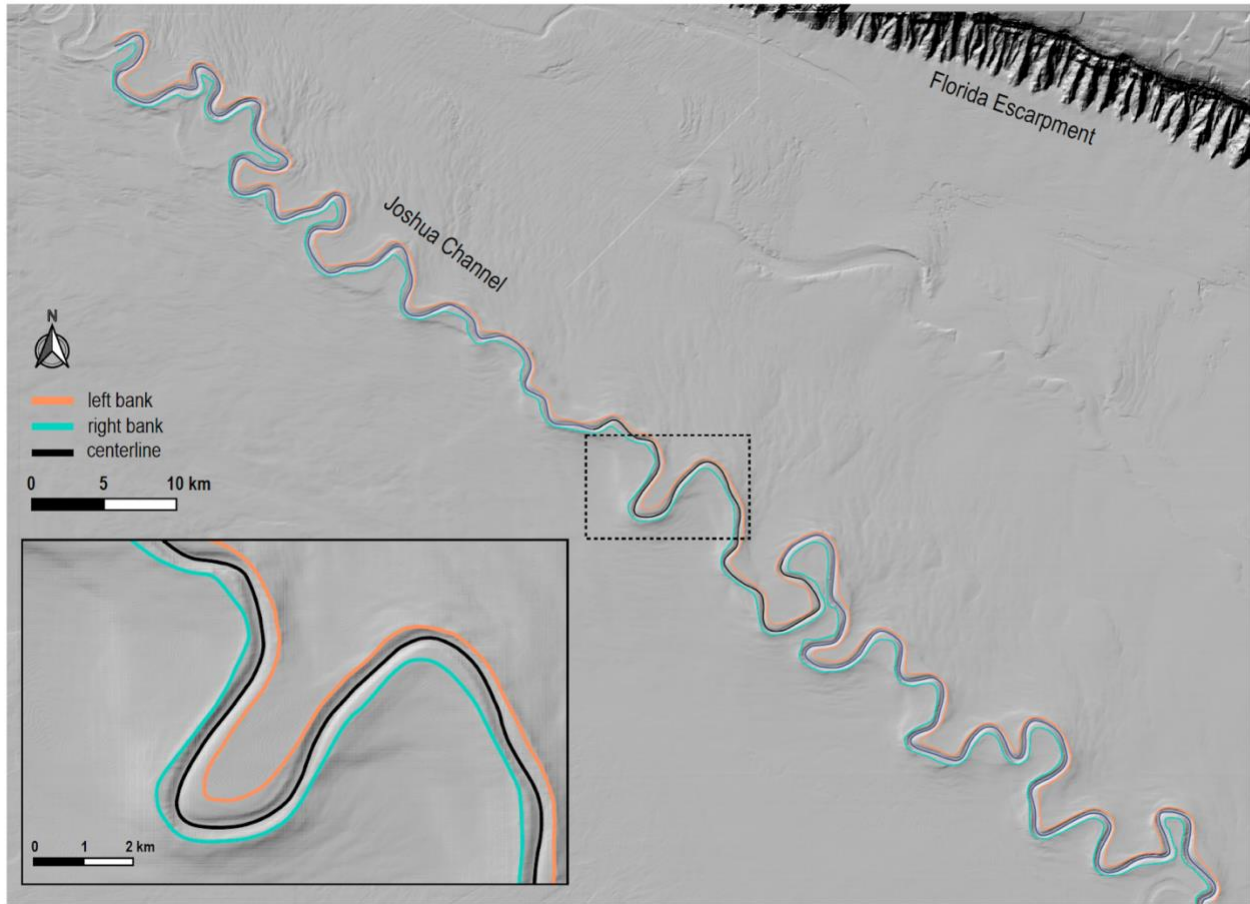


Figure 23. Left bank (orange), right bank (aqua), and centerline (black) interpreted along the seafloor from a high-resolution bathymetric map, with a close up of bends 26-27. The map made available by the BOEM (Kramer and Shedd, 2017).

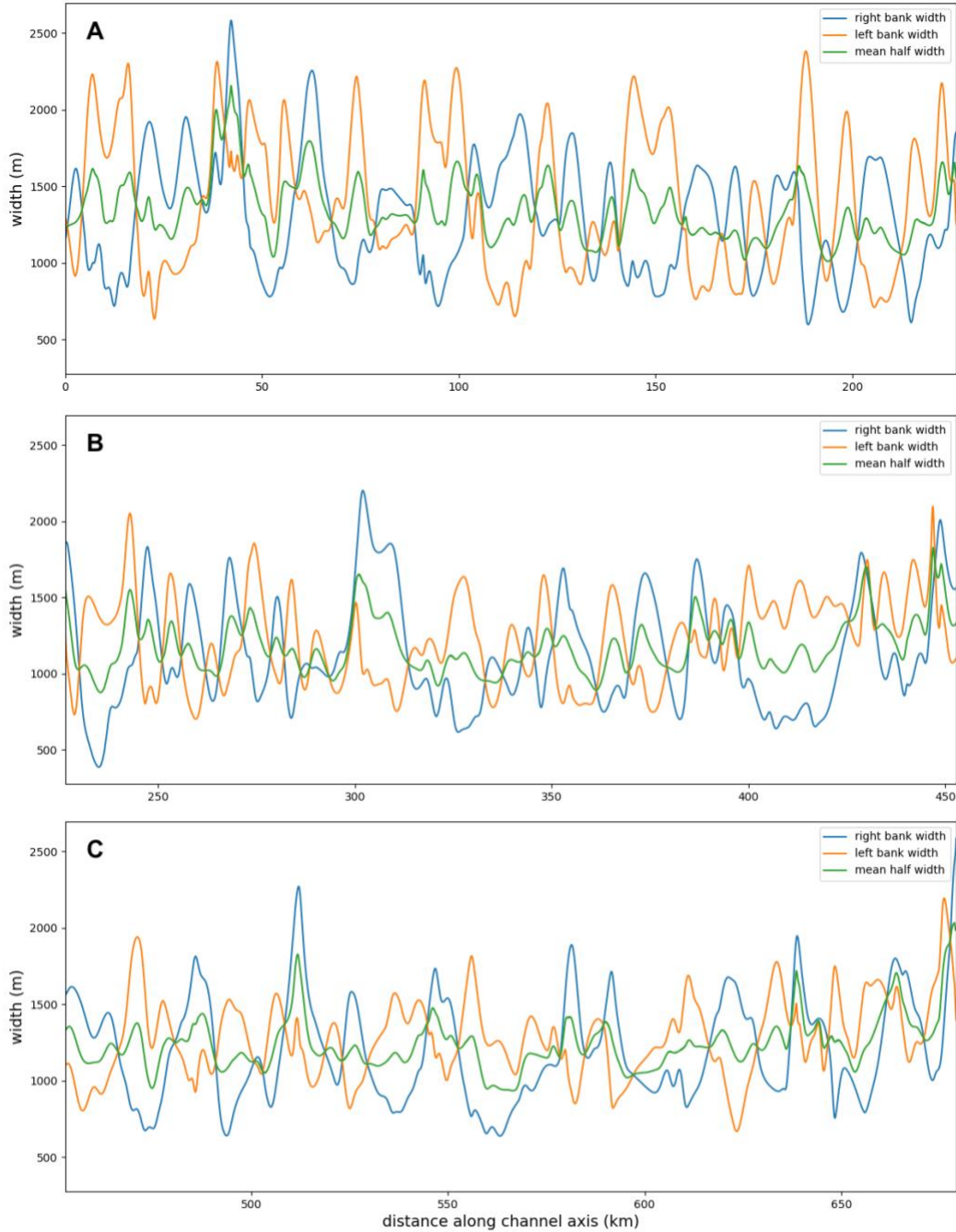


Figure 24. Right bank width, left bank width, and mean half-width plotted along the axis of Joshua Channel (with A along the first third of the channel, B along the second third, and C along the last third). Mean half-width indicates variation in width along the channel. Left and right bank widths indicate the fluctuation in widths along respective sides of the left and right banks, and vary inversely. Either the left or right bank widths may be used as a half-width. Point-bar-like features, the result of lateral migration, will appear as half-width maximums, while cutbanks will display as half-width minimums.

In addition to the levee crest bank boundaries, thalweg boundaries are also mapped in relation to the seafloor centerline (Fig. 25). Thalweg boundaries mark the edges of the relatively flat bottom of the channel (Fig. 25).

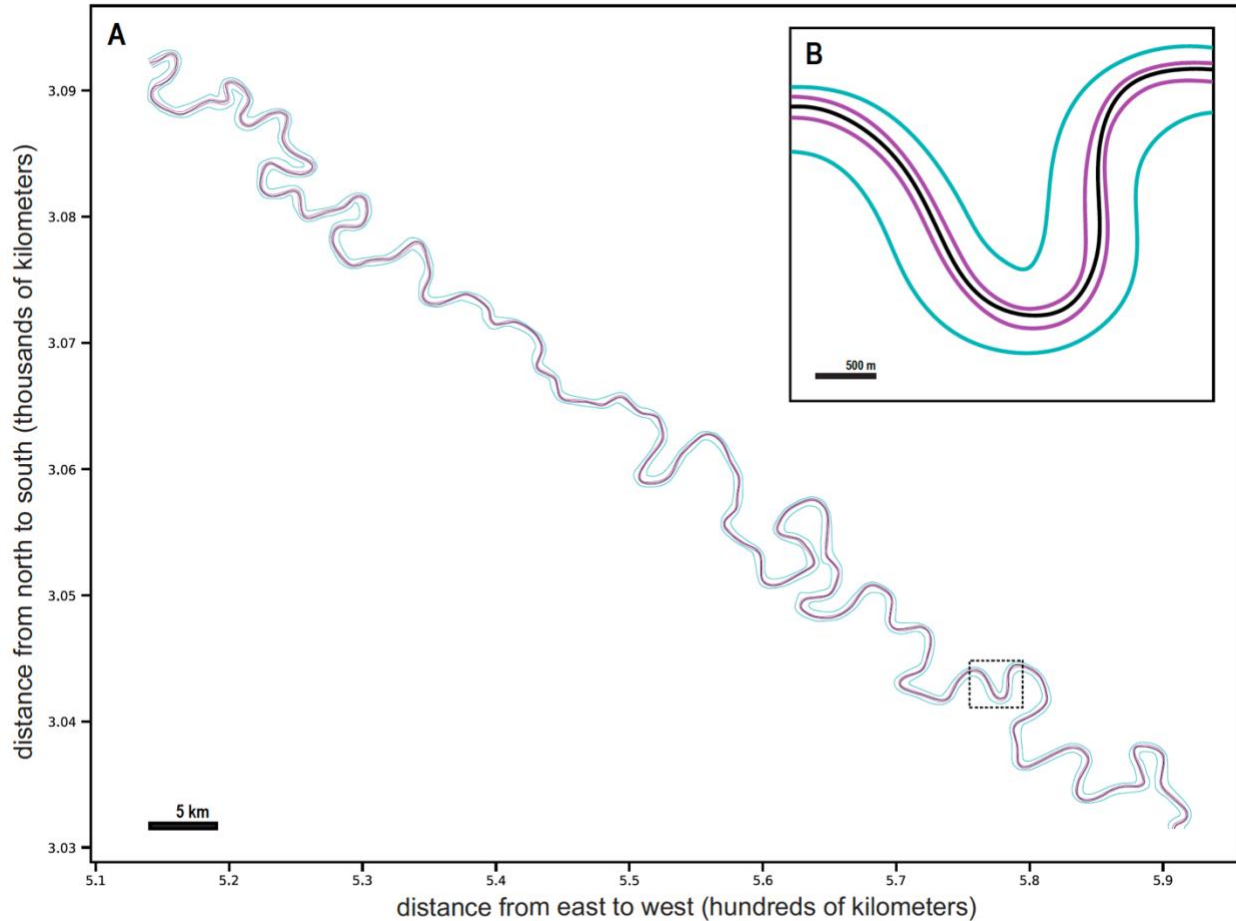


Figure 25. A: Map of levee crests (light green), thalweg edges (aqua), and centerline (black). B: Close-up of one bend outlined in a dashed box on Fig. 25a. The “levee crest” banks are equivalent to the “right bank” and “left bank” that are used to calculate left bank width and right bank width. Centerline and bank boundaries interpreted from the high-resolution bathymetric data. Contours were extracted using the same process described in the discussion of seismic data, and used in conjunction with the bathymetry map to interpret dominant thalweg positions and orientations from the positioning of topographic features such as high-flow bank boundaries and point-bar-like features.

The map of timestep 4 and its corresponding correlation plot are in Figures 26 and 27, displaying inflection points for curvature (teal) and points of zero migration (red), labeled by bend number.

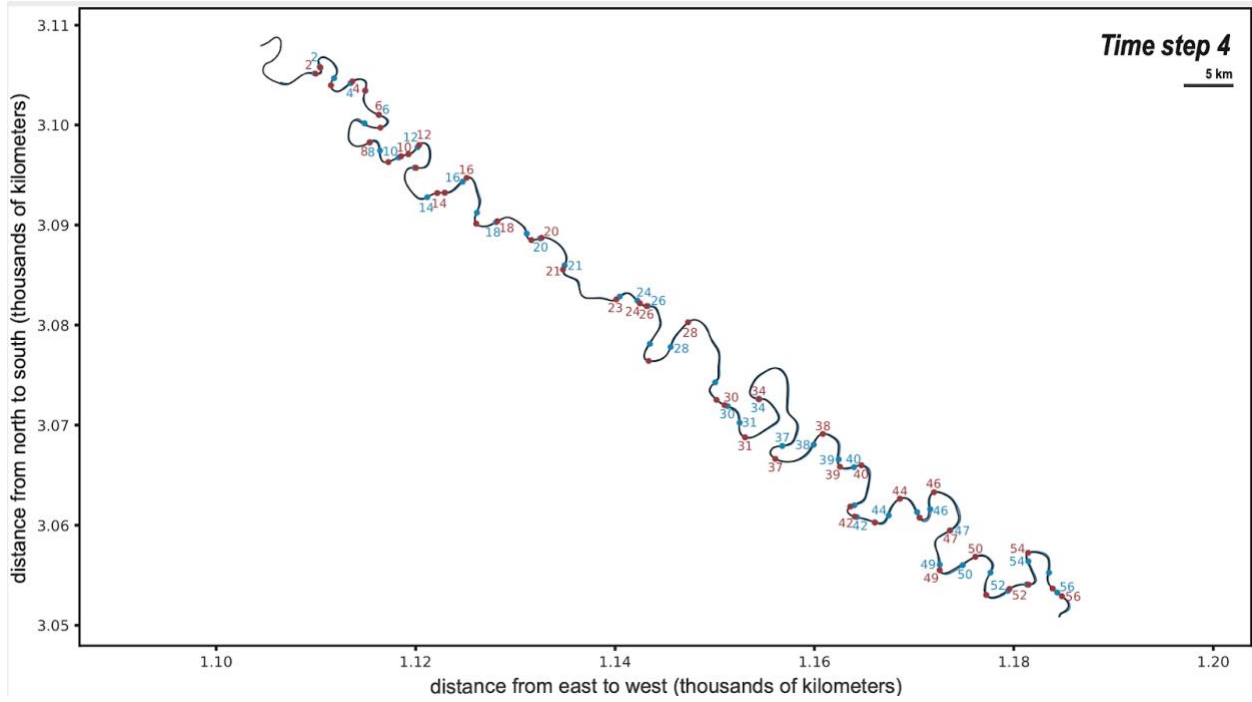


Figure 26. Map of inflection points and zero migration points labeled by bend (every other bend labeled) for time step 4, from Horizon 1 to the seafloor.

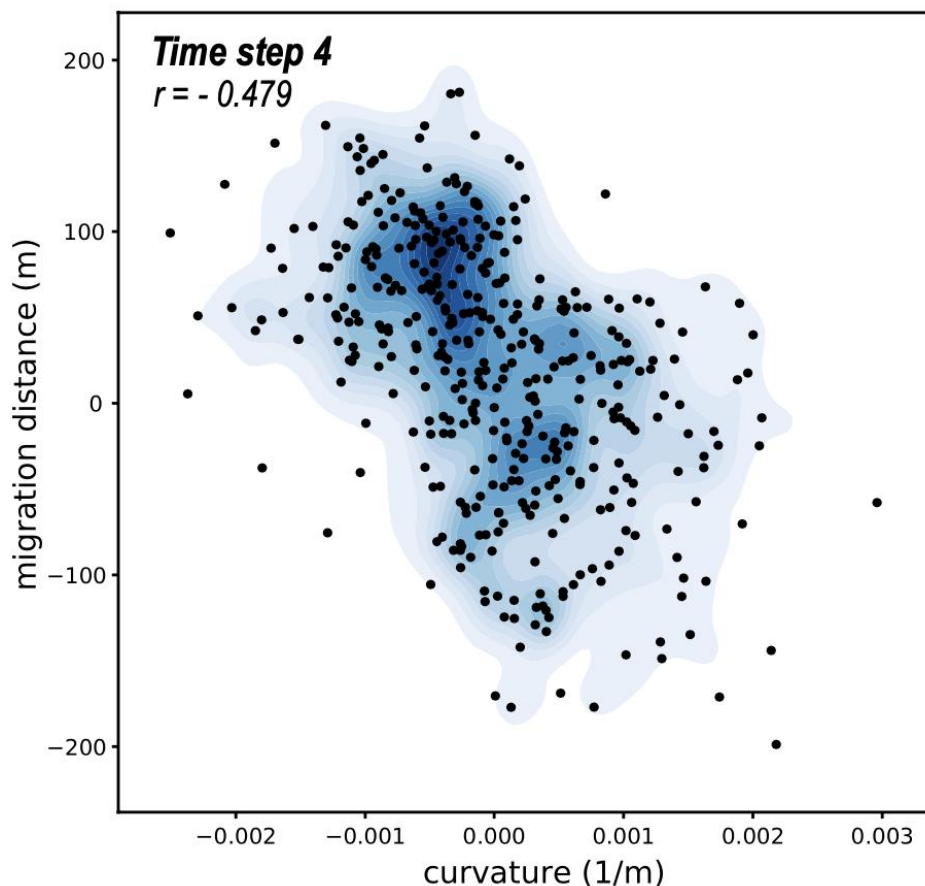


Figure 27. Correlation between migration distance and curvature between the seafloor centerline and Horizon 1 with a phase lag of 300 m between curvature and migration distance, $r = -0.479$.

These findings show that trends in channel curvature are similar to trends in half-width. The median lag computed using LZM and LZC points was 300 m, and the correlation between curvature and half-width was maximized at 250 m (Table 4). In other words, the variation of half-width is shifted downstream by approximately 250 m relative to the variation in centerline curvature.

The lag computed between curvature and half-width (250 m) is less than half that computed for migration distance and curvature (690 m), and is 1.4 times the thalweg width and 0.30 times the levee crest width. $R = 0.772$ when this lag was taken into account. This suggests that the linear relationship between half-width and curvature is significant, with half-width explaining about 60% of variance in curvature.

Chapter Five: Discussion

Although each time step experienced somewhat different changes in sinuosity, migration, and had slightly different relationships between curvature and migration distance, the overall pattern of change is similar across most time steps: an increasing sinuosity and a statistically significant linear correlation between curvature and migration distance, if the spatial lag between the two is taken into account. The relationship between curvature and migration improves compared to original estimates when low quality data are excluded. The relationship between curvature and half-width followed the trend expected, with half-width following curvature. However, the size of the half-width lag was smaller than the lag observed in centerlines interpreted from seismic: the half-width lagged behind curvature by a distance of less than half that of the 679 m lag measured in older channels.

Curvature and Migration

The inclusion of centerline segments interpreted from low quality data decreases the correlation coefficient r by up to 0.015, increases sinuosities of horizons 3 and 4 and decreases the average migration distance. The increase in sinuosity may be due to a tendency to exaggerate curvature, or may simply reflect that the segments of centerlines with incomplete information were located in the high sinuosity portion of the channel. The discrepancy between the full results and results derived from high-quality data is apparent when comparing Table 1 and Table 2. When such unreliable centerline segments are excluded, the linear relationship between curvature and migration, in most cases, strengthens. R only decreases in the case of data exclusion for time step 2 (by 0.011). This discrepancy suggests that centerlines based purely on interpretations of map view channel history are inadequate for a robust analysis of the curvature-migration relationship. While the automatic detection of channel thalwegs by amplitude patterns in seismic data may not be perfect, it is preferable for high-resolution analysis. The manual interpretation of centerlines through map view may encourage confirmation bias and diminish quality of data analysis. For this reason, this study will discuss time steps in its following sections based on results derived from the cropped channels, highlighted in Table 2.

Each timestep has variable migration distances and correlations between curvature and migration distance (Table 1). Between the smallest time steps (1 to 3), the median distance that each point along the channel migrated was highest in Time step 1 (126 m per point) and lowest in time step 2 (49.0 m per point). Sinuosity in these time steps increased the most in time step 1

(+ 0.14), the least in time step 2 (+ 0.05), and by a small amount (+ 0.07) in time step 3. Among the large time steps (A-C), sinuosity predictably increased more with increased migration distance and larger time intervals. The overall increase in sinuosity across the time series was + 0.39. In Tables 1 and 2, “Migration distance” refers to the median absolute value of movement from the old centerline to the new centerline at any particular point on the old centerline. “Aggradation height” is a rough estimate based on contour plots and refers to the change in depth between horizons during each timestep. “r” refers to the correlation coefficient between curvature and migration distance when a lag (listed to the right) is considered.

The amount of migration and aggradation varies for each timestep. Over the course of the time interval studied, the M/A ratio increases. This observation runs counter to the general trend observed in Joshua Channel of incision dominant lateral migration succeeded by dominant aggradation. However, this short trend appears to be noise within the overall trend of increasing aggradation relative to migration, which is evidenced by the “J” stacking patterns observed in seismic cross sections (Fig. 9). Despite the unexpected trend in M/A ratios, the channels depicted in these timesteps are still highly aggradational. Sylvester et al. (2011) plot the aggradation and lateral migration of two time intervals in the Benin Major channel-levee system. Compared to those results, aggradation about twice as dominant in the timesteps of Joshua Channel.

<i>Time step</i>	<i>Horizons</i>	<i>S, old channel</i>	<i>S, new channel</i>	ΔS	<i>Migration distance (m)</i>	<i>Aggradation height (m)</i>	<i>M/A</i>	<i>r</i>	<i>Lag (m)</i>
1	4 to 3	2.17	2.28	+ 0.11	111	52	2.13	0.634	675
2	3 to 2	2.00	2.06	+ 0.06	48.9	16	3.06	0.595	650
3	2 to 1	2.10	2.17	+ 0.07	56.5	10	5.65	0.758	675
A	4 to 1	2.17	2.41	+ 0.24	199	77	2.58	0.782	750
B	4 to 2	2.17	2.35	+ 0.18	143	62	2.30	0.755	675
C	3 to 1	2.00	2.12	+ 0.12	103	36	2.78	0.748	700

Table 1. Sinuosity changes, aggradation and migration estimates, and the migration-curvature relationship for each time step.¹ Horizons are numbered by age, with Horizon 4 being the oldest and Horizon 1 being the youngest. Note that each time step covers different reaches of the channel due to limited data. For this reason, sinuosity values should not be considered as sinuosities of the whole visible channel length, except for in time step 3.

¹ Includes all data, with and without contour information: for updated results when poor data (without contour information) are excluded, see Table 2.

<i>Time step</i>	<i>Horizon s</i>	<i>S, old channel</i>	<i>S, new channel</i>	ΔS	<i>Migration distance (m)</i>	<i>Aggradation height (m)</i>	<i>M/A</i>	<i>r</i>	<i>Lag (m)</i>
1	4 to 3	2.13	2.27	+ 0.14	126	52	2.13	0.655	700
2	3 to 2	1.93	1.98	+ 0.05	49.0	16	3.06	0.584	625
3	2 to 1	2.10	2.17	+ 0.07	56.5	10	5.65	0.758	675
A	4 to 1	2.04	2.43	+ 0.39	197	77	2.58	0.789	725
B	4 to 2	2.04	2.37	+ 0.33	156	62	2.30	0.780	675
C	3 to 1	1.93	2.04	+ 0.11	98	36	2.78	0.752	675

Table 2. Sinuosity changes and migration distance of each time step, when low quality data (lacking seismic horizon information) are excluded.

The linear correlation coefficient between migration distance and curvature ranges from 0.584 to 0.789. r is highest for the cumulative timestep. This may be because the magnitude of the changes in curvature and migration distance are higher in proportion to their margin of error, compared to those of shorter time steps. However, r seems not only tied to the length of the timestep, but to the timing of seismic horizons, specifically Horizon 3. $r = 0.584$ in time step 2 and 0.640 in time step 1, representing the weakest linear relationships of the data set. Both timesteps 1 and 2 include Horizon 3. When comparing the correlation between Horizon 4 and Horizon 2 in timestep B, however, r increases to 0.780. Similarly, when Horizon 3 is matched to Horizon 1, r increases to 0.752. Although increased correlations in time steps B and C are likely due to increased magnitude of timesteps, they may also suggest that Horizon 3 represents a temporary departure from baseline autogenic changes, disrupting the order of the channel at the close of time step 1 and the beginning of time step 2. It may also be that time steps 1 and 2 were too short to detect a good signal and that time step 3 has a high r value because of higher data quality at shallow depth.

	Levee Crest	Thalweg
<i>Width (m)</i>	751	174
<i>Lag/Width Ratio Range</i>	0.8 – 1.0	3.6 – 4.2

Table 3. Lag:width for levee crest and thalweg width measurements. Using levee crest width in the L/W ratio results in different lag:width ratios than those found for rivers of the Amazon Basin (Sylvester et al., 2019). However, using thalweg width gives a ratio that is comparable to that of rivers of the Amazon Basin. Median widths are used in row two, with standard deviations of $\sigma = 43.6$ m (thalweg width), and $\sigma = 120$ m (levee crest width). Lags of 625 and 725 m are used for the ranges of lag/width ratios, which represent the range in lags in Table 2.

An important question is whether the lag between curvature and migration in submarine channels is similar to the lag observed in fluvial channels. There are three different width measurements for Joshua Channel described here. “Levee crest width” is the most common width measured in the study of submarine channels and is thought to be comparable to bankfull width in fluvial channels. Point-bar-like features, cutbanks, and other elements reminiscent of rivers may be observed in submarine channel systems, and levee crests are fairly easy to distinguish and trace, even in areas where data are limited. However, as previously discussed, the comparison of bankfull width to thalweg width may be more appropriate for interpretations of channel planforms and patterns (Pirmez and Imran, 2003). Defining width as that between levee crests leads to a lag/width ratio much lower (approximately 1) than that of the rivers of the Amazon Basin (2.1-4.7). The thalweg width, however, suggests that the lag/width ratio of the Joshua Channel is well in range of that of rivers of the Amazon Basin, at 3.6 to 4.2. This result is not surprising given that Pirmez and Imran find comparable scaling relationships to fluvial data when using thalweg width (2003), and supports the use of thalweg width as a more appropriate “bankfull width” than levee crest width.

The lag-to-width ratio in Joshua Channel (3.6-4.2) is similar to the L/W of rivers of the Amazon Basin (2.1-4.7). The similarity of these ratios across multiple scales and such different systems suggest that the magnitude and the direction of the lag between curvature and migration is a fundamental property of meandering channels. The lag parameter seems to scale with width, as larger channels tend to have larger lags. In rivers, and in simple models of meandering, it also depends on the friction factor (C_f) that characterizes the amount of friction at the base of the

flow (Sylvester et al., 2019). Higher values of C_f tend to decrease the spatial lag between curvature and migration. For rivers of the Amazon Basin, lags in the range of those of the Joshua Channel reflected portions of the river with friction factors between 0.0029 and 0.0061, with a median of approximately 0.0046.

Absolute age data would aid this analysis. As this is an overall aggradational system, depth can be used as an approximate indicator of age. Time step 1 experienced the most aggradation (approximately 52 m). However, a careful analysis should take into account the effects of decompaction and the uncertainty of sediment composition at depth. A future research project might explore a more detailed analysis of aggradation and migration rates over the life of Joshua Channel, and compare aggradation and age to other metrics explored here.

Curvature and Half-width

The relationship between channel curvature and half-width is similar to the one between channel curvature and migration, except it has a significantly smaller lag (a 250 m versus a 679 m lag) (Fig. 21, 22A; Table 4). In contrast, the younger centerline of time step 4 seems to migrate in the opposite direction from what is expected from curvature. The lag in time step 4 (as in the half-width analysis) is also smaller than that of other timesteps (a 250 m versus an approximately 700 m lag). Curiously, the difference between the lags of half-width and timestep 4 both deviate from the expected lag of 700 m by a similar amount (450 to 400 m).

<i>Relationship</i>	ΔS	<i>Migration distance (m)</i>	<i>Aggradation height (m)</i>	<i>M/A</i>	<i>R</i>	<i>Lag (m)</i>
Curvature & migration, timestep 4	- 0.05	58	91	0.63	- 0.479	300
Curvature & half-width	N/A	N/A	N/A	N/A	0.772	250

Table 4. “ ΔS ” represents the change in sinuosity of Joshua Channel from Horizon 1 to the seafloor. “Migration distance” is the median migration distance from the old centerline to the new centerline. “Aggradation height” is a rough estimate based on contour plots and refers to the change in depth between horizons during each timestep. Historical aggradation amounts (particularly in muddy units and at great depths) were likely significantly higher, as this measurement does not account for compaction. “M/A” summarizes the relationship between migration and aggradation in a dimensionless ratio of migration distance to aggradation height. “R” refers to the correlation between curvature and migration distance when a lag (listed to the right) is considered.

In all timesteps, the migration distance was compared to the curvature of the older centerline. However, the half-width analysis used the curvature of the seafloor centerline (the younger centerline). The spatial curvature variation in younger and older centerlines may not be the same. Figure 28 depicts curvature and half-width on bend 8. In most cases (assuming the majority of bends translate downstream), the maximum curvature points of younger centerlines are likely to be located downstream from the equivalent points of older centerlines. This spatial lag between curvatures of older and younger channels may result in a smaller lag between half-width and curvature when the younger centerline is used.

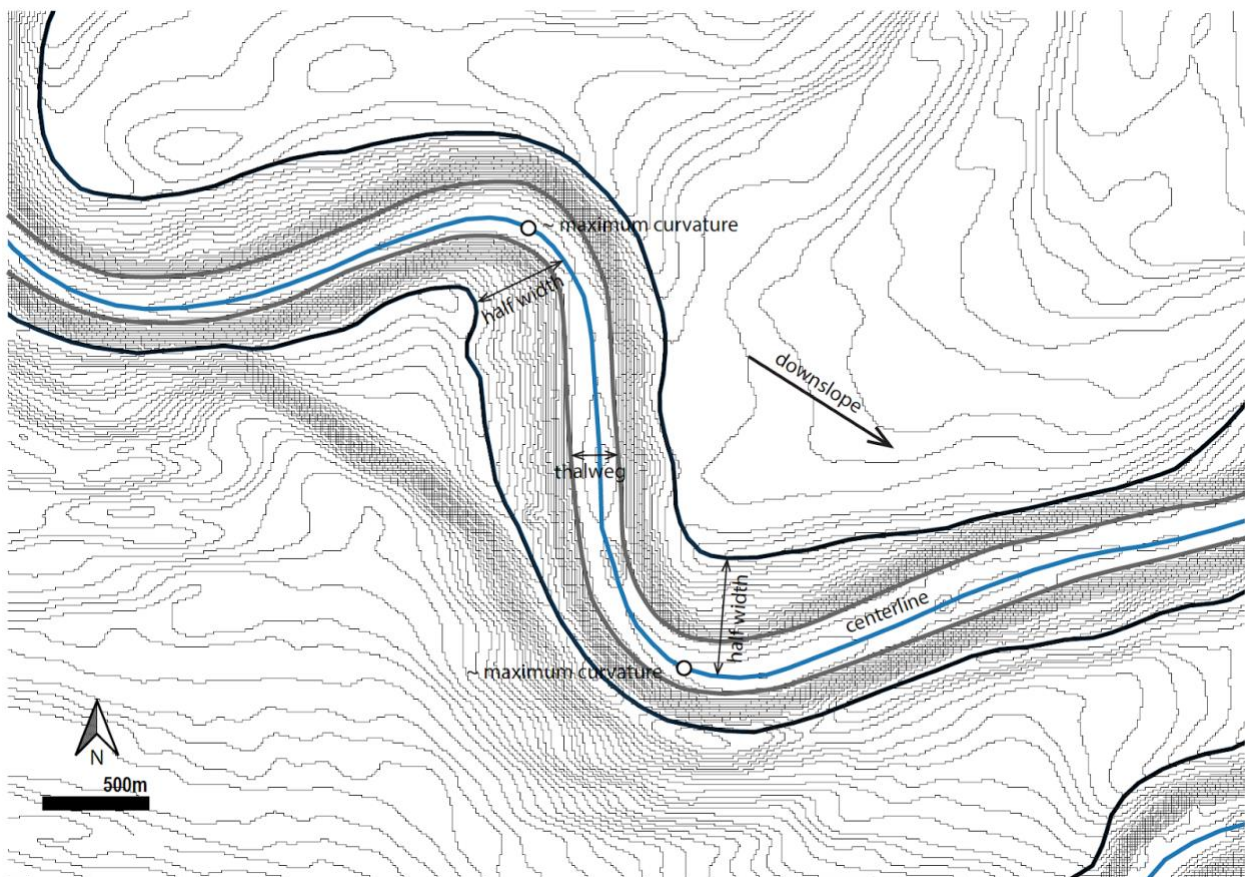


Figure 28. Centerline of the seafloor (blue line) on bend 8 in timestep 8, with thalweg edges (grey) and levee crests (black), to illustrate how the half-width measurements capture the asymmetry of the channel. The white points represent approximate locations of zero curvature for the seafloor.

Despite the smaller lag, half-width likely provides a useful proxy for migration distance, and correlates well ($r= 0.772$) with curvature.

The timestep between Horizon 1 and the seafloor suggests a negative correlation between curvature and migration distance. However, this relationship is weak ($r = -0.479$) compared to the mean of the other timesteps ($r = 0.720$). This result may also arise from special circumstances pertaining to channel abandonment that may distort channel centerlines, which is described below.

On most bends, the seafloor centerline seems to have migrated inward towards point bars and tightened the bends. This behavior distinguishes this time step from the others. In other time steps, bends tend to swing or sweep more as the channel evolves. It may be the case that a true tightening of bends actually occurs in this last timestep. However, it may also be the case that the overlying approximately 30 m thick deposit of mud observed by Posamentier (2003) is a channel-filling debris flow that does not result in typical migratory channel behavior. These final deposits may, potentially, deposit sediment preferentially along the channel bottom, which may distort the perceived position of the thalweg of the last active channel.

An example of how centerline distortion may occur is depicted in Figure 29, on bend #12 of Joshua Channel. Figure 29 shows the bend on a bathymetric seafloor map with the interpreted centerline (teal) and terrain profile section taken roughly perpendicular to the thalweg. The centerline reflects the interpreted thalweg of the channel (Fig. 29a), following topographic lows on the channel bottom. Figure 29b depicts the terrain profile from point bar to cutbank, with an annotated dashed line representing a realistic profile of a channel bottom that may have been present before a channel filling event. In this case, a channel filling event would have deposited approximately 3 m on the bottom of the present channel without preserving detail of the preceding thalweg imprint. The centerline of the deeper channel bottom (dashed) would have been approximately 16 m closer to the cutbank than the centerline measured (solid) (Fig. 29b).

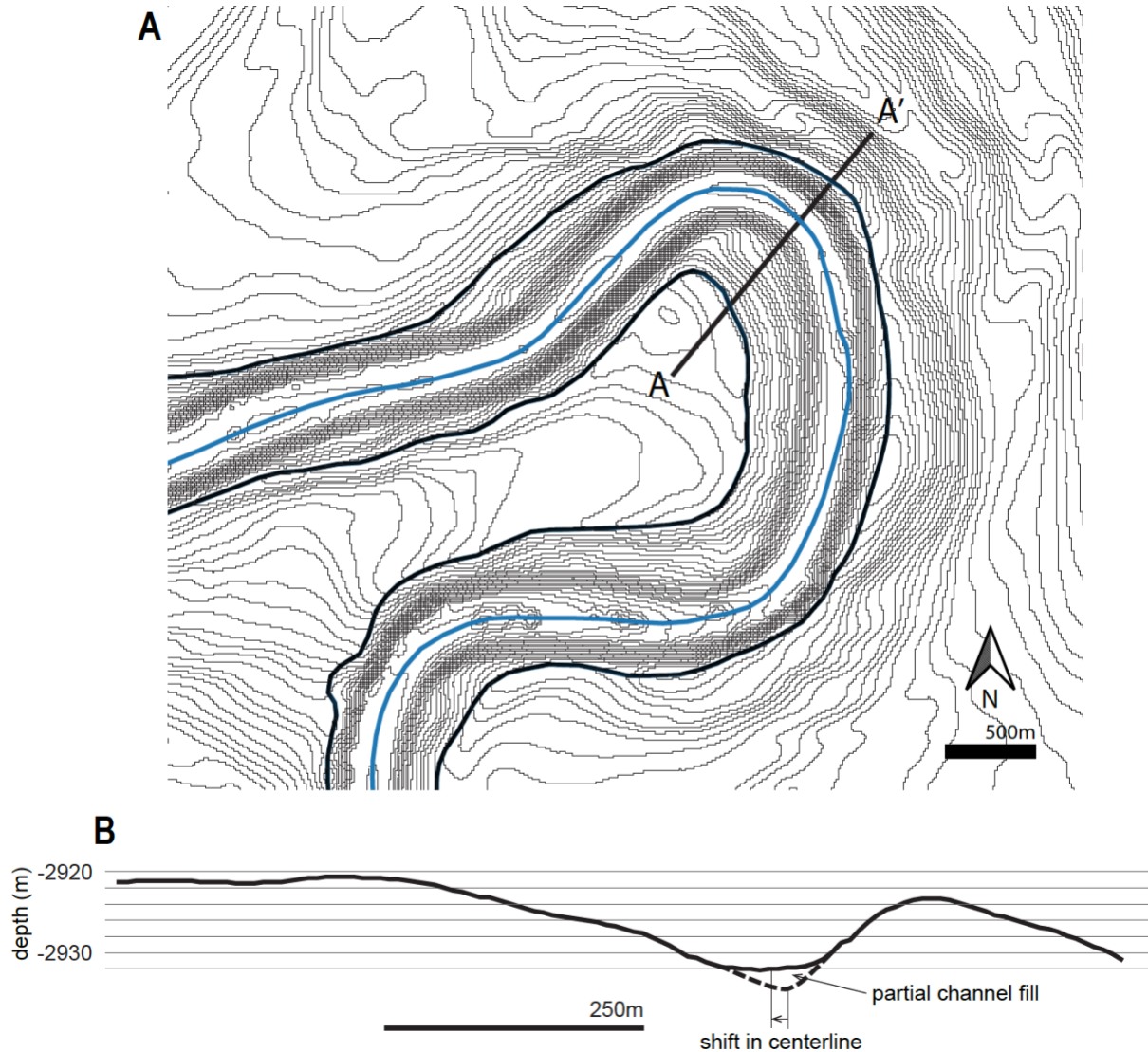


Figure 29. A: Bend 12 of Joshua Channel on a contoured bathymetric seafloor map with the interpreted centerline (teal) and terrain profile section (segment AA'') taken roughly perpendicular to the thalweg. The centerline reflects the interpreted thalweg of the channel, following topographic lows on the channel bottom. B: Terrain profile depicts elevation along the channel from point bar (left) to cutbank (right). The terrain profile is vertically exaggerated. A simple profile of an active channel is annotated beneath the thalweg (dashed). In this segment, following the centerline of the older (dashed) channel bottom would have resulted in that point of the centerline shifting about 16 m towards the cutbank.

Considering that the median migration distance of Horizon 1 to the seafloor centerline is about 58 m, a 16 m outward shift of the centerline would increase the calculated migration distance by 28%. This effect may weaken with increasing fill in submarine channel-levees, as the difference between point bar and cutbank gradients may diminish with increasing relief.

That a channel fill may shift this centerline inward is unsurprising given that a) the first centerline was drawn to reflect an interpreted thalweg (rather than the central point between banks), and that b) point bar gradients are less steep than cutbank gradients, so that any flattening of the channel bottom would naturally shift the point between slopes towards the point bar. Inward movement of channel thalwegs where the differential between cutbank and point bar gradients is high may enhance increases in bend curvature after channels are filled with low energy flows. That channel filling processes played a large role seems more likely given the results of time step 4, whose correlation plot hardly resembles those of other time steps.

The mechanics of debris flows and other submarine sediment-laden flows are not the focus of this thesis, and Figure 29 may not capture the true effects of channel filling processes on channel profiles. It may simply be the case that lower energy flows were not directed at channel cutbanks as powerfully and that the channel tightened. However, the geometry of channel axes may play an important role in centerline placement when flows transition from erosion- to deposition-dominated or change the proportion of sediment deposited at channel bottom relative to banks. Additionally, these considerations may inform the decision of defining a centerline by either an interpreted thalweg (best preserved in seismic) or points equidistant from both banks (best identified in seafloor bathymetry).

Chapter Six:
Channel Migration, Reservoir Architecture, and Qualitative Impact on Financial Value

Overview

The discussion of channel migration is important to understand reservoir communication, recovery efficiency and production rate, all of which affect the net present value (NPV) of deepwater upstream projects. The net present value of a project to investors is estimated from the combined value of cash flows arising from the project while considering the time value of money². To project NPV using discounted cash flow (DCF) analysis, estimated cash flows for each year are calculated as:

$$FCF_t = EBIT_t \times (1 - T) + D - \Delta ONWC_t - CAPEX_t \quad (5)^3.$$

The cash flows are then discounted by dividing each year's cash flows by $(1 + r)^I$, in which r is the discount rate and I is the cash flow period, and subtracting the initial investment from the sum of discounted cash flows (Gallo, 2014). Absent discussion of taxes or other forms of government take (e.g. royalty payments), the NPV of oil and gas projects highly depends upon the 1) estimated ultimate recovery of reserves (EUR), 2) the production profile and 3) the cost of development (CAPEX and OPEX).

In channelized reservoirs, geological interpretations of channel migration impact both the production profile and development costs. With respect to development costs, reservoir architecture impacts the location and number of wells needed to maximize the recovery factor and achieve high flow rates. Darcy's Law describes flow rate (Q) as:

$$Q = \Delta p k A / \mu L \quad (6),$$

with permeability (k), pressure drop (Δp), and cross-sectional area (A) of a conduit increasing flow rate and dynamic viscosity (μ) and length of a conduit (L) decreasing flow rate. Reservoir architecture controls the cross-sectional areas and lengths of reservoir elements as well as the distribution of permeability throughout the reservoir.

² This discussion will specifically refer to the value of project to both debt and equity investors, and will thus discuss unlevered cash flows.

³ The calculation of free cash flows in a given year (year t). The variables are Earnings before Interest and Taxes (EBIT), the Tax Rate (T), Depreciation Expense (D), Change in Operating Net Working Capital ($\Delta ONWC$), and Capital Expenditures (CAPEX). The earnings in an upstream oil and gas project for a given year will relate to production and oil price; the operating net working capital, to the cash inflows and outflows necessary to maintain operations; the depreciation and capital expenditures, to the cost of wells and plants, property, and equipment.

Following the logic of Darcy's Law and with all else equal, high permeability, high cross-sectional area portions of a turbidite channel reservoirs should be targets for production well placement. Injector wells should be placed in relation to production wells in the manner that maximizes the amount of oil swept. Wells with high flow rates are NPV-advantaged, for the production in year 20 will be worth much more than the equivalent amount in year 30. Optimizing production and injector well placement to increase initial production rates and limit well count should significantly impact project NPV. The complexity of geological controls on permeability distributions, cross sectional areas, and lengths of flow conduits make good reservoir models vital. This brief analysis in no way, shape or form is a substitute for the flow analysis that would come from a reservoir simulation.

The following sections will review key considerations for reservoir architecture, discuss the architecture of Joshua Channel and its comparable channel systems, and lastly discuss hypothetical connectivity in a cross-section of Joshua Channel in order to articulate the effects reservoir architecture has on development costs and NPV.

Reservoir Architecture and Impact on Development

Reservoir compartmentalization of any kind usually has very deleterious effects on the economics of deepwater fields. There are several reasons for this. Drilling costs command a disproportionately large part of overall field development CAPEX. This issue is exacerbated by the very high costs of individual wells in deepwater. It is further exacerbated by the fact that many deepwater fields are managed with 100% voidage replacement almost from the beginning of production. That means that every barrel of oil produced is replaced by an equal volume of injected water or gas. Therefore, each additional reservoir compartment requires not just one additional well but two (producer and injector pair).

This section will review aspects of reservoir architecture affecting development, drawing from many examples of fluvial channel reservoirs. However, the similarities and differences between fluvial and deepwater channels must be contextualized before using fluvial systems as analogues.

Kolla et al., (2007) discuss the main differences between fluvial and deepwater systems. They state that one of the main differences between the two systems is that deepwater channels aggrade to a larger extent and migrate downstream to a lesser extent than fluvial systems do (Kolla et al., 2007). However, it is worthwhile to note that in several deepwater systems laterally

migrated channels occur even in more aggradational upper parts of the channel complexes (Abreu et al., 2003; Samuel et al., 2003). While fluvial channels commonly exhibit point bar scrolls that are laterally continuous and migrate downstream, in deepwater channels, migrations may be lateral, continuous, or discrete, laterally to vertically aggrading and with or without a downstream component (Kolla et al., 2007). Widths and depths of submarine channels also tend to decrease downstream, and submarine channels favor vertical aggradation regardless of grain size, whereas aggradation in fluvial channels tends to occur along with increased grain size (Kolla et al., 2007). These differences stem from the properties of sediment gravity flows (in deepwater) and fluid flows (in rivers) (e.g. Imran et al., 1999; Shanmugam, 2000; Kolla et al., 2001). While in rivers both traction and suspended modes of sediment transport are important, in turbidity currents (sediment gravity flows) suspended sediment transport is more important (Kolla et al., 2007). Additionally, density differences between river currents and air exceed those between sediment gravity flows and ambient fluid (leaving less entrainment of ambient fluid into sediment gravity flows), and Coriolis (particularly at high latitudes) and centrifugal forces have a strong effect on submarine flows (Kolla et al., 2007). Despite these differences, many similarities also exist. Morphological characteristics of deepwater channels are similar to fluvial ones, particularly in terms of sinuosities, relationships between meander wavelengths, delayed inflection symmetries, and avulsions and cutoffs (Kolla et al., 2007, Flood and Damuth, 1987; Amir, 1992; Clark et al., 1992; Pirmez and Flood, 1995; Babonneau et al., 2002). Evidence of relatively continuous lateral migrations in seismic data has been observed in many regions of the world, such as offshore Nigeria, Angola, Indonesia, India, and the Gulf of Mexico (Kolla et al., 2007; Bastia, 2004; Deptuck et al., 2003; Abreu et al., 2003). This study underscores the similarities in these morphological characteristics, which are important to the lateral migration aspect of channel stacking discussed here.

Three aspects of reservoir architecture are particularly important to modeling the prospectivity of deepwater submarine channel plays: channel stacking patterns and their internal permeability differences, mudstone or shale drapes, and cutoffs. First, channel stacking patterns play a key role in reservoir connectivity and well performance. Identifying stacking patterns within channels is vital to designing the location and orientation of wells (Mayall and O'Byrne, 2002). The lateral versus vertical pattern of channel element stacking affects the reservoir recovery factor. Vertical connectivity in particular is a critical factor for production performance,

because it tends to align the most coarse-grained channel elements (Jackson et al., 2019). Jackson et al. (2019) demonstrate that connectivity is reduced in cases of high lateral channel element offsets. The lateral vs. vertical stacking of thick-to-thin reservoir lithologies is determined by the degree of lateral migration vs. vertical aggradation, with vertical stacking promoting vertical reservoir connectivity (Kolla et al., 2001). Interestingly, while channel stacking patterns will differ between channel systems, general trends are also observed. For example, long-lived channel complexes commonly evolve from laterally offset to vertically aligned channel elements (e.g., Deptuck et al., 2003; Hodgson et al., 2011; Covault et al., 2016; Jobe et al., 2016). The trend described may increase reservoir connectivity compared to a scenario of random channel placement. For this reason, the assumption of randomness likely underestimates the connectivity of reservoirs made up from long-lived channel systems.

Permeability differences within the channel stack provide challenges for well placement. Curkan et al. (2019) demonstrate that well performance may depend on the well's positioning relative to the migratory sequence of the channel in a reservoir of stacked channel elements. Curkan et al. (2019) illustrate this concept through their study of horizontal steam assisted gravity drainage (SAGD) well performance in a fluvial system. In their study area (the McMurray Formation) production rates are typically higher where steam chamber growth is uninhibited, where stacked meander deposits display sand-on-sand contact. For example, a well intersecting two overlapping point bar deposits would perform better than a well intersecting a sandstone point bar deposit topped with a mudstone counter point bar deposit (Curkan et al., 2019). Hagstrom et al. (2019) describe how channel activity controls sand and mud distribution at the bend scale. For example, accretion packages in a point bar deposit may exhibit different depositional architectures depending on the mode of migration that produced them (Hagstrom et al., 2019). While laterally migrating bends may produce accretion packages that are wide at their apex, bends translating downstream may produce alternating wide-at-apex and downstream-wedge style packages, and bends engaged in both behaviors may toggle between the two depositional styles (Hagstrom et al., 2019). Migration modes and their associated accretionary packages translate into different resulting percentages of net sandstone in the point bar deposits, with the downstream wedge packages producing higher percentages of net sandstone than wide-at-apex packages in a study of 3D seismic and wellbore data from the Lower Cretaceous McMurray Formation in Alberta, Canada (Hagstrom et al., 2019). Within the lateral accretionary

packers, sand content even varied from upstream to downstream, with sandstone content increasing downstream from bar apex to bar tail in an atypical trend potentially signifying the initiation of a new depositional lobe (Hagstrom et al., 2019). Permeability along the channel axis also affects the prospectivity of a channel stack. While point bars may be compartmentalized by mud plugs, they may also be connected via a “string of beads” architecture (Donselaar and Overeem, 2008). In a database of 64 modern, ancient outcropping and subsurface fluvial depositional systems, a string-of-beads architecture appeared prevalent, with string-of-beads architecture dominating over that of full point bar compartmentalization in 87% of studied bars; complete compartmentalization occurred in 20% of studied bars (Colombera et al., 2017). Oil may also linger in upper portions of point bar deposits due to their geometry, leaving behind “attic oil” that escapes recovery, but this effect may lessen if the upper portions of point bar deposits have a lower NTG (Colombera et al., 2017).

Secondly, mudstone drapes pose large uncertainties to reservoir production forecasts because they are generally undetectable in seismic data and may act as strong baffles or barriers to flow. Alpak et al. (2011) rate the significance of geologic parameters to oil recovery and find that shale drape coverage consistently emerges as an important factor for displacement-type recovery mechanisms. Alpak et al. (2013) characterize three types of mudstone “channel base drapes”: 1) abandonment drapes (hemipelagic muds and fine grains that spill into the channel from another source), 2) convergent margin drapes (resulting from increased erosion of mud and deposition of coarse material in the channel thalweg and remnant mud or silt in the margins), and 3) bypass drapes (tails of turbidity currents which are more likely preserved at high gradients) (Fig. 30). While abandonment drapes are relatively rare, convergent margin and bypass drapes are more common and may occur together (Alpak et al., 2013). When Prather et al. (2000) quantify the effects of channel-base drapes, find that the recovery factor significantly declines once the drape coverage exceeds even approximately 10% of the channel base (Fig. 30). However, this model analyzes connectivity in two dimensions and therefore understates actual connectivity in a real, three-dimensional reservoir with dynamic channel deposits.

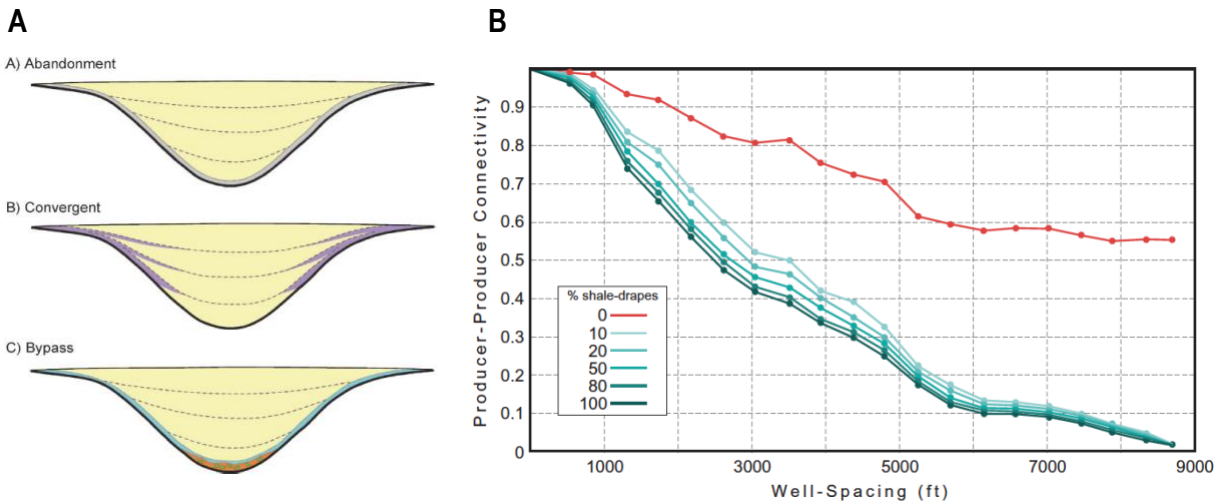


Figure 30. A: Diagram of possible types of channel-base drapes (Alpak et al., 2013). B: Producer-producer plot for the Brushy Bench (West Texas), with producer-producer connectivity a measure of the geometric connectivity within a sandstone. An average connectivity is calculated for each well location across at various well spacings (Prather et al., 2000).

Lastly, cutoffs may introduce stratigraphic heterogeneity that increase model uncertainty and produce abandoned channel deposits that impede oil recovery. Cutoffs tend to occur early on in the evolution of a submarine channel system and result in complex stratigraphy. Sylvester and Covault (2016) find intrinsic features of submarine channel cutoffs that introduce significant morphological variability, erosion, and stratigraphic complexity without external forcing. Examining data from offshore Angola, they find that locally steep gradients resulting from shortened flow paths initiate knickpoints that produce terraces and remnant deposits as the channel incises through the retreating knickpoints onto its new path (Sylvester and Covault, 2016). The complex stratigraphy that may result from cutoffs creates higher expectations of heterogeneity in reservoir models and in recovery estimates. In their most simple form, cutoffs may leave low-permeability mud-rich deposits in abandoned channels that reduce sweep efficiency. Colombera et al. (2017) show that if an injection well sits across from a production well within a compound bend that has an abandoned, mud-filled channel in its center, then the point bar volume bounded by the abandoned channel may remain unswept (Fig. 31). However, channel fills may be underlain by erosive channel contacts or filled with coarse material (in the case of a high-flow cutoff event), in which case more efficient sweep may take place. While cutoffs may produce challenging heterogeneities and potential barriers to flow, statistical analysis of large data sets may reduce uncertainty over these impacts on oil recovery. Colombera

et al. (2017) utilize quantitative characterization of 1259 architectural elements from modern and ancient rivers from 64 datasets to predict the volume of the largest unpenetrated compartment based on bar thickness and well spacing. Large scale data analysis may aid the understanding of impactful small-scale heterogeneities.

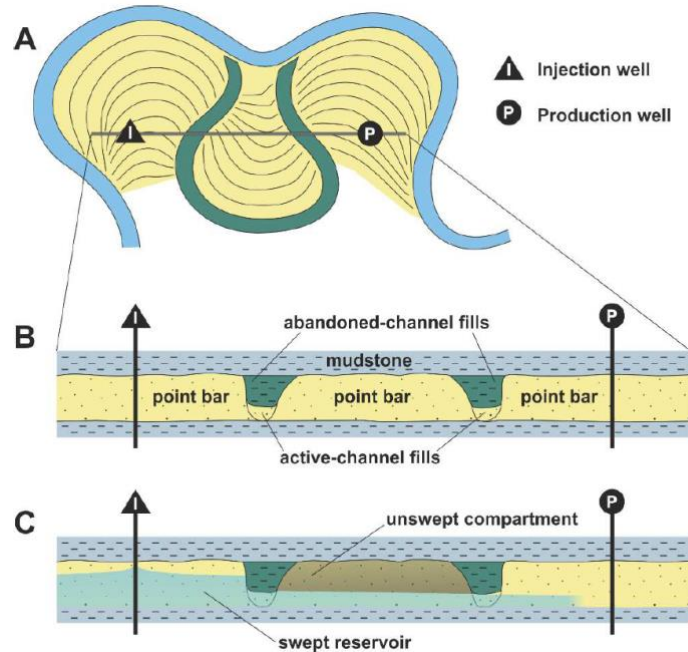


Figure 31. A: Planform view of an idealized meander belt consisting of sand-rich point bars (yellow) and mud-prone abandoned-channel-fill deposits (green). B: Cross-section of the following idealized preserved sedimentary architecture of a meander belt of the type represented in part A. C: The compartmentalization of upper point bar areas by abandonment deposits (green); development of attic reservoir compartments might lead to poor sweep efficiency if oil production occurs by waterflooding. Figure and condensed caption from Colombera et al. (2017).

Clearly channel stacking patterns, permeability differences, mud drapes, and cutoffs are important to characterizing submarine reservoirs; however, the way in which geoscientists model the order and placement of these channel stacking patterns, channel elements, and drapes is equally important to submarine reservoir characterization.

In an effort to expand the range of possibilities presented by reservoir models while minimizing computational effort, many modelers randomize channel stacking patterns and shale drupe coverage. Randomization of channel elements may prove powerful in avoiding bias towards imperfect organizational patterns and providing base case estimates for the effects of reservoir parameters on recovery. Larue and Hovadik (2006) randomize channel stacking in their simple 3D geostatistical models and shale deposition within the channel fill. Describing reservoir

connectivity as a function of NTG, they assert that poor connectivity generally occurs where NTG values are below 30% and where parallel channel stacking occurs. This kind of generalization may provide a powerful baseline for simplified analyses of channel systems in which channel movements are poorly understood. In a paper discussing the importance of reservoir architecture relative to other parameters, Larue and Hovadik (2008) state that reservoir architecture does not introduce significant uncertainties into reservoir models unless it impacts more significant factors such as reservoir connectivity, volume, or permeability. However, in this analysis of parameter significance their models of channel stacking (an architectural factor) in lowstand or in highstand scenarios, channel elements still remain largely scattered apart compared to what one may produce with a meandering channel model. Additionally, while Larue and Hovadik believe that reservoir architecture in itself does not significantly control productivity, NTG is not a perfect control either. As Jackson et al. (2019) demonstrate, connectivity is not directly correlated with NTG--thin channel element base drapes may decrease connectivity in ways not captured by NTG.

In contrast to the views of Larue and Hovadik (2008), Alpak et al. (2013) find that reservoir architecture significantly controls the recovery factor of submarine channel reservoirs. After conducting more than 1700 flow simulations in a geologically realistic three dimensional model at outcrop-scale resolution, Alpak et al. (2013) discover several factors governing oil recovery which include NTG and architectural aspects such as meander bar width, meander-belt amalgamation, and shale drape coverage emerge as consistently as significant factors affecting recovery. Covault et al. (2016) propose that randomization of channel and shale elements underestimates the connectivity of reservoirs, because autogenic movements of submarine channels preferentially connect channel elements laterally and vertically. Within a large timeframe, the composite submarine channel systems created by submarine-channel fills tend to begin with channel incision and end with aggradation. This trajectory likely adjusts its associated slope and sediment-gravity flows towards an equilibrium gradient (Covault et al., 2016). This process exerts a control on channel aggradation, which increases in the late stages of channel evolution. Within a small timeframe, the channels migrate laterally in trajectories that may be described by an implementation of the Howard and Knutson (1984) meandering channel model (Covault et al., 2016). While modelers implementing random channel placement may view associated sediment gravity flows as sporadic and unpredictable, Covault et al. (2017)

demonstrate that autogenic controls commonly organize the trajectories of channelized turbidites in sinuous systems. When reservoir architecture follows a meandering channel model and differs as a function of the incising-to-aggrading trajectory, multiple remnant channel bodies may establish connectivity between injector and producer wells and promote efficient sweep (Fig. 32). This organized stacking increases sand-on-sand contact laterally and vertically compared to random stacking--it is also potentially more realistic. In order to better condition stochastic reservoir models, modelers may borrow the approach from Colombera et al. (2017): employing descriptive statistics from large data sets as direct inputs or empirical constraints to algorithms.

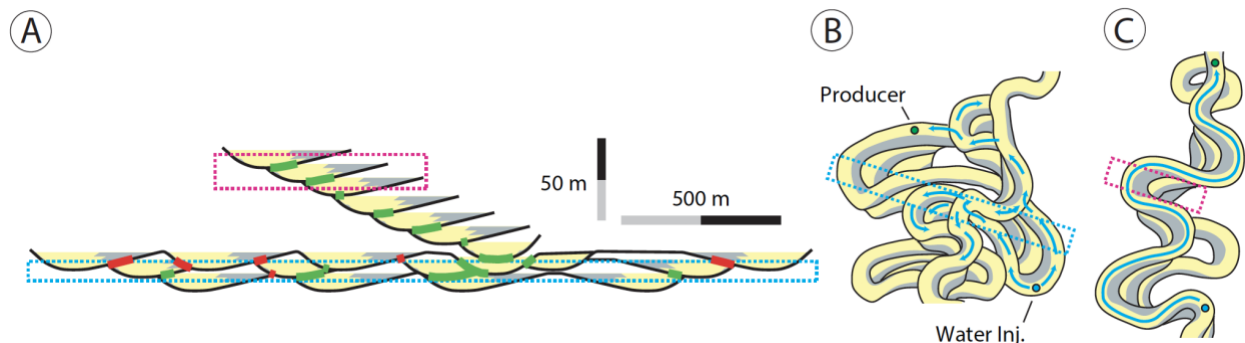


Figure 32. Hypothetical submarine-channel-system facies architecture (i.e., facies heterogeneity and stacking patterns) inspired by an outcrop, stratigraphic forward model, and potential fluid flow behavior during hydrocarbon production (Covault et al., 2016). (A) Cross section of incising-to-aggrading trajectory of a submarine-channel system with yellow representing sand-rich lithology; gray, mud-rich lithology; green lines, sand body connectivity; red lines, baffles or barriers between sand bodies in cross section. The approximate locations of B and C are blue and pink dashed boxes, respectively. (B) Lower zone of cutoff and eroded channel deposits. The water injector well is a blue dot and the producer well is a green dot. (C) The upper zone of more continuous and vertically connected sandstone-rich facies.

Key Architectural Elements of Joshua Channel

A moderately to highly sinuous channel-levee system unaffected by structural deformation or mass wasting, Joshua Channel provides an ideal case study for meandering submarine channel architecture. The main architectural elements of Joshua channel include channel fills, levees, and likely mud drapes. Channel fills are visible in seismic data and are 600 to 700 meters wide, with an aspect ratio of 36 (Posamentier 2003; Schumaker et al., 2018). Inner portions (about 200 m wide) of the channel fills feature high amplitudes, suggesting that the centers of the channel fills are sand prone. Levees rise roughly 20 m above the channel belt on the bathymetric map (Kramer and Shedd, 2017). Mud-rich deposits bury upstream sediments.

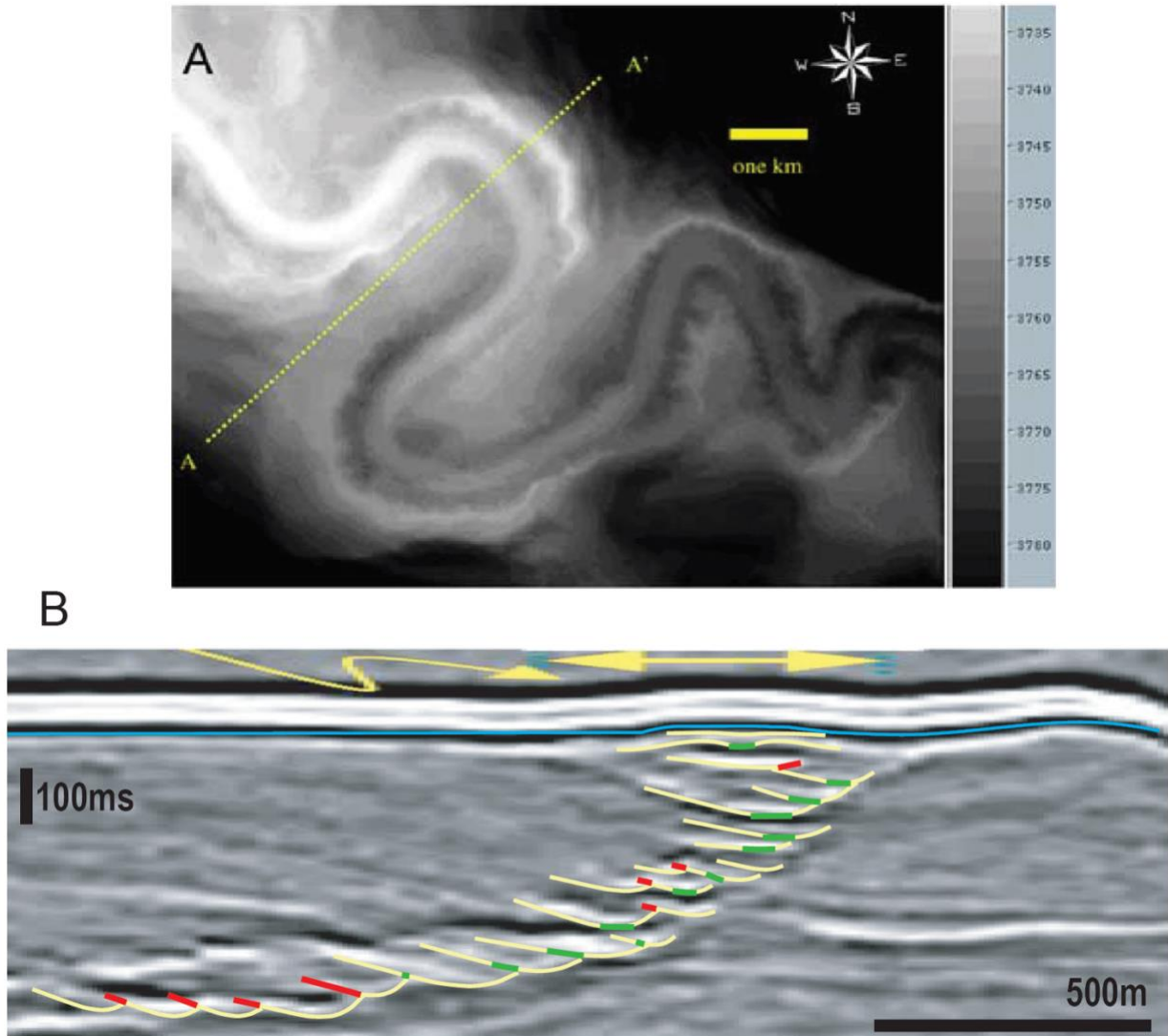


Figure 33. A: Black and white time structure map of the upper bounding surface of the Joshua channel-levee system (Posamentier, 2003). B: Transverse seismic reflection profile across the Joshua channel-levee (Posamentier, 2003), annotated with interpreted channel bases (yellow), draping facies (blue), and areas of low (red) and high (green) connectivity in a similar manner as in Covault et al. (2016). Yellow arrows are annotations by Posamentier (2003) pointing to channel width and relief. Original graphic has been vertically squeezed to reduce vertical exaggeration and more appropriately show relevant geometries.

The channel stacking patterns in Joshua channel resemble the trend described by Covault et al. (2016), with early stage poorly preserved channel elements followed by laterally migrating and then vertical aggrading channel elements (Fig. 32, Fig. 33b). The likely sandy channel elements are laterally offset at the beginning of the studied sequence and progressively become more vertically aligned. The stacking pattern appears to be well organized in a “J” shape that reflects this rapid transition from lateral to vertical stacking as well as down-system migration

(Fig. 9; Fig. 33, Fig. 34). In plan view, meander loop expansion (swing) and down-system migration (sweep) are observed. Connectivity would likely be poor in the lower intervals of the channel stack, where the channel elements are laterally offset (Fig. 34b). Connectivity would likely be stronger towards the top of the channel stack, where channels are more vertically aligned, with the exception of a few smaller fills that appear slightly offset, including one channel base towards the very top of the channel that appears to exhibit a more symmetrical profile (in a straighter portion of the channel) than preceding deposits (Fig. 34b).

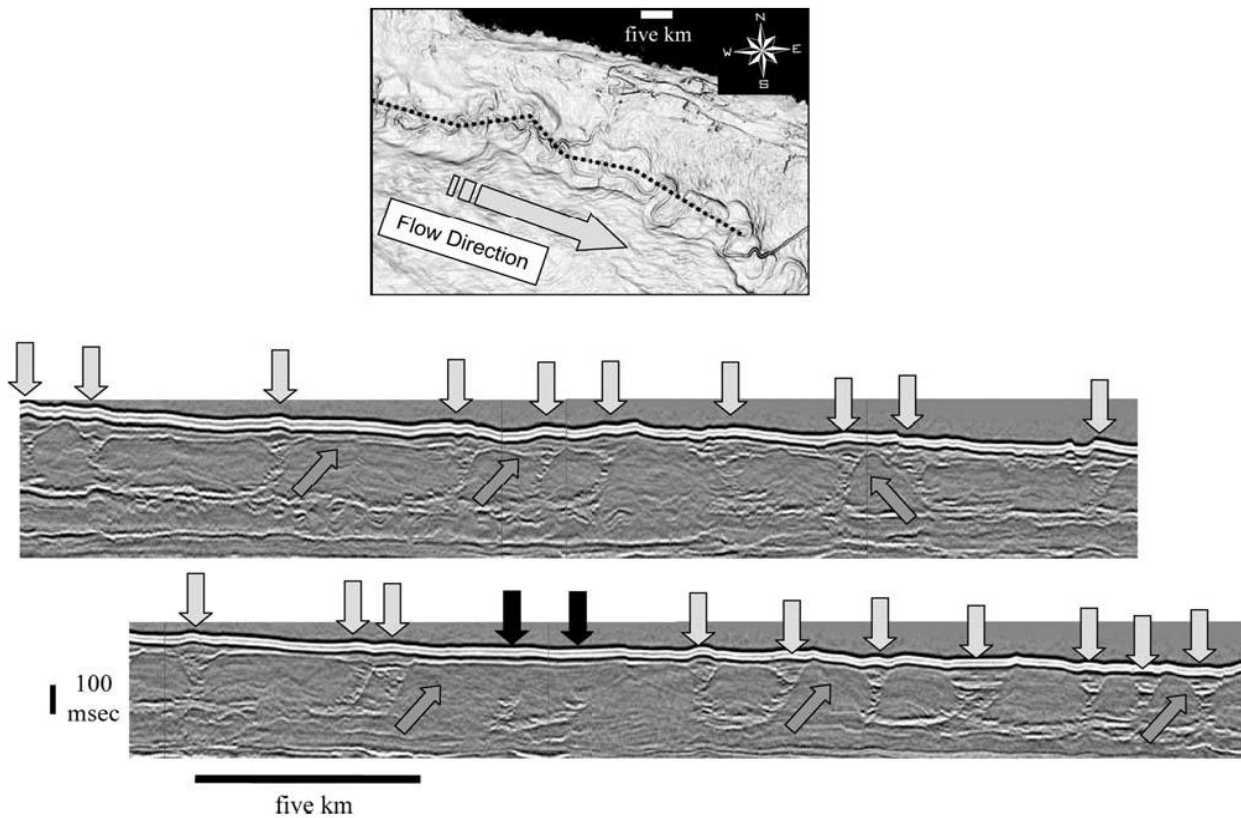


Figure 34. Axial seismic reflection profile through the channel belt with white and grey arrows indicating channel crossings; black arrows, an abandoned meander loop. Down-system migration of meander bends apparent on sixteen of the channel crossings. Figure and annotations by Posamentier (2003).

Shale drapes are not visible in the data. However, Posamentier (2003) observes bank slumps likely introduce heterogeneity or compromise connectivity in several levees and bend axes; bank slumps and potential crevasse splays are visible in the bathymetric and seismic time slice data employed for this paper. A homogenous approximately 30 m thick layer of sediments, likely mudstone, bury upstream channel deposits (Posamentier 2003).

In terms of cutoffs, none occur within the studied time interval. However, an older cutoff is visible on a seismic time slice (Fig. 35) near bends 2 and 3 and likely influenced meander bend evolution of the interpreted channel trajectories above it. Bar width in bend 2 expands by approximately 100 m between horizons 2 and 1 close to the master bounding levees, while bend 3 migrates roughly approximately 200 m down-system and expands by approximately 140 m over the abandoned channel fill in the same period. The greater movement of bend 2 relative to that of bend 3 may be attributed to many factors, but it is possible that the steeper gradient of the master bounding levees constrained the movements of bend 2 and that the potential mud-rich abandoned channel fill and gentler gradient underneath a segment of bend 3 promoted channel migration. Posamentier (2003) observes five or fewer cutoffs and oxbows in Joshua channel (Fig. 36). Cutoffs probably also played a factor in early stage evolution -- in horizon 4, the thalweg trajectory is difficult to trace, this may be the result of more erosive flows and fewer preserved deposits.

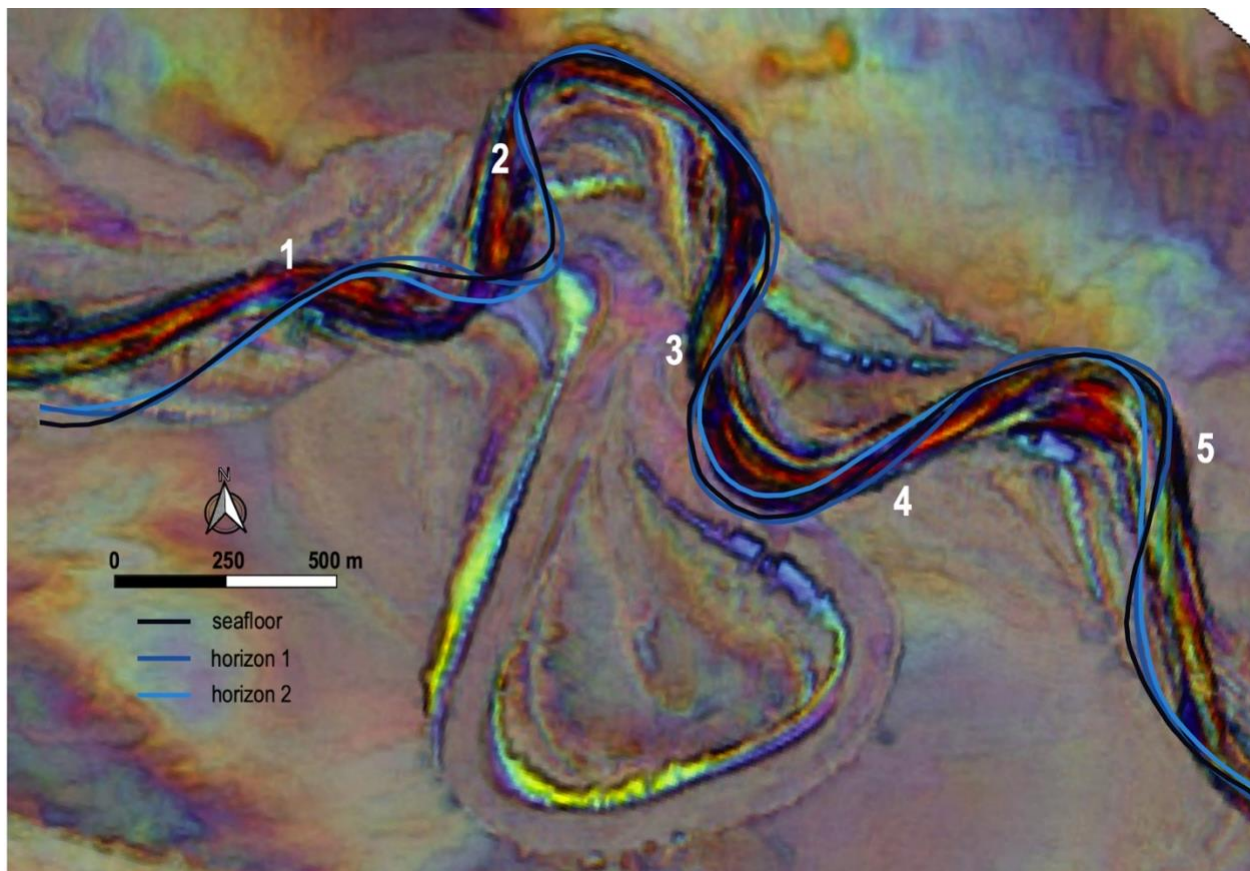


Figure 35. Cutoff observed in a 3D seismic map of Joshua Channel (Kramer et al., 2016), near the interpreted channel centerlines of bends 2 and 3, annotated in yellow in accordance with the approximate positions of their upstream curvature inflection points on the seafloor centerline.

Bar width in bend 2 expands by approximately 100 m between horizons 2 and 1 close to the master bounding levees, while bend 3 migrates roughly approximately 200 m down-system and expands by approximately 140 m over the abandoned channel fill in the same period.

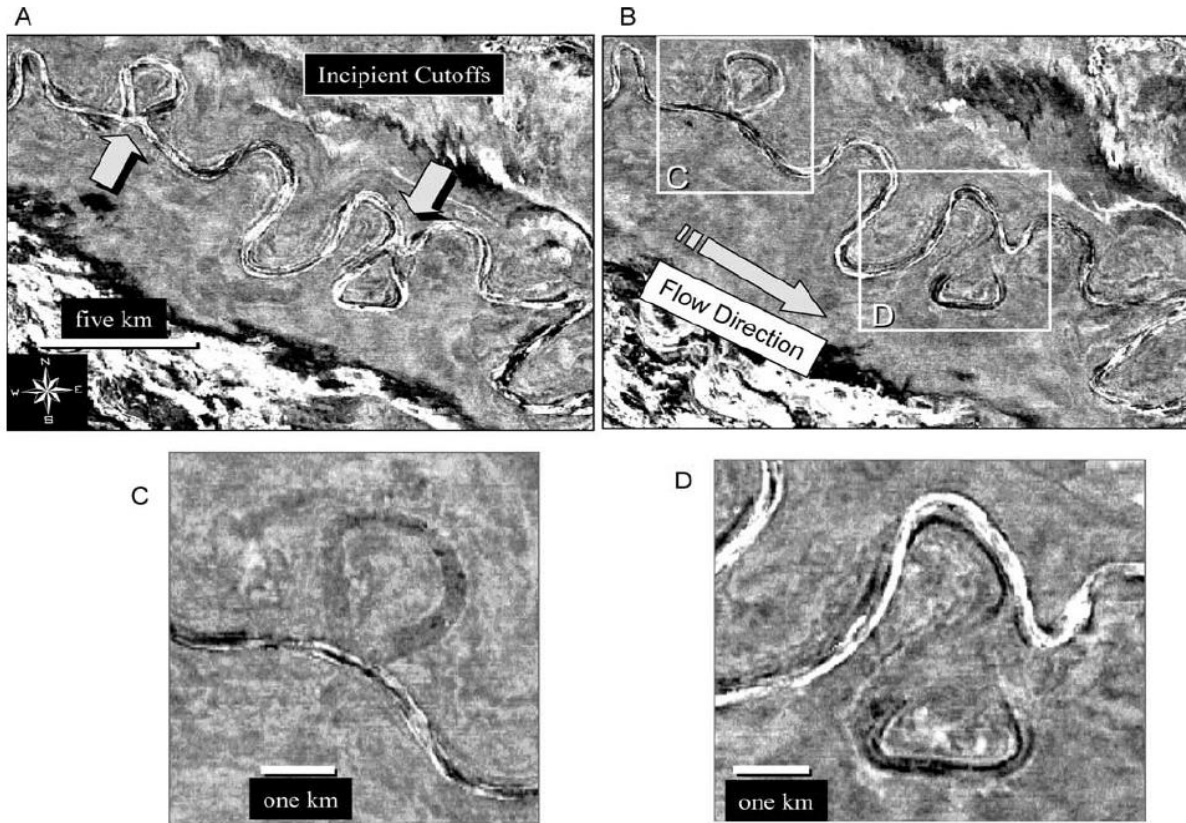


Figure 36. Meander loop cutoffs and oxbows resembling those in fluvial systems. Figure and annotations from Posamentier 2003.

Joshua Channel as an Analog for Deepwater Reservoirs

Joshua Channel shares several characteristics with producing deepwater reservoirs. Mayall et al. (2006) describe these characteristics in seismic data from a variety of turbidite channel reservoirs in deepwater Angola. While Mayall et al. (2006) do not specify which specific regions the seismic images are from, they are mostly from large, erosionally confined 3rd-order channels, typically 1 to 3km wide and 50 to 200 m thick. In the four areas describing deepwater systems that Mayall et al. (2006) describe that affect interpretations, many features of Joshua Channel are consistent with producing reservoirs. These areas are: 1) the nature of sinuosity, 2) the facies, 3) cutting and filling episodes, and 4) variable stacking patterns (Mayall et al., 2006). Mayall et al. (2006) note the spectacular sinuosity observed in not only modern submarine

channels, but also older turbidite channel sequences as well (e.g. Babonneau et al., 2002; Cronin et al., 2002; Damuth et al., 1983; Kenyon et al., 1995; Beydoun et al., 2002; Deptuck et al., 2003; Fonnesu et al., 2003; Kolla et al., 2001; Mayall and O'Byrne, 2002; Mayall and Stewart, 2000; Navarre et al., 2002; Posamentier et al., 2000; Sikkema and Wojcik, 2000; Wonham et al., 2000). This sinuosity tends to come as a result of erosional effects early in channel evolution, and then as a result of lateral migration (Mayall et al., 2006). Joshua Channel reveals sinuosity at depth in older centerlines (e.g., horizon 4), beneath which dynamic sinuous elements are imaged along with a cutoff (perhaps a remnant of some of these more erosional processes). The final element of many large erosional channels is also a highly sinuous leveed channel, many with channel-levee systems up to 500 m wide and with channel depths of a few tens of meters (Mayall et al., 2006). Here, the scale of Joshua Channel also compares: its channel-levee system is approximately 300-600 m wide and its channel axis is approximately 30 m deep. Hemipelagic drapes also commonly cover the channels, which occurs in Joshua Channel as well (Fig. 34). Mayall et al. (2006) describe repeated cutting and filling events (Fig. 37), with erosion surfaces offset laterally toward the channel bottom and vertically. Figure 34 depicts evidence of cutting and filling in Joshua channel in the yellow surfaces, particularly in the top third of the stack. Stacking styles also change frequently in producing reservoirs (Mayall et al., 2016). Channel stacks in Joshua Channel evolve from laterally offset, to vertically aligned, to discontinuous in the case of abandoned meanders (Fig. 34, Fig. 35).

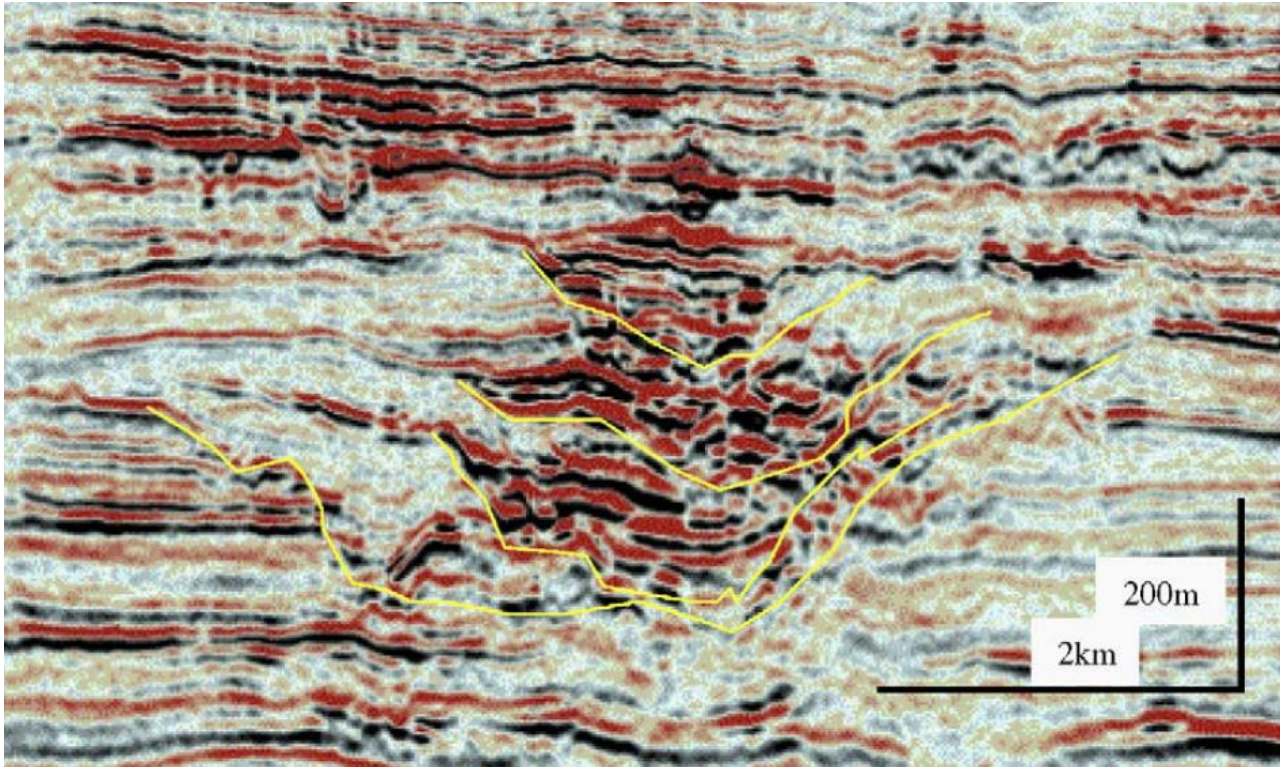


Figure 37. Cut-and-fill episode with erosional bases annotated in yellow by Mayall et al. (2006).

Joshua Channel resembles several channels of producing regions in plan view, particularly those in West Africa. The high-sinuosity and variation in channel meander width and sinuosity along Joshua channel are similar to the highly productive Green Channel Complex in the Dalia M9 Upper field in offshore Angola (Fig. 38). While the size of meander wavelengths are different (the meanders of Joshua channel appear 3 to 4 times larger than those of the Green Channel Complex), the types of bend behaviors observed (cutoffs, and single and compound bends rotating, swinging, and sweeping to varying degrees) are qualitatively similar (Fig. 38). The numerous crescent shaped single loops and compound loops in Joshua Channel are also similar to the those described by Kolla et al. (2001) in the subsurface Tertiary of offshore Angola. Similar to the channels described by Kolla et al. (2001), migration occurs in each bend of Joshua Channel to varying degrees. One particular loop in Joshua Channel bears a remarkably similar geometry, in terms of asymmetry, curvature, migration, and rotation, to a sinuous channel example in offshore Angola (Fig. 39).

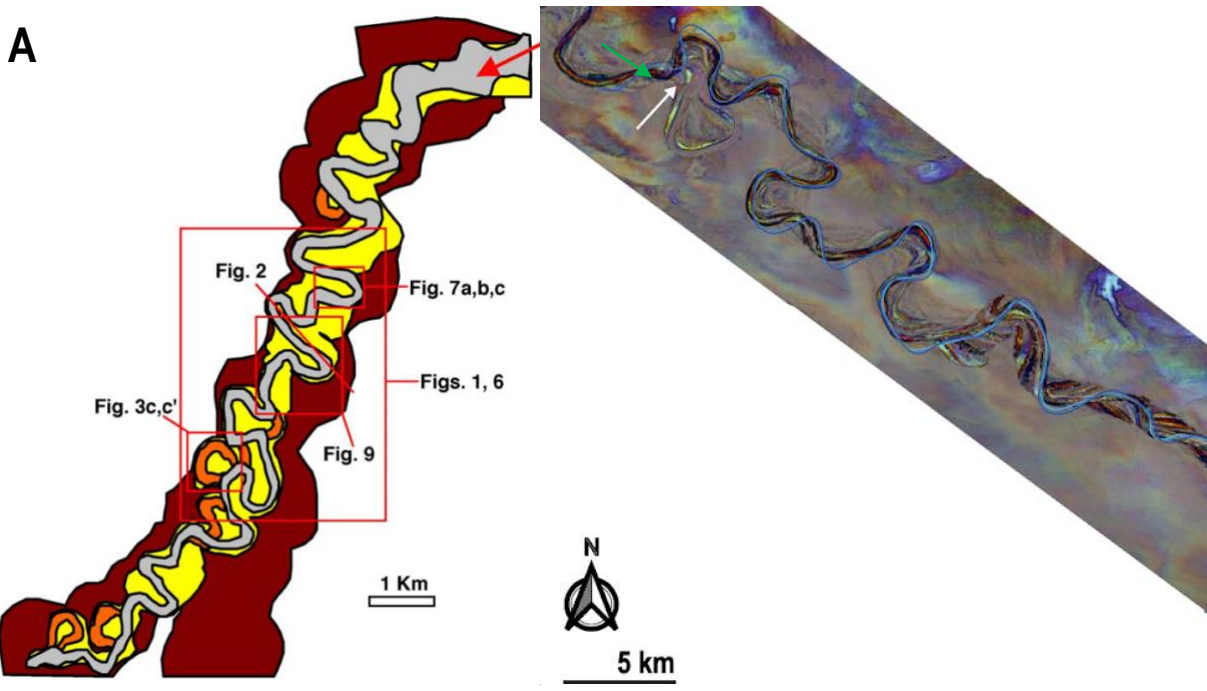


Figure 38. A: Map view of the Dalia M9 Upper field (in brown), with the Green Channel Complex (in yellow), flow direction (in red), the last position of a single, sinuous channel (in gray) and cutoff meanders (in orange) (Abreu et al., 2003). B: The upstream segment of the Joshua Channel study area with interpreted centerlines (in shades of blue) and flow direction (green arrow) on a 3D seismic map (Kramer et al., 2016).

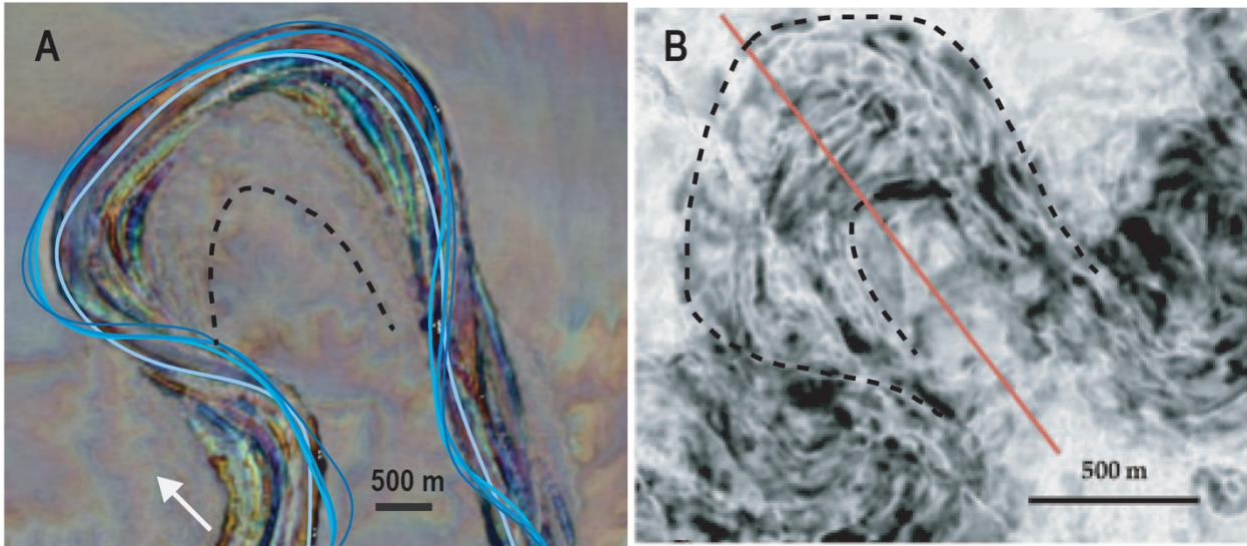


Figure 39. A: A bend in Joshua Channel seen in a 3D seismic map (Kramer et al., 2016) overlaid with interpreted centerlines (youngest in light blue and oldest in dark blue) and an interpreted rough shape of an earlier bend curvature in a dashed black line. Flow is from left to right, marked by a black arrow. B: A smaller yet strikingly similar bend in a deepwater Tertiary channel in offshore Angola (paleoflow is unknown) (Kolla et al., 2001). Annotations (dashed lines) added to interpret potential initial (inner curve) and late stage (outer curve) bend curvatures.

The stacking patterns of Joshua channel serve as analogs for many deepwater reservoirs. Joshua channel is fairly sinuous, and therefore offers many examples of meander bends. These sinuous meander bends have a point-bar-like architecture and may have generated lateral accretion packages (LAPs) as described by Abreu et al. (2003) in offshore Angola. The terrain covered by Joshua channel is not affected by obvious salt or fault structures that may impede channel development. This is very different from Angola where salt deformation plays an important role.

Joshua channel differs from deepwater reservoirs in that it is a modern submarine channel system (the morphology reflects original depositional conditions) and lacks features of confinement present in study areas such as West Africa. It also experiences an avulsion event at some point in its history which although common to submarine channel systems, may affect the expression of autogenic processes.

The main points of comparison between Joshua Channel and deepwater reservoirs of sinuous channels is that Joshua Channel follows a classic stacking pattern (reminiscent of the evolution described above by Covault et al. in 2016) and displays various examples of swing and sweep common to submarine meander bends.

Potential Reservoir Rock Properties of Joshua Channel

While there are neither core nor well data with which to analyze rock properties, one may suppose that the channel fills of the Joshua channel system are sand-rich and reservoir-prone and may resemble lithofacies of channels offshore of West Africa. The sandy fill is suggested by their high amplitude reflections (Fig. 39) and by the channel's roughly 100 m high relief above the surrounding seafloor that likely resulted from differential compaction over a relatively short timeframe (Posamentier 2003). Joshua channel may share lithological characteristics with other sinuous channels in the Gulf of Mexico, one of which is discussed by Kendrick (2000) and compared to other reservoirs. McGee et al. (1994) discuss rock properties of the Auger field, which hosts multiple reservoir styles. Of the amalgamated channel sands with overlying levee and overbank deposits (which they name the "N1" and "O" reservoirs), both of these reservoirs had porosities 29%, and boasted permeabilities of 900 md and 800 md respectively. Similar to what likely occurs in Joshua Channel, these deposits also feature fining and thinning upward trends. In the O reservoir, partial Bouma sequences of Ta (massive) through Tc (rippled,

convoluted) are common. The fact that neither Td (laminated silt and mud) nor Te (pelitic shales) were recovered in whole core suggests that depositional flows were constant and likely eroded preceding flow deposits (McGee et al., 1994). Geography may not always provide a reliable basis for comparison, so it may also be helpful to discuss the rock properties of the sinuous channels in West Africa that bear a striking resemblance to Joshua channel. Zhang et al. (2015) study the submarine fan channel reservoirs of the X oilfield in the Niger Delta Basin; they find that these reservoirs have fairly high average porosities of 24.1% (ranging from 12.1% to 37.1% and normally distributed) and very high average permeabilities of 914.6 md.

Given the information discussed and absence of well or core data, it is reasonable to assume that the coarse-grained sediment of Joshua Channel has similar characteristics as the channel systems described above. For the following discussion, this paper will assume the reservoir rock of Joshua channel has high average porosity (greater than 25%) and permeability (greater than 800 md).

Summary of parameters affecting connectivity in submarine channel reservoirs

Given the discussion above, one may conclude that several processes increase permeability in deepwater submarine channels (Table 5). Vertical permeability is enhanced by confinement, vertical stacking and aggradation. This is because confinement encourages vertical stacking, and with vertical stacking and aggradation fluid may more easily flow where coarse grains (concentrated at the center and thalweg of the channel axes) align. Horizontal permeability is enhanced by laterally offset stacking, which may erode away some of the left and righthand portions of the channel bases likely composed in finer grained material, and by lateral migration, which may produce LAPs with sand-on-sand contacts. Erosional contacts increase both horizontal and vertical permeability because of their potential to erode low-permeability, fine-grained material, such as mud drape (Fig. 30b) and cutoff (Colombera et al., 2017) features that decrease both horizontal and vertical permeability.

<i>Relative Impact</i>	<i>Vertical Permeability</i>	<i>Horizontal Permeability</i>
Vertical stacking		
Laterally offset stacking		
Erosional contacts		
Mud drapes		
Cut offs		
Aggradation		
Confinement		
Lateral migration		
Downstream migration	?	?

Table 5. Summary of factors affecting vertical and horizontal permeability noted with increasing (green) or decreasing (red) impacts. The last factor (“downstream migration”), is annotated with “?” because while this study reveals that downstream migration is probably an important aspect of deepwater channels, its specific effects on connectivity need to be studied.

The lag between curvature and migration inflection points in this study establishes downstream migration as an important factor in the evolution of Joshua Channel, and likely in many submarine channels systems. However, research on the impact of downstream migration on the connectivity of deepwater channelized reservoirs seems lacking. An important question to ask is whether this kinematic influence makes highly downstream-migrating submarine channels less or more prospective than submarine channels where downstream migration is less substantial. Downstream translation may decrease connectivity in some portions of submarine channels, yet increase them in others. For example, connectivity may increase where translating channels intersect in plan view and channels are vertically stacked (Fig. 40b, Fig. 40d). However, connectivity may decrease near counter point bars and where channels are too laterally offset to connect their coarse axes deposits (Fig. 40b, Fig. 40f). These examples only consider two theoretical scenarios in 2D. Even more differences, including relationships between cross-sectional areas, would be found in 3D. Comparisons to fluvial systems may also be helpful. In meandering rivers, downstream translation results in counter point bars that tend to be finer grained, and therefore have lower overall permeability than point bars. A similar difference might exist in submarine channels. Further study is needed to estimate the impact of downstream translation on reservoir connectivity and recovery. The results of this study point to the importance of downstream migration in the kinematics of deepwater channels and provide a solid starting point for this research.

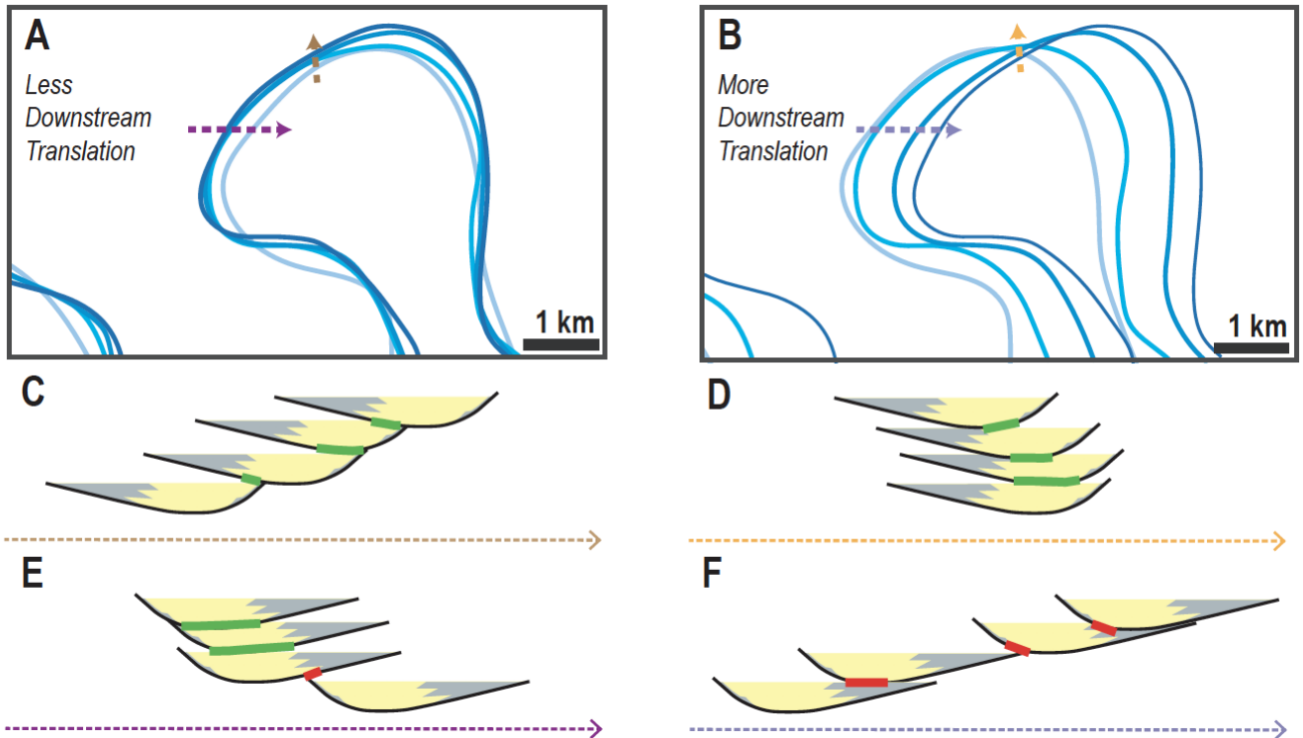


Figure 40. Theoretical cross sections of a bend in Joshua Channel and the same bend if downstream translation were heavily exaggerated, accompanied by the two bends in plan view. A: Plan view of a bend in Joshua Channel. B: Plan view of a bend in Joshua Channel distorted to exaggerate downstream translation. C: Theoretical cross section of a segment of Joshua Channel, the orange arrow in Fig. 11a. D: Theoretical cross section of a segment of Joshua Channel where downstream translation is exaggerated (orange arrow in Fig. 11b). E: Theoretical cross section of a segment of Joshua Channel, the purple arrow in Fig. 11a. F: Theoretical cross section of a segment of Joshua Channel where downstream translation is exaggerated, the purple arrow in Fig. 11b. Figures 11c-f are not to scale. Channel element illustrations are adapted from Covault et al. (2016).

Chapter Seven: Conclusions

Variation in curvature explains roughly 52% of variance in migration distance in Joshua Channel seismic data. The lag in the relationship followed bend curvature by a distance that was 3.6 to 4.2 times larger than the median thalweg width. Two widths have been identified in submarine channels, with thalweg width appearing most useful for comparisons with fluvial channels and levee crest width most useful when converted to half-width. If Joshua Channel provides an appropriate case study, which it seems to, then the relationship between curvature and migration in submarine channels appears to be similar to that in fluvial channels, with variation in migration lagging behind variation in curvature by a distance that is 2.1 to 4.7 times larger than bankfull width and 3.6 to 4.2 times larger than thalweg width. High curvatures not only drive river meandering, but also submarine channel meandering.

As with variation in migration distance, variation in half width follows curvature, however, it does so with a significantly smaller lag. These results may reflect the fact that the centerline used for the curvature was younger than the older centerline associated with the migration distance itself. They may also relate to the channel abandonment processes that generated an anomalous weak negative correlation and similarly sized small lag in the final timestep of the channel. Future studies of active channels may shed light on whether the half-width and curvature relationship echoes the curvature-migration relationship in fluvial channels, and whether half-width may be used as a proxy for migration in active channels when older centerlines are used, or other adjustments are made.

Qualitative financial analysis suggests that channel architecture may enable or disable investment in a project through its influence on hydrocarbon recovery. Curvature and migration are fundamental parameters influencing channel stacking patterns. For this reason curvature and migration impact both lateral and vertical reservoir connectivity, which influences hydrocarbon recovery through its control on flow rates. Now that a strong element of downstream migration throughout the evolution of Joshua Channel is established, the impact of downstream migration in submarine channels is critical to assess. Examples of how downstream migration may either increase or decrease reservoir connectivity in different positions within bends have been illustrated. That high curvatures tend to increase downstream migration in Joshua Channel has too been shown. Future research should establish the effects of downstream migration on reservoir connectivity in the context of the curvature and migration model. With reservoir

connectivity already difficult to estimate due to the presence of imperceptible mud drapes, models should reduce uncertainty using the relationships of readily available parameters such as curvature. These findings are not only important for the geology community, but also for oil and gas investors evaluating how prospective and productive their sinuous submarine channel plays may be.

Appendix

Example of Code for Analysis of time step 1 (Python).

Set Things Up

In [513]:

```
# Import packages  
import numpy as np  
import matplotlib.pyplot as plt  
from scipy.signal import savgol_filter  
import pandas as pd  
from scipy.signal import medfilt  
import functools  
from scipy.optimize import minimize, bisect  
import seaborn as sns
```

In [514]:

```
pwd
```

In [515]:

```
cd '/Users/indre/Python/dp_python-master'
```

In [516]:

```
from dpcore import dp
```

In [517]:

```
%matplotlib qt
```

In [518]:

```
## Define curvature functions
```

```
def compute_derivatives(x,y):
```

```
    """function for computing first derivatives of a curve (centerline)
```

```
    x,y are cartesian coordinates of the curve
```

```
    outputs:
```

```
    dx - first derivative of x coordinate
```

```
    dy - first derivative of y coordinate
```

```
    ds - distances between consecutive points along the curve
```

```
    s - cumulative distance along the curve"""
```

```
    dx = np.gradient(x) # first derivatives
```

```
    dy = np.gradient(y)
```

```

ds = np.sqrt(dx**2+dy**2)
s = np.cumsum(ds)
s = np.hstack((0,np.cumsum(ds[1:])))
return dx, dy, ds, s

```

```

def compute_curvature(x,y):
    dx = np.gradient(x); dy = np.gradient(y) # first derivatives
    ds = np.sqrt(dx**2+dy**2)
    ddx = np.gradient(dx); ddy = np.gradient(dy) # second derivatives
    curvature = (dx*ddy - dy*ddx) / ((dx**2 + dy**2)**1.5)
    s = np.cumsum(ds)
    return curvature, s

```

```

def compute_curvature(x,y):
    """function for computing first derivatives and curvature of a curve (centerline)
    x,y are cartesian coordinates of the curve
    outputs:
    dx - first derivative of x coordinate
    dy - first derivative of y coordinate
    ds - distances between consecutive points along the curve
    s - cumulative distance along the curve
    curvature - curvature of the curve (in 1/units of x and y)"""
    dx = np.gradient(x) # first derivatives
    dy = np.gradient(y)
    ds = np.sqrt(dx**2+dy**2)
    ddx = np.gradient(dx) # second derivatives
    ddy = np.gradient(dy)
    curvature = (dx*ddy - dy*ddx) / ((dx**2 + dy**2)**1.5)
    s = np.cumsum(ds)
    s = np.hstack((0,np.cumsum(ds[1:])))
    return curvature, s

```

```

def resample_curve(x,y,deltas,sf):
    dx,dy,ds,s = compute_derivatives(x,y)
    tck, u = scipy.interpolate.splprep([x,y],s=sf)

```

```

unew = np.linspace(0,1,1+s[-1]/deltas) # vector for resampling
out = scipy.interpolate.splev(unew,tck) # resampling
return out[0], out[1]

```

```

def correlate_clines(x1,x2,y1,y2):

```

```

    # use dynamic time warping to correlate centerlines
    c = len(x1)
    r = len(x2)
    sm = np.zeros((r,c))
    for i in range(0,r):
        sm[i,:] = ((x1-x2[i])**2 + (y1-y2[i])**2)**0.5
    p,q,C,phi = dp(sm,penalty=0.0,gutter=0.0)
    return p,q,sm

```

In [519]:

```

# Define migration functions

```

```

def get_migr_dist(x1,y1,x2,y2,years):

```

```

    """use dynamic time warping to correlate centerlines
    inputs:
    x1, y1 - coordinates of first centerline
    x2, y2 - coordinates of second centerline
    years - time between the two centerlines, in years
    penalty - parameter that forces more parallel correlation (or not)
    outputs:
    migr_dist - migration rate (in m/years)
    migr_sign - migration sign
    p - indices of correlation in second centerline
    q - indices of correlation in first centerline"""
    p,q,sm = correlate_clines(x1,x2,y1,y2)
    qn = np.delete(np.array(q),np.where(np.diff(q)==0)[0]+1)
    pn = np.delete(np.array(p),np.where(np.diff(q)==0)[0]+1)
    xa = x1[:-1]
    xb = x1[1:]
    ya = y1[:-1]
    yb = y1[1:]

```

```

x = x2[pn][1:]
y = y2[pn][1:]
migr_sign = np.sign((x-xa)*(yb-ya) - (y-ya)*(xb-xa))
migr_dist = migr_sign*sm[pn,qn][1:]/years
migr_dist = np.hstack((migr_dist[0],migr_dist))
return migr_dist, migr_sign, p, q

```

```

def get_predicted_migr_dist(curvature,W,k,Cf,D,kl,s):

```

```

    """function for calculating predicted migration rate
    using the simplified Howard-Knutson model

```

```

    inputs:

```

```

    W - channel width (m)

```

```

    k - constant (=1)

```

```

    Cf - friction factor

```

```

    D - channel depth (m)

```

```

    kl - migration constant (m/year)

```

```

    s - along-channel distance (m)

```

```

    output:

```

```

    R1 - predicted migration rate"""

```

```

    ds = np.diff(s)

```

```

    alpha = k*2*Cf/D

```

```

    ns = len(s)

```

```

    R0 = kl*W*curvature # preallocate vector for nominal channel migration rate

```

```

    R1 = np.zeros(ns) # preallocate adjusted channel migration rate

```

```

    for i in range(0,len(R1)):

```

```

        si2 = np.hstack((0,np.cumsum(ds[i-1::-1]))) # distance along centerline, backwards from current

```

```

point

```

```

        G = np.exp(-alpha*si2) # weighting function

```

```

        R1[i] = -1*R0[i] + 2.5*np.sum(R0[i::-1]*G)/np.sum(G) # actual migration rate (m/year)

```

```

    return R1

```

```

# function for optimizing for Cf:

```

```

def get_friction_factor(Cf,curvature,migr_dist,kl,W,k,D,s):

```

```

    R1 = get_predicted_migr_dist(curvature,W,k,Cf,D,kl,s)

```

```

    corr = correlate(R1, migr_dist)

```

```

# delta time array to match xcorr:
delta_t = np.arange(1-len(R1), len(R1))
time_shift = delta_t[corr.argmax()]
return time_shift # goal is to minimize the time shift

```

```

from __future__ import division
import numpy as np

```

Code below taken from Stack Exchange.

```

def zerocross1d(x, y, getIndices=False):

```

"""

Find the zero crossing points in 1d data.

Find the zero crossing events in a discrete data set.

Linear interpolation is used to determine the actual locations of the zero crossing between two data points showing a change in sign. Data point which are zero are counted in as zero crossings if a sign change occurs across them. Note that the first and last data point will not be considered whether or not they are zero.

Parameters

x, y : arrays

Ordinate and abscissa data values.

getIndices : boolean, optional

If True, also the indices of the points preceding the zero crossing event will be returned. Default is False.

Returns

xvals : array

The locations of the zero crossing events determined by linear interpolation on the data.

indices : array, optional

The indices of the points preceding the zero crossing events. Only returned if `getIndices` is set True.

"""

*# Indices of points *before* zero-crossing*

```
indi = np.where(y[1:]*y[0:-1] < 0.0)[0]
```

Find the zero crossing by linear interpolation

```
dx = x[indi+1] - x[indi]
```

```
dy = y[indi+1] - y[indi]
```

```
zc = -y[indi] * (dx/dy) + x[indi]
```

What about the points, which are actually zero

```
zi = np.where(y == 0.0)[0]
```

Do nothing about the first and last point should they be zero

```
zi = zi[np.where((zi > 0) & (zi < x.size-1))]
```

Select those point, where zero is crossed (sign change across the point)

```
zi = zi[np.where(y[zi-1]*y[zi+1] < 0.0)]
```

Concatenate indices

```
zzindi = np.concatenate((indi, zi))
```

Concatenate zc and locations corresponding to zi

```
zz = np.concatenate((zc, x[zi]))
```

Sort by x-value

```
sind = np.argsort(zz)
```

```
zz, zzindi = zz[sind], zzindi[sind]
```

if not getIndices:

```
return zz
```

```
else:
    return zz, zzindi
```

```
# Import CVS Files for HZ 4 and HZ3
df = pd.read_csv('/Users/indre/Desktop/Thesis Data
Processing/thalweg_hz3_vertices2.csv',usecols=[0,1])
df.columns = ['x', 'y']
x3r = np.array(df['x'])
y3r = np.array(df['y'])
df = pd.read_csv('/Users/indre/Desktop/Thesis Data
Processing/thalweg_hz4_vertices.csv',header=None,usecols=[0,1])
df.columns = ['x', 'y']
x4r = np.array(df['x'])
y4r = np.array(df['y'])
```

In [522]:

```
# Smooth, resample vector data
import scipy.interpolate
deltas = 25.0 # sampling distance, previously and in half-width analysis is 50m
sf = 20000 # smoothing factor changed from 200000 and then half that and then 20000

x1, y1 = resample_curve(x1r,y1r,deltas,sf)
x2, y2 = resample_curve(x2r,y2r,deltas,sf)
x3, y3 = resample_curve(x3r,y3r,deltas,sf)
x4, y4 = resample_curve(x4r,y4r,deltas,sf)

plt.plot(x4r,y4r,'k')
plt.plot(x3r,y3r,'k')
plt.plot(x2r,y2r,'k')
plt.plot(x1r,y1r,'k')
plt.plot(x4,y4,'y')
plt.plot(x3,y3,'c')
plt.plot(x2,y2,'g')
plt.plot(x1,y1,'b')

plt.ylabel('distance from south to north (m)', fontsize =12);
```

```
plt.xlabel('distance from east to west (m)',fontsize =12)
plt.ticklabel_format(axis='x', style='sci', scilimits=(-2,2))
plt.ticklabel_format(axis='y', style='sci', scilimits=(-2,2))
```

In [524]:

```
# Display all color coded, smoothed data
plt.plot(x4,y4,'y')
plt.plot(x3[2456:4842],y3[2456:4842],'c')
plt.plot(x2,y2,'g')
plt.plot(x1,y1,'b')
plt.ylabel('distance from south to north (m)', fontsize =12);
plt.xlabel('distance from east to west (m)',fontsize =12)
plt.ticklabel_format(axis='x', style='sci', scilimits=(-2,2))
plt.ticklabel_format(axis='y', style='sci', scilimits=(-2,2))
```

In [13]:

```
# Now, run through process for each Time step
```

Analyze Timestep 1 - Horizon 4 to and Horizon 3

In [492]:

```
# 1. Compute, Smooth Curvatures
```

```
curv,s = compute_curvature(x4,y4) # Horizon 4 (older horizon curvature used for analysis)
from scipy.signal import savgol_filter # Plot Smoothed and Raw Curvature
curv = medfilt(savgol_filter(curv,41,3),kernel_size=5) # smoothing
```

In [493]:

```
# 2. Compute, Smooth Migration Distance
```

```
years = 1.0 # to get migration distance because age and rate unknown
migr_dist, migr_sign, p, q = get_migr_dist(x4,y4,x3,y3,years)
migr_dist = medfilt(savgol_filter(migr_dist,51,3),kernel_size=5) # smoothing
curv,s = compute_curvature(x4,y4)
```

```
# Get index points
```

```
loc_zero_curv_s, loc_zero_curv = zerocross1d(s, curv, getIndices=True)
loc_zero_migr_s, loc_zero_migr = zerocross1d(s, migr_dist, getIndices=True)
```

In [447]:

```
# 3. Plot Migration and Curvature
```

```
#hz 4 to hz 3 plot
```

```
fig = plt.figure(figsize=(30,5))
```

```

ax1 = fig.add_subplot(111)
ax1.plot(s/1000.0,curv)
ax1.set_xlim(0,max(s/1000.0))
ax1.set_ylabel('curvature (1/m)', fontsize=14)

#Label curv_s=0
ax1.plot([0,max(s/1000)],[0,0],'k--')
ax2 = ax1.twinx()
ax2.plot(s/1000.0,migr_dist,'r')
ax1.set_xlabel('distance along channel (km)', fontsize=14)
ax2.set_ylabel('migration rate (m/year)', fontsize=14, color='r')
ax2.set_ylim(-300,300)
ax1.set_ylim(-0.003,0.003);

plt.title('Migration from Horizon 4 to Horizon 3', fontsize =16);

```

In [448]:

In [494]:

4. Import bends from CSV, bends picked on a seperate Jupyter notebook.*

```

df = pd.read_csv('/Users/indre/Desktop/Thesis Data
Processing/Joshua_hz4_to_hz3_inflection_and_zero_migration_indices_v2.csv',
usecols=[0,1,2,3,4])
df.columns =
['bend','index_inflection_point','index_zero_migration','s_coordinate_index_ip','s_coordinate_index_z
m']

BEND = np.array(df['bend'])
LZC = np.array(df['index_inflection_point'])
LZM = np.array(df['index_zero_migration'])
LZC_s = np.array(df['s_coordinate_index_ip'])
LZM_s = np.array(df['s_coordinate_index_zm'])
BEND=BEND+25 # add [amount] to bend 0 to account for upstream curvatures, match to 2 to 1
BEND=BEND[1:] # delete bend "0" by redefining BEND=BEND[1:]
LZC=LZC.astype(int)
LZM=LZM.astype(int)

```

In [496]:

5. Find lag between curv and migr for this time step

```
lag = np.median(LZC-LZM) # make sure these were imported
```

In [358]:

```
#find lag as index points
```

```
print lag/deltas
```

In [365]:

```
#Without lag
```

```
from scipy.stats import pearsonr
```

```
# calculate Pearson's correlation
```

```
corr, _ = pearsonr(curv, migr_dist)
```

```
print('Pearsons correlation: %.3f' % corr)
```

```
#With lag!
```

```
from scipy.stats import pearsonr
```

```
# calculate Pearson's correlation (r)
```

```
corr, _ = pearsonr(curv[:-29], migr_dist[29:]) # 29 = lag in index points
```

```
print('Pearsons correlation: %.3f' % corr)
```

```
# Correlation displayed in kernel density and scatter plots, following Figure 6 in Sylvester et al.: 5% of data points are plotted as black dots; areas shaded in blue are contour maps (with equal contour spacing) of bivariate kernel # density estimate that includes all data points"
```

```
plt.figure(figsize=(8,8))
```

```
sns.kdeplot(curv[:-28], migr_dist[28:],
```

```
           n_levels=20,shade=True,cmap='Blues',shade_lowest=False)
```

```
plt.scatter(curv[:-28][::20],migr_dist[28:][::20],c='k',s=10)
```

```
plt.xlabel('curvature (1/m)', fontsize=14)
```

```
plt.ylabel('migration distance (m), with phase lag', fontsize=14)
```

In [367]:

```
## 6. Map bends, cropped
```

```
# colors: hz1 - 'b', hz 2 - 'g', hz3 - 'c', hz 4 - 'y'
```

```
plt.figure(figsize=(60,60))
```

```
plt.plot(x4[:4511],y4[:4511], 'y')
```

```
plt.plot(x3[1606:],y3[1606:], 'c')
```

```
plt.axis('equal')
```

```
plt.scatter(x4[LZC], y4[LZC], c='r')
plt.scatter(x4[LZM], y4[LZM], c='b')
```

```
for i, txt in enumerate(BEND):
```

```
    plt.annotate(txt, (x4[LZC][i], y4[LZC][i]), color='r', size='small')
```

```
for i, txt in enumerate(BEND):
```

```
    plt.annotate(txt, (x4[LZM][i], y4[LZM][i]), color='b', size='small')
```

```
LZM=LZM.astype(int)
```

```
LZC=LZC.astype(int)
```

```
plt.ylabel('distance from south to north (m)', fontsize =12);
```

```
plt.xlabel('distance from east to west (m)',fontsize =12)
```

```
plt.ticklabel_format(axis='x', style='sci', scilimits=(-2,2))
```

```
plt.ticklabel_format(axis='y', style='sci', scilimits=(-2,2))
```

In [495]:

```
# 7. Let's plot curvature and migration rate by bends
```

```
W = 2395.1385050707095 # Median width in bathymetric dataset.
```

```
fig, ax1 = plt.subplots(figsize=(16,4))
```

```
y1g = 6.0
```

```
y2g = 0.0
```

```
y3g = -8
```

```
y4g = -18.0
```

```
for i in range(0,len(LZC)-1,2):
```

```
    xcoords = [LZC_s[i],LZC_s[i+1],LZC_s[i+1],LZM_s[i+1],LZM_s[i+1],LZM_s[i],LZM_s[i],LZC_s[i]]
```

```
    ycoords = [y1g,y1g,y2g,y3g,y4g,y4g,y3g,y2g]
```

```
    ax1.fill(xcoords,ycoords,color=[0.85,0.85,0.85],zorder=0)
```

```
offset = 10
```

```
deltas = 25.0
```

```
ax1.fill_between(s, 0, curv*W)
```

```
ax2 = ax1.twinx()
```

```
ax2.fill_between(s, 0, migr_dist, facecolor='green')
```

```
ax1.plot([0,max(s)],[0,0], 'k--')
ax2.plot([0,max(s)],[0,0], 'k--')
ax1.set_ylim(y4g,y1g)
ax2.set_ylim(-400,600)
ax1.set_xlim(0,s[-1])
for i in range(0,len(LZC)-1,2):
    ax1.text(LZC_s[i],0.5,str(i),fontsize=8)
ax1.set_ylabel('W/r (m)')
ax2.set_ylabel('migration distance (m)')
ax1.set_xlabel("distance along channel axis (m)")
plt.tight_layout()
```

Bibliography

- Abreu, V., Sullivan, M., Pirmez, C., Mohrig, D., 2003, Lateral accretion packages (LAPs): an important reservoir element in deep water sinuous channels: *Marine and Petroleum Geology*, vol. 20, p. 631-648, doi:10.1016/j.marpetgeo.2003.08.003.
- Amir, A., 1992, Channel-levee System on the Indus Fan [Ph.D. Thesis]: University of Wales, Cardiff, UK, p. 241.
- Babonneau, N., Savoye, B., Cremer, M., and Klein, B., 2002, Morphology and architecture of the present canyon and channel system of the Zaire deep-sea fan: *Marine and Petroleum Geology* v. 19, p. 445–467.
- Bastia, R., 2004, Depositional model and reservoir architecture of Tertiary deep-water sedimentation, Krishna–Godavari offshore basin, India: *Journal of Geological Society of India* v.64, p. 11–20.
- Beydoun et al., 2002, Benefits of a 3DHR survey for Girassol Field appraisal and development, Angola: *The Leading Edge*, v. 21, no. 11, p. 1152, doi:10.1190/1.1523744.
- Bouma, A.H, Stone, and C.G., 2000, Fine-grained turbidite systems: AAPG Memoir Special Publication, no. 68, p. 73-88, doi:10.1017/S0016756801236231.
- Bouroullec, R., Weimer, P., and Serrano, O., 2017, Regional structural setting and evolution of the Mississippi Canyon, Atwater Valley, western Lloyd Ridge, and western DeSoto Canyon protraction areas, northern deep water Gulf of Mexico: *AAPG Bulletin*, v. 101, no. 7, p. 1035-1071.
- Clark, J.D., Kenyon, N.H., and Pickering, K.T., 1992, Quantitative analysis of the geometry of submarine channels: implications for the classification of submarine fans: *Geology*, v. 20, p. 633–636.
- Clark, J.D., Pickering, K.T., 1996, *Submarine Channels: Process and Architecture*: London, Vallis Press, p. 231.
- Covault, J.A., Sylvester, Z., Hubbard, S.M., Jobe, Z.R., and Sech, R.P., 2016, *The Stratigraphic Record of Submarine-Channel Evolution: The Sedimentary Record*.
- Curkan, J., Nejadi, S., Durkin, P., and Hubbard, S.M., 2019, Implications of Stacked Meander-belt Deposits for Steam Assisted Gravity Drainage, McMurray Formation, Alberta *in* *Proceedings, GeoConvention: Department of Geoscience, Calgary, Canada*.

- Denne, R.A., and Blanchard, R.H., 2013, Regional controls on the formation of the ancestral DeSoto canyon by the Chicxulub impact: *Gulf Coast Association of Geological Societies Journal*, v. 2, p. 25.
- Deptuck, M.E., Steffens, G.S., Barton, M., and Pirmez, C., 2003. Architecture and evolution of upper fan channel-belts on the Niger Delta slope and in the Arabian Sea: *Marine and Petroleum Geology*, v. 20, p. 649–676.
- Donselaar, M. E., and I. Overeem, 2008, Connectivity of fluvial point-bar deposits: An example from the Miocene Huesca fluvial fan, Ebro Basin, Spain: *AAPG Bulletin*, v. 92, no. 9, p. 1109–1129, doi:10.1306/04180807079.
- Flood, R.D., and Damuth, J.E., 1987, Quantitative characteristics of sinuous distributary channels on the Amazon deep-sea fan: *Geological Society of America Bulletin* v. 98, p. 728–738.
- Gallo, A., 2004, A refresher on net present value: <https://hbr.org/2014/11/a-refresher-on-net-present-value>.
- Galloway, William E., 2008, Depositional Evolution of the Gulf of Mexico Sedimentary Basin, *in* Hsu, K.J., ed., *Sedimentary Basins of the World*: Amsterdam, Elsevier, v. 5, p. 508-539, doi:10.1016/S1874-5997(08)00015-4.
- Hagstrom, C.A., Hubbard, S.M., Leckie, D.A., and Durkin, P.R., 2019, The effects of accretion-package geometry on lithofacies distribution in point-bar deposits: *Journal of Sedimentary Research*, v. 89, p. 381–398.
- Harrison, R.N., 1968, Geology of De Soto Canyon: *Journal of Geophysical Research*, v. 73, no. 16. doi: 10.1029/JB073i016p05175.
- Hodgson, D. M., C. N. Di Celma, R. L. Brunt, and S. S. Flint, 2011, Submarine slope degradation and aggradation and the stratigraphic evolution of channel–levee systems: *Journal of the Geological Society*, v. 168, no. 3, p. 625–628, doi:10.1144/0016-76492010-177.
- Howard, A.D., and Knutson, T.R., 1984, Sufficient conditions for river meandering: A simulation approach: *Water Resources Research*, v. 20, p. 1659–1667.
- Ikeda, S., Parker, G., and Sawai, K., 1981, Bend theory of river meanders. Part 1. Linear development: *Journal of Fluid Mechanics*, v. 112, p. 363-377.

- Imran, J., Parker, G., and Pirmez, C., 1999. A numerical model of flow in meandering submarine and sub-aerial channels. *Journal of Fluid Mechanics* 400, 295–331.
- Isikdogan, F., Bovik, A., and Passalacqua, P., 2017, RivaMap: An automated river analysis and mapping engine: *Remote Sensing of Environment*, v. 202, p. 88–97, doi: 10.1016/j.rse.2017.03.044.
- Jackson, A., Stright, L., and Hubbard, S.M., 2019, Static connectivity of stacked deep-water channel elements constrained by high-resolution digital outcrop models: *AAPG Bulletin*, v. 103, no. 12, p. 2943–2973.
- Jobe, Z.R., Nick, H.C., and Auchter, N.C., 2016, Comparing submarine and fluvial channel kinematics: Implications for stratigraphic architecture: *Geology*, v. 44, no. 11, p. 931–934., doi:10.1130/G38158.1.
- Kluyver, T. et al., 2016, Jupyter Notebooks-a publishing format for reproducible computational workflows., *in* Loizides, F. and Schmidt, B. eds., *Positioning and Power in Academic Publishing: Players, Agents and Agendas: Proceedings of the 20th International Conference on Electronic Publishing*, Yektaweb publishing Company, p. 87–90, doi:10.3233/978-1-61499-649-1-87.
- Kolla, V., Bandyopadhyay, A., Gupta, P., Mukherjee, B., and Ramana, D.V., 2012, Morphology and Internal Structure of a Recent Upper Bengal Fan-Valley Complex *in* Prather, B.E., Deptuck, M.E., Mohrig, D., Hoorn, B.V., and Wynn, R.B. *Application of the Principles of Seismic Geomorphology to Continental Slope and Base-of-Slope Systems: Case Studies from Sea Floor and Near-Sea Floor Analogues: SEPM Society for Sedimentary Geology*, doi:10.2110/pec.12.99.
- Kolla, V., Bourges, P., Urruty, J-M., and Safa, P., 2001, Evolution of deepwater sinuous channels offshore Angola (west Africa) and implications for reservoir architecture: *AAPG Bulletin* v. 85, p. 1373–1405.
- Kolla, V., Posamentier, H.W., and Wood, L.J., 2007, Deep-water and fluvial sinuous channels—Characteristics, similarities and dissimilarities, and modes of formation: *Marine and Petroleum Geology* v. 24, p. 388–405.

- Kramer, K. V., and Shedd, W.W., 2017, A 1.4-billion-pixel map of the Gulf of Mexico seafloor, *Eos*, v. 98, doi:10.1029/2017EO073557.
- Kramer, K. V., Bjerstedt, T.W., and Shedd, W.W. 2016, 3D Visualization and Characterization of a Mississippi River-scale Deepwater Channel-levee System on the Basin Plain, Gulf of Mexico: Bureau of Ocean Energy Management.
- Kluyver, T. et al., 2016, Jupyter Notebooks—a publishing format for reproducible computational workflows., in Loizides, F. and Schmidt, B. eds., Positioning and Power in Academic Publishing: Players, Agents and Agendas: Proceedings of the 20th International Conference on Electronic Publishing, Yektaweb Publishing Company, p. 87–90, doi:10.3233/978-1-61499-649-1-87.
- Larue, D.K., and Hovadik, J., 2008, Why is reservoir architecture an insignificant uncertainty in many appraisal and development studies of clastic channelized reservoirs?: *Journal of Petroleum Geology*, v. 31, p. 337– 366.
- Lisiecki, L.E., and Lisiecki, P.A., 2002, *Paleoceanography*, v. 17, no. 4, doi: 10.1029/2001PA000733.
- Martin, S.T., 2015. *Valuation* (third edition): US, Pearson Education.
- Martinson, D.G., Pisias, N.G., Hays, J.D., Imbrie, J., Moore, T.C., and Shackleton, N.J., 1987, Age dating and the orbital theory of the ice ages: development of a high-resolution 0 to 250,000-year chronostratigraphy: *Quaternary Research*, v. 27, no. 1, p. 1–29.
- Mayall, M., O’Byrne, C., 2002, Reservoir Prediction and Development Challenges in Turbidite Slope Channels *in Proceedings*, OTC Conference, no. 14029.
- Mayall, M., Jones, E., and Casey, M., 2006, Turbidite channel reservoirs—Key elements in facies prediction and effective development: *Marine and Petroleum Geology*, v. 23, p. 821–841.
- Peakall, J., McCaffrey, W.D, Kneller B.C., Stelling, C.E, McHargue, T.R, Schweller W.J., 2000, A process model for the evolution of submarine fan channels: Implications for sedimentary architecture, *in Bouma, A.H., Stone, C.G. eds., Fine-Grained Turbidite Systems*, AAPG Memoir 72/SEPM Special Publication, no. 68, p. 73-88.
- Pettingill, H., and Weimer, P., 2002, Worldwide deepwater exploration and production: Past, present, and future: *The Leading Edge*, v. 21, p. 371.

- Pirmez, C., Flood, R.D., 1995, Morphology and structure of Amazon Channel: Proceedings of the Ocean Drilling Program: Initial Reports: College Station, Texas, v. 155, p. 23–45.
- Pirmez, C., and Imran, J., 2003, Reconstruction of turbidity currents in Amazon Channel: *Marine and Petroleum Geology*, v. 20, p. 823-949.
- Posamentier, H.W., 2003, Depositional elements associated with a basin floor channel-levee system: case study from the Gulf of Mexico: *Marine and Petroleum Geology*, v. 20, p. 677-690.
- Samuel, A., Kneller, B., Raslan, S., Sharp, A., and Parsons, C., 2003, Prolific deep-marine slope channels of the Nile Delta, Egypt: *American Association of Petroleum Geologists Bulletin* v. 87, p. 541–560.
- Seminara, G., 2006, Meanders: *Journal of Fluid Mechanics*, v. 554, p. 271–297, doi:10.1017/S0022112006008925.
- Shanmugam, G., 2000, 50 years of the turbidite paradigm (1950s–1990s): deep-water processes and facies models—a critical perspective: *Marine and Petroleum Geology* v. 17, p. 285–342.
- Shumaker, L.E., Jobe, Z.R., Johnstone, S.A., Pettinga, L.A., Cai, D., and Moody, J.D., 2018, Controls on submarine channel-modifying processes identified through morphometric scaling relationships: *Geosphere*, v. 14, no. 5.
- Sylvester, Z., and Covault, J.A., 2016, Development of cutoff-related knickpoints during early evolution of submarine channels: *Geology*, v. 44, no. 10, p. 835-838.
- Sylvester, Z., Durkin, P., and Covault, J.A., 2019, High curvatures drive river meandering: *Geology*, v. 47, no. 3, p. 263-266, doi:10.1130/G45608.1.
- Sylvester, Z., Pirmez, C., and Cantelli, A., 2011, A model of submarine channel-levee evolution based on channel trajectories: Implications for stratigraphic architecture: *Marine and Petroleum Geology*, v. 28, no. 3, p. 716-727, doi: 10.1016/j.marpetgeo.2010.05.012
- Talling, P. et al., 2015, Key Future Directions For Research On Turbidity Currents and Their Deposits: *Journal of Sedimentary Research*, v. 85, p. 153–169, doi:10.2110/jsr.2015.03.